

Electron Antineutrinos in the Water Phase of the SNO+ Experiment

by

Pawel Mekarski

A thesis submitted in partial fulfillment of the requirements for the degree of

Doctor of Philosophy

Department of Physics  
University of Alberta

© Pawel Mekarski, 2018

# Abstract

The SNO+ experiment will soon complete its commissioning and begin searching for the neutrinoless double beta decay of tellurium, loaded within its liquid scintillator. As a large-scale (780 tonne) liquid scintillator detector, SNO+ will also be well positioned to make a precision measurement of antineutrinos, produced from nearby nuclear reactors. Measuring these antineutrinos would provide direct information about the cores of these reactors and enable a study of neutrino properties. In anticipation, a first search for antineutrinos was performed over 69.7 live days of data collected while the SNO+ detector was filled with water, an intermediate commissioning phase. A combination of Monte Carlo simulations and measurements with radioactive calibration sources were used to determine what the antineutrino signal (characterized by a coincident positron and neutron) would look like in the detector.

The neutron modeling was first validated by performing a series of measurements of an americium-beryllium (AmBe) neutron source at the University of Alberta. The neutron interactions were detected by irradiating various targets and measuring the  $\gamma$  rays of the resulting reactions using a High Purity Germanium detector. Following Monte Carlo simulations of antineutrinos in the SNO+ detector, a search algorithm was developed to distinguish this signal

from naturally occurring backgrounds. Lastly, another AmBe source was placed within the SNO+ detector to exactly characterize its neutron detection capabilities. Searching the detector-collected data yielded a total of 5 antineutrino candidate events in the region of interest. This was in agreement with expectations from another Monte Carlo simulation that was developed to model the detector backgrounds for this specific signal. From this, an upper limit at 90% confidence was determined for the flux of antineutrinos from nuclear reactors passing through the SNO+ detector of  $(1.45 \pm 0.23) \times 10^7 \bar{\nu}/(\text{cm}^2 \text{s})$ .

# Preface

Much of the work performed in this thesis was done in contribution to the multi-national SNO+ collaboration. As such, some of the work was performed using tools developed by the researchers involved.

The majority of the work in Chapter 4 has been published as Duke, M. Hallin, A. Krauss, C. Mekarski, P. and Sibley, L. (2016) “A precise method to determine the activity of a weak neutron source using a germanium detector.” *Applied Radiation and Isotopes* 116:51–56. I performed the experimental measurements using the equipment of Krauss, C. with the assistance of Sibley, L. I was solely responsible for the development of the simulation. I also performed the data analysis and created the manuscript for submission. Duke, M. Hallin, A. Krauss, C. and Sibley, L. were involved in scientific discussion and manuscript revision. This work was performed under the supervision of Hallin, A. and Krauss, C.

The simulations of the SNO+ detector, described in Chapters 5, were performed by myself using the software programs developed by the SNO+ collaboration. The background simulation, also detailed in Chapter 5 was my own work. The various data presented in Chapters 5–8, collected using the SNO+ detector, were the result of a collaborative effort in detector operation. The design of an antineutrino search algorithm (Chapter 5), its application on the data and simulations (Chapters 5–8), and its optimization (Chapter 6) were my own work.

I designed and created the analysis algorithms to determine both the antineutrino signal expectation (Chapter 7) and subsequently the limit on the antineutrino flux (Chapter 8). I executed these algorithms on data and simu-

lation using the computing resources, provided by Compute Canada, that were allocated to Krauss, C. All analyses, on the simulations and data in Chapters 4–8, are my own work that was performed under the supervision of Hallin, A. and Krauss, C.

# Acknowledgments

Over the five years during which I performed my PhD research, there were innumerable people who supported me on this journey.

I'd first like to greatly thank my supervisor Dr. Carsten Krauss, who's guidance and knowledge have immensely helped me develop as a researcher. Additionally, I'd like to thank Dr. Aksel Hallin for the direction and insight he provided as I progressed through my many projects on the way to this dissertation. This work was also made possible by many agencies who's support allowed me to dedicate a much larger amount of my efforts to research. A big thank you to the Natural Sciences and Engineering Research Council, Alberta Innovates, and the Killam Trust for this support. Moreover, I am very appreciative of the computing resources provided by Compute Canada that made my data analyses possible.

This work was only possible due to the collaborative effort of over a hundred members of the SNO+ experiment. I am profoundly grateful for everyone's contribution to make this experiment a reality and a success. I'd like to specifically thank Dr. Christine Kraus and Dr. Erica Caden for their roles in enabling me to help locally in Sudbury with multiple aspects of the detector. I'd like to thank the Department of Physics at the University of Alberta for hosting me and providing the resources with which I have performed my research, and specifically to Sarah MacKinnon who guided me through the many years of my program.

My time on the SNO+ experiment was greatly enhanced by my fellow researchers at the University of Alberta: thank you Kalpana, David, Aleksandra, Karin, and Juan Pablo. A large thanks goes to my office mates, with who I

would spend the day, sharing many discussions scientific or otherwise: Courtney, Tom, Jie, Pooja, and Joe. You made my time as a graduate student even more enjoyable. A special thanks goes to Dr. Logan Sibley, who's impact on my life I cannot begin to describe.

Lastly, I'd like to thank my dear wife Michelle, who embarked on this adventure with me, and Sarge, who is there everyday for us. I'm excited to continue and see where life takes us all next!

# Contents

<b>List of Tables</b>	<b>xiii</b>
<b>List of Figures</b>	<b>xiv</b>
<b>1 Introduction</b>	<b>1</b>
1.1 Historical Background . . . . .	2
1.1.1 First Discovery . . . . .	2
1.1.2 Other Early Experiments . . . . .	3
1.1.3 Neutrino Oscillation Discovery . . . . .	3
1.2 Current Status of the Field . . . . .	4
<b>2 Antineutrino Theory</b>	<b>6</b>
2.1 Antineutrino Sources . . . . .	6
2.1.1 Atmospheric $\bar{\nu}$ . . . . .	6
2.1.2 Supernova $\bar{\nu}$ . . . . .	7
2.1.3 Reactor $\bar{\nu}$ . . . . .	8
2.1.4 Geoneutrinos . . . . .	10
2.2 Inverse Beta Decay . . . . .	11
2.3 Neutrino Oscillation . . . . .	13
2.3.1 Matter Effects . . . . .	16
2.4 Majorana Neutrino . . . . .	17
2.4.1 Neutrinoless Double Beta Decay . . . . .	17

<b>3 The SNO+ Detector</b>	<b>20</b>
3.1 SNO+ Detector . . . . .	20
3.1.1 Detector Overview . . . . .	20
3.1.2 Phases of Operation . . . . .	21
3.1.3 Differences from SNO . . . . .	22
3.1.4 Current Status . . . . .	23
3.2 Physics Goals . . . . .	24
3.3 Particle Detection . . . . .	26
3.3.1 Interaction . . . . .	26
3.3.2 Detector Trigger Logic . . . . .	27
3.3.3 Data Collection . . . . .	28
3.3.4 Event Reconstruction . . . . .	29
3.4 Antineutrinos in SNO+ . . . . .	31
3.4.1 Local Sources . . . . .	31
3.4.2 Interaction Expectations . . . . .	33
3.4.3 Inverse Beta Decay in SNO+ . . . . .	37
3.5 Current Reactor Antineutrino Experiments . . . . .	38
3.5.1 Detection Strategies . . . . .	38
3.5.2 Current Experiments . . . . .	39
<b>4 Neutron Measurements and Modeling</b>	<b>41</b>
4.1 Neutron Measurements . . . . .	41
4.1.1 Neutron Source . . . . .	41
4.1.2 Neutron Reactions . . . . .	43
4.1.3 Experimental Setup . . . . .	44
4.1.4 Measurement Details . . . . .	46
4.1.5 Background Measurements . . . . .	48
4.1.6 Peak Activity Determination . . . . .	50
4.2 Simulation . . . . .	52

4.2.1	Geometry Definition . . . . .	52
4.2.2	Physics Processes . . . . .	53
4.2.3	Inelastic Scattering Process . . . . .	53
4.2.4	Data Collection . . . . .	54
4.3	Results . . . . .	55
4.3.1	$^{27}\text{Al}(n,n')$ and $^{27}\text{Al}(n,p)$ Reactions . . . . .	55
4.3.2	$^{27}\text{Al}(n,\gamma)$ Reaction . . . . .	57
4.3.3	$^1\text{H}(n,\gamma)$ Reaction . . . . .	58
4.4	Model Comparison . . . . .	59
4.4.1	Neutron Activity Determination . . . . .	59
4.4.2	Considerations and Corrections . . . . .	59
4.4.3	Neutron Source Activity . . . . .	63
4.5	Inelastic Scattering Evaluation . . . . .	66
4.5.1	Cross Sections . . . . .	66
4.5.2	Measurements . . . . .	68
4.5.3	Simulation . . . . .	69
4.5.4	Results and Discussion . . . . .	69
4.6	Conclusions . . . . .	72
<b>5</b>	<b>Simulations and the Antineutrino Search Algorithm</b>	<b>74</b>
5.1	SNO+ Monte Carlo Simulation . . . . .	75
5.1.1	Antineutrino Simulation . . . . .	75
5.2	Antineutrino Event Selection . . . . .	78
5.2.1	Time Coincidence . . . . .	78
5.2.2	Position Difference . . . . .	79
5.2.3	Number of PMTs . . . . .	81
5.3	Search Algorithm . . . . .	82
5.3.1	Algorithm Overview . . . . .	82
5.4	Background Monte Carlo . . . . .	84

5.4.1	Drawbacks and Alternative . . . . .	85
5.4.2	Toy Monte Carlo Approach . . . . .	85
5.4.3	Event Generation . . . . .	86
5.4.4	Comparison to Data . . . . .	92
5.4.5	Conclusions . . . . .	96
5.5	Wavelength Shifter Improvements . . . . .	96
5.5.1	Overview . . . . .	96
5.5.2	Wavelength Shifter Details . . . . .	97
5.5.3	Reactor Antineutrino Effect . . . . .	98
5.5.4	Outlook . . . . .	99
<b>6</b>	<b>Optimizing the Search for Antineutrinos</b>	<b>102</b>
6.1	AmBe Source Calibration . . . . .	102
6.1.1	AmBe Source . . . . .	103
6.1.2	Deployment . . . . .	103
6.1.3	Neutron Detection . . . . .	104
6.1.4	Results . . . . .	105
6.1.5	Position Difference . . . . .	108
6.1.6	nHit . . . . .	109
6.2	Cut Optimization . . . . .	110
6.2.1	Time Difference . . . . .	112
6.2.2	Position Difference . . . . .	115
6.2.3	Neutron nHit . . . . .	116
6.2.4	$e^+$ nHit . . . . .	118
6.2.5	Fiducial Volume . . . . .	120
6.2.6	Final Selection Criteria . . . . .	121
<b>7</b>	<b>Signal Efficiency</b>	<b>123</b>
7.1	Neutron Tagging Efficiency . . . . .	124
7.1.1	$\gamma$ ray Event Rate . . . . .	124

7.1.2	Tagging Efficiency Determination . . . . .	128
7.1.3	Systematic Uncertainty . . . . .	129
7.2	$e^+$ Detection Efficiency . . . . .	140
7.3	Fiducial Volume Efficiency . . . . .	143
7.4	Summary and Expectation . . . . .	145
<b>8</b>	<b>Searching for Antineutrinos in SNO+ Data</b>	<b>147</b>
8.1	Detector Data Overview . . . . .	147
8.1.1	Data Processing Details . . . . .	147
8.1.2	Live Time . . . . .	148
8.2	Search Results . . . . .	149
8.2.1	Background Considerations . . . . .	149
8.3	Background Expectation . . . . .	152
8.4	Confidence Interval . . . . .	154
8.4.1	Final Region of Interest . . . . .	154
8.4.2	Limit on Number of Events . . . . .	155
8.5	Antineutrino Limit . . . . .	155
8.5.1	Antineutrino Flux . . . . .	155
8.5.2	Flux Uncertainty . . . . .	158
<b>9</b>	<b>Conclusions</b>	<b>162</b>
<b>Bibliography</b>		<b>164</b>
<b>Appendix A Inelastic Scattering Model</b>		<b>179</b>
<b>Appendix B Data Cleaning Cuts</b>		<b>182</b>
<b>Appendix C SNO+ Water Data Runs</b>		<b>184</b>
<b>Appendix D Signal to Background Optimization</b>		<b>189</b>

# List of Tables

2.1	Summary of the neutrino oscillation parameters. . . . .	15
3.1	Summary of the thermal powers and distances of the closest nuclear reactors to the SNO+ detector. . . . .	32
4.1	Systematics for the neutron activity measurements. . . . .	64
6.1	Values of the selection criteria used to identify a coincident event pair as an antineutrino candidate. . . . .	122
7.1	Number of particles produced by the AmBe neutron source. . .	127
7.2	List of AmBe source positions for which calibration data were collected with the SNO+ detector. . . . .	130
7.3	Position resolutions obtained from fits to the AmBe (4.4 MeV $\gamma$ ray) and $^{16}\text{N}$ source data. . . . .	135
7.4	Mean neutron lifetimes as determined from various sources. . .	137
7.5	Summary of the efficiencies in detecting signal events. . . . .	146
8.1	Number of expected background event pairs vs. number of measured event pairs for different values of a minimum $e^+$ nHit cut. .	154
8.2	IAEA and IESO nuclear reactor electric powers. . . . .	160
8.3	Comparison of IAEA and IESO reactor power outputs for the SNO+ data-taking period. . . . .	161

# List of Figures

2.1	$\bar{\nu}_e$ energy spectra from a PWHR reactor.	9
2.2	$\bar{\nu}_e$ energy spectra from radioisotopes in the Earth.	10
2.3	Total cross section for the inverse beta decay reaction.	12
2.4	Energy spectrum of the detectable $\bar{\nu}_e$ from a nuclear reactor.	13
2.5	Survival probability of $\bar{\nu}_e$ that have traveled 240 km and 345 km.	16
3.1	The main structural components of the SNO+ detector.	22
3.2	Picture of the SNO+ detector during its water phase.	24
3.3	Expectations for the $0\nu\beta\beta$ decay signal and backgrounds.	25
3.4	Event display of the SNO+ detector during a muon event.	29
3.5	Event display of the SNO+ detector during a common event.	30
3.6	Map of the nuclear power reactors around the SNO+ detector.	32
3.7	Energy of the $\bar{\nu}_e$ that interact in the SNO+ detector.	34
3.8	Energy of the $\bar{\nu}_e$ that interact in the SNO+ detector after neutrino oscillations.	36
4.1	Energy of the neutrons produced from the $^9\text{Be}(\alpha,\text{n})$ reaction.	42
4.2	Cross sections of neutron reactions on acrylic and aluminum.	45
4.3	Cross sectional view of the HPGe detector system.	47
4.4	Photograph of the HPGe detector system.	47
4.5	Diagrams of the configurations used in the laboratory experiment.	49
4.6	Configuration diagrams of all HPGe detector measurements.	51

4.7	Energy spectra for the measurement of the aluminum disk and four acrylic disks. . . . .	56
4.8	Energy spectra for the measurements of aluminum disks. . . . .	57
4.9	Energy spectra for the measurement of six acrylic disks. . . . .	58
4.10	Measured and simulated $^{60}\text{Co}$ detection efficiencies. . . . .	62
4.11	Neutron source activities determined for different measurements.	63
4.12	Energy spectra of the 4438 keV $\gamma$ ray from the AmBe source. . .	65
4.13	Neutron scattering cross sections for the main elements of the SNO+ detector. . . . .	67
4.14	Energy spectra for a measurement of a tellurium ingot. . . . .	69
4.15	Energy spectra for neutron reactions induced on tellurium. . . . .	71
5.1	Simulated time difference between $e^+$ and 2.2 MeV $\gamma$ ray emission.	78
5.2	Distance travelled from neutron emission to capture. . . . .	80
5.3	Reconstructed distance between the $e^+$ and neutron events. . . . .	80
5.4	Difference between reconstructed positions and true positions. .	81
5.5	nHit distribution for the $e^+$ and neutron events. . . . .	82
5.6	Time, radius, and nHit distributions from 2.6 live days of data..	87
5.7	2-dimensional distributions of the SNO+ detector data. . . . .	88
5.8	Simulated and measured time difference distributions. . . . .	90
5.9	Relative probability of an event reconstructing at a given radius.	91
5.10	Simulated and measured reconstructed radii distributions. . . . .	92
5.11	nHit distribution of events within the central water volume. . . .	93
5.12	Time difference between events in data compared to simulation.	94
5.13	Position difference between events in data compared to simulation.	94
5.14	nHit distribution of events in data compared to simulation. . . .	95
5.15	Cherenkov emission spectrum and PMT quantum efficiency. . . .	97
5.16	Bis-MSB absorption coefficient and emission spectrum. . . . .	98
5.17	nHit distributions for water and water with Bis-MSB. . . . .	100
5.18	Position difference for water and water with Bis-MSB. . . . .	101

6.1	Time, radius, and nHit distributions from AmBe data. . . . .	104
6.2	Time difference between events in AmBe and background data. .	106
6.3	Time difference between subsequent events for the AmBe source.	108
6.4	Position difference in AmBe source and background data. . . . .	108
6.5	nHit distribution of coincidence event pairs for AmBe source data.	109
6.6	Simulated neutron capture time difference vs. distance traveled.	113
6.7	Time difference vs. position difference of AmBe source data. . .	114
6.8	Signal and background acceptance of the time difference cut. . .	114
6.9	Position difference for AmBe data and background simulation. .	115
6.10	Signal and background acceptance of the position difference cut.	116
6.11	Second event nHit for AmBe data and background simulation. .	117
6.12	First event nHit for AmBe source data and reactor simulation. .	118
6.13	First event nHit for reactor and background simulations. . . . .	119
6.14	Signal and background acceptance of the first event nHit cut. . .	119
6.15	Signal and background acceptance of the radius cut. . . . . .	121
6.16	$\frac{SA}{\sqrt{BA}}$ of the radius cut value applied separately to each event. .	122
7.1	nHit distribution of the 4.4 MeV $\gamma$ ray compared to background.	125
7.2	nHit distributions for data with and without the AmBe source .	126
7.3	Background subtracted nHit distribution of the AmBe source. .	127
7.4	Measured and simulated nHit distribution of the 4.4 MeV $\gamma$ ray.	128
7.5	Neutron tagging efficiency at different radii within the detector.	130
7.6	Variance of the neutron tagging efficiency for different positions.	131
7.7	Reconstructed position of $\gamma$ rays from the $^{16}\text{N}$ source. . . . .	133
7.8	Reconstructed position of 4.4 MeV $\gamma$ rays from the AmBe source.	134
7.9	Position difference for original and resampled data. . . . . .	136
7.10	Position difference for data with resampled first event positions.	136
7.11	Time difference between simulated 4.4 MeV $\gamma$ ray–neutron pairs.	138
7.12	Measured and modeled trigger efficiencies. . . . . . . . . .	139
7.13	Detection efficiency for simulated $e^+$ . . . . . . . . . . . .	141

7.14	Measured and simulated nHit distributions of the $^{16}\text{N}$ source . . .	142
7.15	Mean of the $^{16}\text{N}$ nHit distribution at different radii. . . . .	142
7.16	Difference between the fraction of events within an nHit ROI for $^{16}\text{N}$ data and simulation. . . . .	143
7.17	Reconstructed position of neutrons from the AmBe source. . . .	145
8.1	nHit distribution for 69.7 live days of data after selection cuts. .	150
8.2	Illustration of the “measured” and “mirrored” nHit regions. . .	151
8.3	Ratio of the number of events in each of the two nHit regions. .	151
8.4	Simulated nHit distribution of the 69.7 days of data. . . . .	153
8.5	Sensitivity and $e^+$ efficiency vs. the minimum nHit cut value. .	156
8.6	Electric power outputs of the three closest nuclear reactors. . . .	160

# Chapter 1

## Introduction

Antineutrinos rarely interact with matter, allowing them travel large distances (up to a galactic scale) unimpeded. Measurements of the rare few antineutrinos to do interact therefore provide direct information about the sources that emitted them. Additionally, these measurements also allow for the study of the antineutrinos themselves — where there are still several unanswered questions about these elusive particles and many current experiments exploring them.

This thesis presents the first search for antineutrinos in the data collected by the water-filled SNO+ detector between September 1, 2017 and March 31, 2018. During this period of time, a small number of antineutrinos, produced from nearby nuclear reactors, interacted within the detector. Over this same period, the detector measured many more interactions from naturally occurring backgrounds. The search for antineutrinos therefore required the development of a software algorithm to separate them from these backgrounds. This search algorithm was designed in a way to directly translate into use in future phases of the experiment.

To understand the signal from antineutrinos in the SNO+ detector, Monte Carlo simulations were used. Before using these simulations, the physical processes that they model were validated. This was done by performing a series of laboratory measurements using a radioactive source that mimics parts of the

antineutrino signal. This model validation is described fully in Chapter 4.

Similarly, an alternative data-driven Monte Carlo approach was developed to accurately simulate the background. The exact Monte Carlo methods used to simulate both the antineutrino signal and the detector background are detailed in Chapter 5. With a picture of what the antineutrino signal looks like, this chapter also describes the development of an analysis algorithm that searches for it.

The parameters that define the search algorithm were optimized to provide the best possible distinction of antineutrinos from the backgrounds, which is discussed in Chapter 6. With a well-defined search, the efficiency of detecting antineutrinos and the associated expected rate was determined in Chapter 7. These procedures included the analysis of multiple calibration sources and Monte Carlo simulations to best describe the antineutrino signal in the SNO+ detector.

Lastly, the details of the search using detector-collected data are compiled in Chapter 8. In the absence of an observed signal, a limit on the number of antineutrinos that pass through the SNO+ detector at any given moment was determined.

## 1.1 Historical Background

### 1.1.1 First Discovery

Early in the 1900s, a problem was found in the kinematics of beta decay. Namely, the energy and momentum were not conserved between the nucleus and emitted electron. The proposition from Pauli in 1930 that the reaction instead shares its energy between three outgoing particles (the nucleus, electron, and a neutrino) solved this problem and introduced the neutrino as a potential new particle [1].

The existence of the neutrino remained unproven until 1956 when Cowan

and Reines provided the first direct detection [2]. They placed their experiment near a nuclear reactor, in which a large amount of beta decay takes place and thereby provides a large electron antineutrino  $\bar{\nu}_e$  flux. Their experiment detected the neutrinos when they interacted with the protons in their water tanks.

### 1.1.2 Other Early Experiments

Neutrinos are also produced as part of nuclear reactions at the core of the Sun. A different set of experiments were undertaken to measure this neutrino flux. The first was the Homestake experiment, by Davis, which consisted of  $380\ m^3$  of dry-cleaning fluid [3]. Solar neutrinos (electron neutrinos  $\nu_e$ ) incident on chlorine in the fluid were occasionally captured, producing radioactive argon. By periodically extracting and measuring the argon, the neutrino flux was determined. This flux was only about a third [4] of the prediction by Bahcall [5], giving rise to the solar neutrino problem.

### 1.1.3 Neutrino Oscillation Discovery

#### Solar Neutrinos

Later experiments, including GALLEX [6], SAGE [7], and Super-Kamiokande [8] also observed this discrepancy, again seeing fewer neutrinos from the Sun than expected. This problem is solved with the inclusion of neutrino oscillations, wherein some of the  $\nu_e$  produced in the Sun change flavour (to  $\nu_\mu$ ,  $\nu_\tau$ ) as they travel to the Earth. The flavour of an antineutrino defines the charged lepton it would produce in a weak interaction. An experiment sensitive to all flavours of neutrinos was needed in order to verify this theory.

This experiment came in the form of the SNO (Sudbury Neutrino Observatory) detector, which consisted of 1000 tonnes of heavy water ( $D_2O$ ) [9]. The breakup of deuterium ( $D$ ) by an incident neutrino is equally sensitive to all

three flavours, which enabled SNO to observe the predicted flux of neutrinos from the Sun [10]. Similarly to the other neutrino experiments at the time, SNO also measured a deficit in the expected  $\nu_e$  flux in a different interaction channel [11]. This provided strong evidence for neutrino oscillations as the cause of the solar neutrino problem.

### Atmospheric Neutrinos

Atmospheric neutrinos (a combination of  $\nu_e$ ,  $\nu_\mu$ ,  $\bar{\nu}_e$ , and  $\bar{\nu}_\mu$  produced from interactions with cosmic rays) are all measured by the Super-Kamiokande experiment along with the direction from which they come [12]. Super-Kamiokande observed a large deficit in the number of  $\nu_\mu + \bar{\nu}_\mu$  that traveled through the Earth, as compared to those that only passed through the atmosphere. This effect is not present in the measured  $\nu_e + \bar{\nu}_e$  [13]. This deficit is also explained by neutrino oscillations ( $\nu_\mu$  to  $\nu_\tau$ ) and confirmed neutrino oscillations for atmospheric neutrinos.

### Nobel Prize

For their roles in the discovery of neutrino oscillations, in 2015, Arthur McDonald and Takaaki Kajita were jointly awarded the Nobel Prize in Physics. McDonald received it specifically for the result produced by the SNO experiment in measuring solar neutrino oscillations. Kajita was awarded for his work with the Super-Kamiokande experiment in discovering neutrino oscillations for atmospheric neutrinos.

## 1.2 Current Status of the Field

Presently, with the observation of neutrino oscillations, at least two of the neutrino mass states must have a non-zero mass [14]. Through measurements made on these oscillations the differences between neutrino mass states ( $m_1$ ,

$m_2$ , and  $m_3$ ) are known along with the mixing between these mass states and flavour states [15–19]. From further measurements of the Z boson decay width, it is also known that only 3 flavours of light non-sterile neutrinos exist [20]. This finding is supported by cosmological results based on neutrino decoupling in the early universe [21].

Presently, a few unanswered questions remain in regards to the neutrino:

- What is the charge-parity (CP) violating phase for neutrino oscillations?
- Is  $m_3 > m_2$  (normal hierarchy) or is  $m_2 > m_3$  (inverted hierarchy)?
- What is the absolute mass of the neutrino?
- Is the neutrino distinct from its antiparticle?

Current and future neutrino experiments, SNO+ included, are all looking to answer one or more of these questions.

# Chapter 2

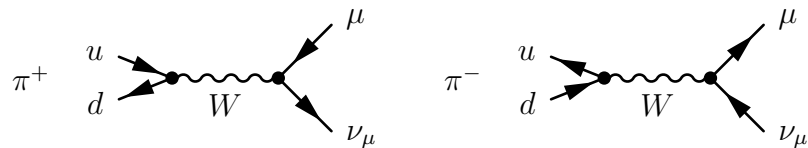
## Antineutrino Theory

### 2.1 Antineutrino Sources

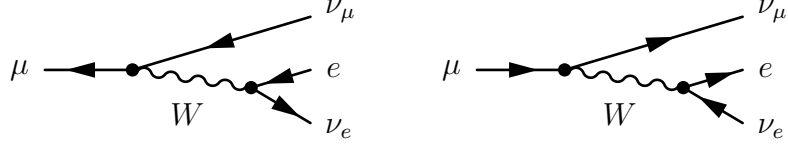
Many sources, covering a wide range of energies, produce antineutrinos. The sources that produce the vast majority of antineutrinos passing through the Earth at any given moment include cosmic rays interacting in the atmosphere, supernovae, nuclear reactors, and the Earth's crust and mantle. Each will be described, with more details provided for the reactor-produced antineutrinos that the SNO+ detector aims to measure.

#### 2.1.1 Atmospheric $\bar{\nu}$

At any given moment, cosmic rays are bombarding the Earth's atmosphere. The majority of these cosmic rays are high energy protons [22]. As these high energy particles collide with the nuclei of the atmosphere, an abundance of charged pions  $\pi^\pm$  are produced. The  $\pi^+$  and  $\pi^-$  quickly decay to  $\mu^+ + \nu_\mu$  and  $\mu^- + \bar{\nu}_\mu$ , respectively, through the exchange of a  $W^\pm$  boson:



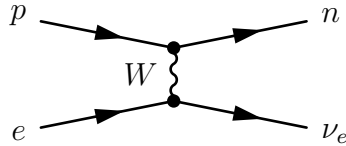
The  $\mu^+$  and  $\mu^-$  may then decay to  $e^+ + \bar{\nu}_\mu + \nu_e$  and  $e^- + \nu_\mu + \bar{\nu}_e$ , respectively:



These processes produce both  $\bar{\nu}_e$  and  $\bar{\nu}_\mu$  along with  $\nu_e$  and  $\nu_\mu$  [23]. The energies of these neutrinos range from 0.1 GeV to well past  $10^6$  GeV [24]. The majority of the antineutrinos are at the lower energies of this range, where the flux drops rapidly with energy  $E$  as  $E^{-2.7}$  [25]. Near the surface of the Earth, the flux of neutrinos going upwards is equal to those going downwards. This allows for measurements of any asymmetry caused by oscillations, which with the neutrinos traveling 10–10,000 km corresponds to measurements of specific oscillation parameters [26].

### 2.1.2 Supernova $\bar{\nu}$

During a core-collapse supernova, a large fraction (99%) of the energy is radiated away in the form of neutrinos [27]. In the initial stages of the supernova, electrons capture on protons to produce a burst of  $\nu_e$  as the core collapses:



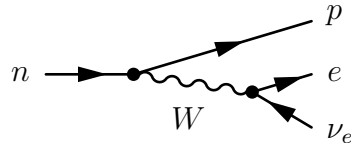
Once the density of the core reaches that of nuclear matter, the collapse is halted and a proto-neutron star forms. As the proto-neutron star cools, it emits neutrinos and antineutrinos of all flavours. A variety of processes produce these neutrinos (for example,  $e^- + e^+ \rightarrow \nu + \bar{\nu}$ ) [28]. The vast majority of neutrino emission of a core-collapse supernova occurs over a period of approximately 10 seconds and produces neutrinos with energies in the 10s of MeV [29].

Experimental evidence of these neutrinos came in 1987 when supernova SN 1987A occurred in the nearby Large Magellanic Cloud. Three neutrino detectors at the time, Kamiokande-II [30], Irvine-Michigan-Brookhaven [31], and Baksan [32], recorded a total of 24 events within a period of 13 seconds. With many more neutrino detectors operational today, another nearby supernova would provide an immense amount of neutrino detections. This would be very important in providing information from directly within the supernova and help to develop and confirm the physical models for core-collapse supernovae.

### 2.1.3 Reactor $\bar{\nu}$

Large numbers of antineutrinos are produced in the radioactive decay that occurs in the cores of nuclear reactors, resulting from the fission of the nuclear fuel. Nuclear fuel is composed of four primary isotopes:  $^{235}\text{U}$ ,  $^{238}\text{U}$ ,  $^{239}\text{Pu}$ , and  $^{241}\text{Pu}$ . Following the fission of any of these isotopes, the neutron-rich fragments undergo a series of  $\beta^-$  decays until they reach a stable isotopic state.

In each of these  $\beta^-$  decays, a neutron decays to proton, emitting an electron  $e^-$  and an electron antineutrino  $\bar{\nu}_e$ :



The energy spectrum of the emitted  $\bar{\nu}_e$  is continuous and differs for each decaying isotope as each has a different amount of energy that can be released. The  $\bar{\nu}_e$  energy spectrum for each of the four fuel isotopes is therefore a sum of the spectra from its daughter isotopes. The total  $\bar{\nu}_e$  energy spectrum for the reactor core is then the weighted sum of the contributions from the individual fuel isotopes (where the relative composition of the core varies for different reactor types).

Using the parameterized form from Huber and Schwetz [33] for the four different isotope contributions and the relative composition for a pressurized

heavy-water reactor (PHWR), the energy spectrum of the emitted antineutrinos is shown in Figure 2.1.

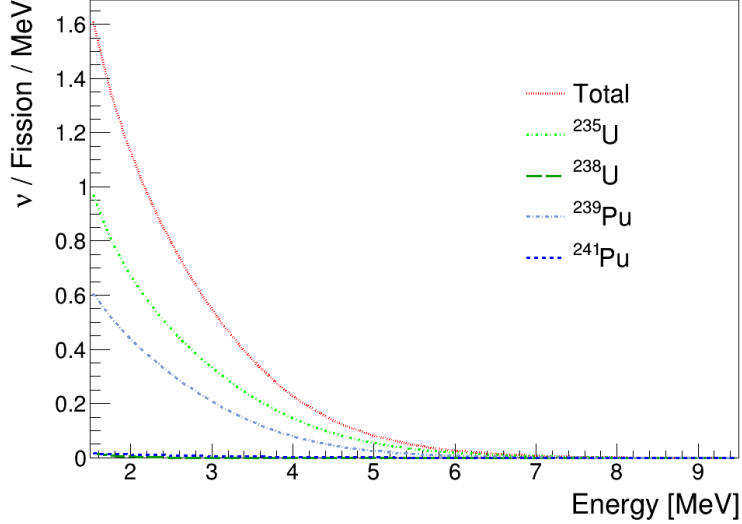


Figure 2.1: Energy spectra of the emitted  $\bar{\nu}_e$  from the different isotopes that make up the nuclear fuel in a PHWR reactor. The total energy spectrum, as the sum of the four contributions, is also shown.

The total flux  $\Phi$  of antineutrinos emitted by the reactor can be determined from the thermal power produced by each core. This requires the time averaged thermal power  $\langle P_{\text{Th}} \rangle$ , calculated by:

$$\langle P_{\text{Th}} \rangle = P_{\text{Th}} LF \quad (2.1)$$

where  $P_{\text{Th}}$  is the listed thermal power at operating capacity and  $LF$  is the load factor (the fraction of the time that the reactor was operating at capacity). To determine the total number of antineutrinos produced at a given energy  $N(E)$ , the flux also needs to be corrected by the energy released per fission  $Q_i$  [34]:

$$N(E) = \langle P_{\text{Th}} \rangle \sum_{i=1}^4 \frac{p_i}{Q_i} \Phi_i(E) \quad (2.2)$$

where the sum is over the four main isotopes of the nuclear fuel  $i$  and includes

the power fraction  $p_i$  of each fuel isotope that produces a flux of antineutrinos  $\Phi_i(E)$  per fission.

### 2.1.4 Geoneutrinos

In addition to the  $\beta^-$  decay in nuclear fuel, decay from naturally occurring radioactive isotopes in the Earth's crust and mantle can similarly produce large quantities of  $\bar{\nu}_e$ . The majority of these  $\bar{\nu}_e$  come from the decay of  $^{238}\text{U}$  and  $^{232}\text{Th}$  and their daughter isotopes, with smaller contributions from  $^{40}\text{K}$  and  $^{235}\text{U}$ . By summing the contributions from each parent isotope, the energy spectra of the emitted  $\bar{\nu}_e$  can be determined and are shown in Figure 2.2. This spectrum differs from Figure 2.1, where geoneutrinos are seen to be produced at lower energies as compared to reactor-produced antineutrinos. This results from the difference between the decay of U and Th directly (for geoneutrinos) and the decay of U and Pu fission fragments (reactor antineutrinos).

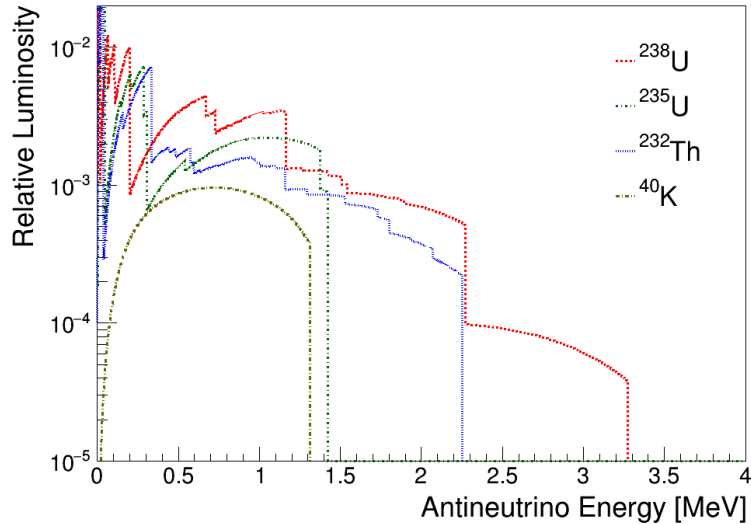


Figure 2.2: Energy spectra of the  $\bar{\nu}_e$  emitted from naturally occurring radioisotopes in the Earth. Data from [35].

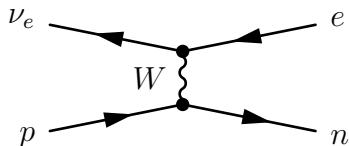
Both the KamLAND [36] and Borexino [37] large-scale liquid scintillator experiments have made measurements of geoneutrinos. As geoneutrinos overlap

the energy range of antineutrinos from reactors, they are measured together. A precise knowledge of the reactor antineutrino spectrum is needed to disentangle the geoneutrino contributions.

Additionally, U and Th isotopes are much more concentrated in Earth’s crust as compared to the mantle. However, both the crust and mantle are expected to have similar total U and Th masses [38], producing similar quantities of antineutrinos. The flux of geoneutrinos will therefore vary based on an experiment’s location, due to the variation in Earth’s crust thickness [39]. There has so far been evidence of mantle component measurements by subtracting out the crustal contribution [39, 40]. These measurements of geoneutrinos provide direct information about the radiogenic heat generation within the Earth, serving as a crucial input in the development of heat flow models.

## 2.2 Inverse Beta Decay

One of the primary mechanisms used to detect  $\bar{\nu}_e$  is the inverse beta decay (IBD) reaction. In this reaction, a  $\bar{\nu}_e$  interacts with a proton:



This results in the simultaneous emission of a  $e^+$  and a neutron. The  $e^+$  will typically travel a very short distance, in a short period of time  $O(\text{ns})$ , after which it will annihilate with an  $e^-$ , producing two 511 keV  $\gamma$  rays. The neutron is less likely to interact immediately. It will instead scatter off of nuclei and lose energy (a process called thermalization). This will occur over a longer period of time  $O(100 \mu\text{s})$  and a longer distance, ending with the neutron capturing on a proton (or other nucleus).

For the IBD reaction to occur, the  $\bar{\nu}_e$  must have sufficient energy. This energy  $E_{\text{Thr}}$  corresponds to the mass difference between the initial and final

particles:

$$E_{\text{Thr}} \approx m_n + m_e - m_p \quad (2.3)$$

Therefore the neutrino must have an energy of at least 1.8 MeV for the reaction to take place [41].

The IBD reaction is used in many antineutrino detection experiments as it has a relatively high cross section (as compared to elastic scattering [42]) and provides a coincident signal. The cross section of the IBD reaction as calculated by Vogel and Beacom [43] is shown in Figure 2.3. It depends on the energy of the  $\bar{\nu}_e$ , increasing with higher energies. The product of the cross section with the expected flux from a source (for example, a nuclear reactor) gives the energy spectrum of the IBD interactions that will occur within a detector. The shape of this energy spectrum for reactors is illustrated in Figure 2.4. The complete calculation that includes the rate of these interactions specific to the SNO+ detector is performed later in Section 3.4.2.

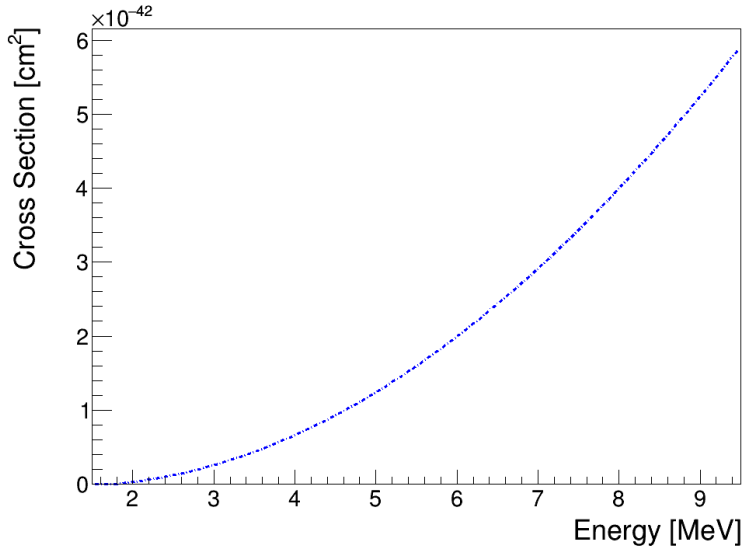


Figure 2.3: Total cross section for the inverse beta decay reaction on hydrogen as a function of the  $\bar{\nu}_e$  energy.

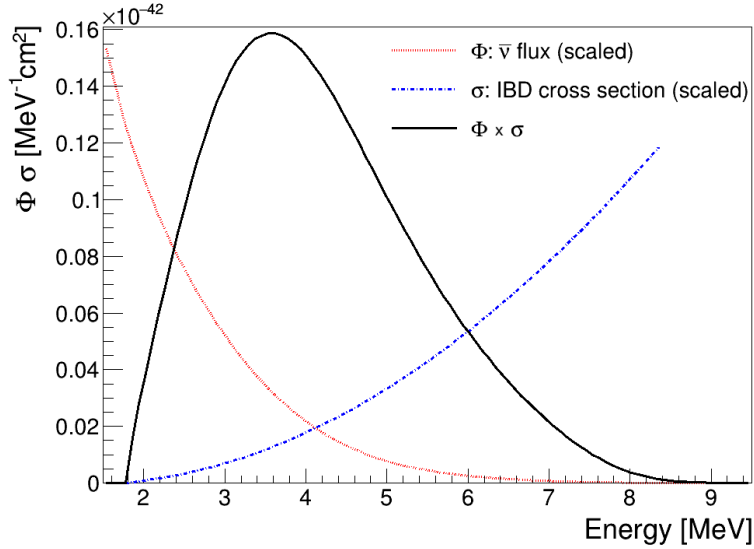


Figure 2.4: Energy spectrum of the  $\bar{\nu}_e$  (from a nuclear reactor) that will interact within a detector via IBD (the product of the flux and cross section,  $\Phi \times \sigma$ ). The scaled IBD cross section and reactor flux spectra are also shown.

## 2.3 Neutrino Oscillation

A neutrino is always created in a particular weak interaction eigenstate, called a “flavour” state (using the previous example of a  $\bar{\nu}_e$  emitted in a  $\beta^-$  decay). This means it is created as a superposition of mass states (labeled  $\nu_1$ ,  $\nu_2$ , and  $\nu_3$ ). More generally, each flavor  $l$  of neutrino  $\nu_l$  is defined as a sum over mass states  $i$ :

$$|\nu_l\rangle = \sum_{i=1}^n U_{li}^* |\nu_i\rangle \quad (2.4)$$

where the interaction between neutrino flavour and mass states is described by the matrix  $U$ . This framework is not limited to three neutrino flavours. Models exist that include  $\nu_e$ ,  $\nu_\mu$ , and  $\nu_\tau$  along with one or more flavours of “sterile” neutrinos (neutrinos that do not interact via the weak interaction) [44]. However, the existence of sterile neutrinos has yet to be experimentally verified.

As a neutrino travels, if the mass states and mixing angles are not degenerate, the phase between the states will change with distance. For a free particle,

with energy  $E$  and momentum  $\vec{p}$ , this propagation along the direction  $\vec{x}$  in time  $t$  may be described by:

$$|\nu_i(\vec{x}, t)\rangle = e^{-i(Et - \vec{p}\cdot\vec{x})} |\nu_i(0, 0)\rangle \quad (2.5)$$

When the neutrino flavour is measured, the mass states may have different relative phases and there is a chance to detect this neutrino as a different flavour state. In the three neutrino model, the relationship between the neutrino flavour and mass states may be parametrized by the Pontecorvo-Maki-Nakagawa-Sakata (PMNS) Matrix [45]:

$$U = \begin{pmatrix} c_{12}c_{13} & s_{12}c_{13} & s_{13}e^{-i\delta} \\ -s_{12}c_{23} - c_{12}s_{23}s_{13}e^{i\delta} & c_{12}c_{23} - s_{12}s_{23}s_{13}e^{i\delta} & s_{23}c_{13} \\ s_{12}s_{23} - c_{12}c_{23}s_{13}e^{i\delta} & -c_{12}s_{23} - s_{12}c_{23}s_{13}e^{i\delta} & c_{23}c_{13} \end{pmatrix} \quad (2.6)$$

where  $c_{ij}$  and  $s_{ij}$  represent  $\cos \theta_{ij}$  and  $\sin \theta_{ij}$ . This matrix is parameterized by three mixing angles ( $\theta_{12}$ ,  $\theta_{23}$ , and  $\theta_{13}$ ) and a charge-parity (CP) violating phase factor ( $\delta$ ).

The mixing angles define how different the flavour and mass states are from each other. In the case of all mixing angles being zero, this matrix becomes the identity matrix. In this case, the mass states are equal to the flavour states and no oscillation will occur. Conversely, for mixing angles of  $45^\circ$  the oscillation is maximal.

In the three neutrino model, the oscillation probability is also described by two mass squared differences ( $\Delta m_{21}^2$  and  $\Delta m_{32}^2$ ). Different neutrino experiments target the measurement of these parameters. The values of these five parameters are all known from various measurements. Table 2.1 summarizes the current values of these parameters.

Given the example of a nuclear reactor (producing  $\bar{\nu}_e$ ), using equations 2.4, 2.5, and 2.6, the probability of measuring a  $\bar{\nu}_e$  with energy  $E$  as a  $\bar{\nu}_e$  after it

Oscillation Parameters	
$\sin^2 \theta_{12}$	$0.307 \pm 0.013$
$\sin^2 \theta_{23}$	$0.417^{+0.025}_{-0.028}$
$\sin^2 \theta_{13}$	$(2.12 \pm 0.08) \times 10^{-2}$
$\Delta m_{21}^2$	$(7.53 \pm 0.18) \times 10^{-5} \text{ eV}^2$
$ \Delta m_{32}^2 $	$(2.51 \pm 0.05) \times 10^{-3} \text{ eV}^2$

Table 2.1: Summary of the neutrino oscillation parameters as reported by the Particle Data Group in 2018 (corresponding to the case of a normal hierarchy and 1<sup>st</sup> quadrant for  $\sin^2(\theta_{23})$ ) [46].

has traveled a distance  $L$ , called the survival probability, is [47]:

$$P(\bar{\nu}_e \rightarrow \bar{\nu}_{e(L,E)}) = |\langle \bar{\nu}_e | \bar{\nu}_{e(L,E)} \rangle|^2 = 1 - \cos^4 \theta_{13} \sin^2 2\theta_{12} \sin^2 \Delta_{21} - \sin^2 2\theta_{13} (\cos^2 \theta_{12} \sin^2 \Delta_{31} + \sin^2 \theta_{12} \sin^2 \Delta_{32}) \quad (2.7)$$

where each  $\Delta$  term above (expressed in more relevant units), can be written as:

$$\Delta_{ij} = 1.267 \Delta m_{ij}^2 [\text{eV}^2] \frac{L[\text{km}]}{E[\text{GeV}]} \quad (2.8)$$

This expression is referred to as the survival probability of the  $\bar{\nu}_e$ . It also neglects the modification in the case of a non-zero CP violating phase (not yet measured by any experiment). The effect of the CP phase is negligible for reactor antineutrino experiments [48].

Continuing with the example of the  $\bar{\nu}_e$  produced from nuclear reactors, if the  $\bar{\nu}_e$  oscillate to  $\bar{\nu}_\mu$  or  $\bar{\nu}_\tau$  they can no longer interact via the IBD reaction. At the detector, this would appear as a deficit in the number of detections as compared to the null oscillation prediction. From the expression in Equation 2.7, using the oscillation parameters from the Particle Data Group [41], the survival probability is shown in Figure 2.5 for  $\bar{\nu}_e$  after they have traveled 240 km and 345 km (distances relevant to the SNO+ detector).

For this specific case of  $\bar{\nu}_e$  from reactors traveling hundreds of kilometres, the large-scale features in the survival probability are the result of the  $\sin^2 \Delta_{21}$  term in Equation 2.7. The small scale features are the result of the  $\sin^2 \Delta_{31}$  terms

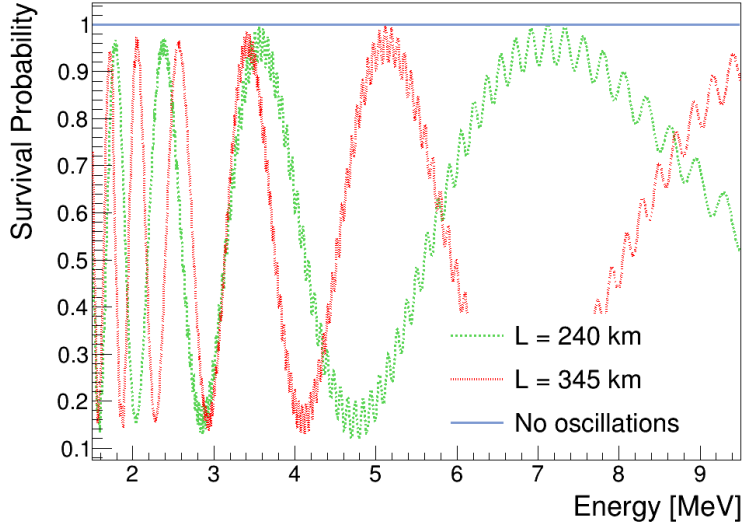


Figure 2.5: Survival probability of  $\bar{\nu}_e$  that have traveled a distance of 240 km and 345 km as a function of energy. The case of no neutrino oscillations is also shown.

(where  $\sin^2 \Delta_{31} \approx \sin^2 \Delta_{32}$  here as  $\Delta m_{31}^2 \approx \Delta m_{32}^2$ ) and are not resolvable in any current experiment because of the energy resolution that would be required [49].

### 2.3.1 Matter Effects

The presence of electrons in matter causes neutrinos to propagate differently than in vacuum. The neutrinos may interact with these electrons as they travel. Within matter, the possible interactions are different for  $\nu_e$  (which have charged-current and neutral-current interactions) and  $\nu_\mu, \nu_\tau$  (which have neutral-current interactions only). This subsequently affects the oscillation probabilities as compared to propagation in vacuum. This is referred to as the Mikheyev-Smirnov-Wolfenstein (MSW) effect [50].

In the two neutrino oscillation case, this effect is observed through an effective mixing angle  $\theta_{\text{eff}}$  and mass squared difference  $\Delta m_{\text{eff}}^2$ :

$$\sin 2\theta_{\text{eff}} = \frac{\sin 2\theta}{\sqrt{(\cos 2\theta - A)^2 + \sin^2 2\theta}} \quad (2.9)$$

$$\Delta m_{\text{eff}}^2 = \Delta m^2 \sqrt{(\cos 2\theta - A)^2 + \sin^2 2\theta} \quad (2.10)$$

where the constant  $A$  is given by:

$$A = \pm \frac{2\sqrt{2}G_F N_e E}{\Delta m^2} \quad (2.11)$$

This is positive for neutrinos and negative for antineutrinos.  $G_F$  is the Fermi constant,  $N_e$  is the electron density of the matter, and  $E$  is the neutrino's energy.

Unlike vacuum oscillations, this effect differs for  $\nu_e$  and  $\bar{\nu}_e$  and also depends of the sign of  $\Delta m^2$ . For certain neutrino energies and electron densities, this effect has resonances where it can be significant (even if the mixing angle itself is small). From Equation 2.9, this resonance occurs when  $A \approx \cos 2\theta$ . However, for the energies of  $\bar{\nu}_e$  produced from reactors, the effect on oscillations is very small [51].

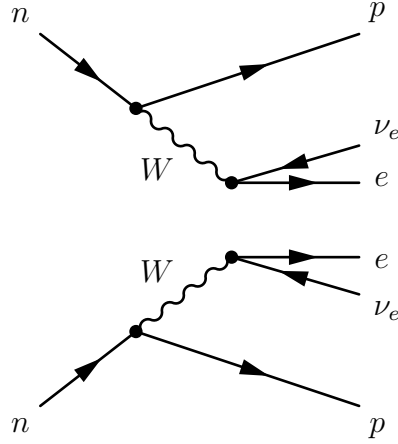
## 2.4 Majorana Neutrino

It is postulated, first by Majorana in 1937, that the neutrino may be its own antiparticle. Specifically, for “Majorana neutrinos”, there is no distinction between a neutrino and an antineutrino [52]. These neutrinos still have their respective left and right-handed helicities, which determine the charge of the lepton that is produced in weak interactions.

### 2.4.1 Neutrinoless Double Beta Decay

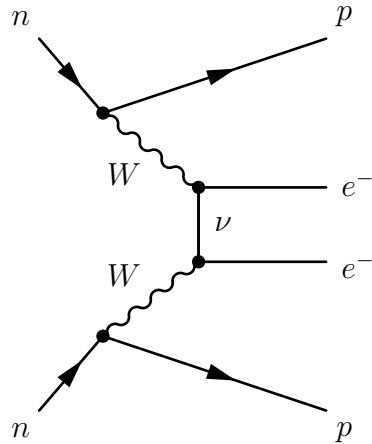
There exists a small subset of radioactive isotopes in which the decay through the emission of a single  $e^-$  is energetically forbidden, but the simultaneous emission of two  $e^-$  is not. These isotopes can undergo double beta ( $\beta\beta$ ) decay. This higher order decay process is greatly suppressed in comparison to  $\beta$  decay.

There are only 11 isotopes which have been observed to undergo  $\beta\beta$  decay. The lifetimes are on the order of  $10^{18}$ – $10^{21}$  years [46]. Through this process, two neutrons  $n$  in the nucleus become protons  $p$  resulting in the emission of two  $e^-$  and two  $\bar{\nu}_e$ :



$$(A, Z) \rightarrow (A, Z + 2) + 2e^- + 2\bar{\nu}_e \quad (2.12)$$

The possibility exists, in the case of Majorana neutrinos, that rather than two  $\bar{\nu}_e$  being emitted in the final state, a  $\nu_e$  is exchanged between the two decaying neutrons. This requires that there is no distinction between a  $\bar{\nu}_e$  and  $\nu_e$ . In this decay, no neutrinos are emitted from the nucleus (only the two  $e^-$ ). This process is called neutrinoless double beta ( $0\nu\beta\beta$ ) decay and is shown below:



$$(A, Z) \rightarrow (A, Z + 2) + 2e^- \quad (2.13)$$

The half-life of the  $0\nu\beta\beta$  decay  $T$  is given by the following expression [53]:

$$\frac{1}{T} = G|M|^2 m_{\beta\beta}^2 \quad (2.14)$$

with  $G$  being the phase factor (which depends on the kinematics of the decay),  $|M|^2$  the nuclear matrix element (which depends on the nuclear structure of the isotopes involved), and  $m_{\beta\beta}$  the effective neutrino mass.

The kinematics of  $\beta\beta$  and  $0\nu\beta\beta$  decay differ and can be used to differentiate the decay of the two processes. In the case of the  $\beta\beta$  decay, the total energy is shared between the two  $e^-$  and two  $\bar{\nu}_e$  (with a very small amount transferred to the recoiling nucleus). This results in a broad continuous  $e^-$  energy spectrum. However, in the case of  $0\nu\beta\beta$  decay, the total energy is shared only between the two  $e^-$  (and nucleus) in the final state, resulting in a very narrow energy spectrum. Therefore, by measuring an excess of final states with this energy (the sum of the two  $e^-$  energies), one can search for the occurrence of  $0\nu\beta\beta$  decay. The observation of  $0\nu\beta\beta$  would provide evidence for the Majorana nature of the neutrino and also give a handle on the absolute neutrino mass scale.

An observation (i.e. measurement of  $T$ ) would quantify the effective neutrino mass as  $G$  and  $|M|^2$  can be calculated theoretically [51, 54]. The uncertainty on a such mass measurement would additionally depend on the uncertainties on  $G$  and  $|M|^2$ .  $G$  is determined from the kinematics of this decay process and has a relatively small uncertainty. However, recent analyses of the calculations of  $|M|^2$  and its systematics indicate that these values are likely known to only a factor of 2–3 [55]. To accurately determine the neutrino mass from a future  $0\nu\beta\beta$  decay measurement, more work is first required to decrease these uncertainties.

# Chapter 3

## Inverse Beta Decay in the SNO+ Detector

### 3.1 SNO+ Detector

#### 3.1.1 Detector Overview

The SNO+ detector is geographically situated near Sudbury, Ontario, at coordinates of  $46^{\circ}28'30''$  N and  $81^{\circ}12'4''$  W. It is located deep underground within an excavated rock cavity measuring 22 m in diameter and 34 m in height. The rock above the detector is primarily norite with a total overburden of  $2092 \pm 6$  m. This reduces the muon flux passing through the detector to roughly 1 every 20 min [56]. Overburden is crucial in reducing the amount of cosmogenic backgrounds as the muons may otherwise produce neutrons or unstable isotopes [57].

The detector itself consists of the same 12 m diameter and 5.5 cm thick acrylic sphere (referred to as the “acrylic vessel”) used for the SNO experiment. It is concentric within a 17.8 m diameter geodesic photomultiplier tube (PMT) support structure. This stainless steel structure holds 9438 8-inch Hamamatsu R1408 PMTs that face inwards. Each PMT is mounted within a 27 cm diameter

light concentrator. The PMTs and concentrators give a total effective coverage of 54%. Additionally, 91 more PMTs are mounted on the structure facing outwards. These PMTs are designed to detect light originating from outside the structure to act as a veto [58].

The space between the rock cavity walls and acrylic vessel is filled with 7000 tonnes of ultra-pure water, acting to shield the detector from radioactivity originating from the rock. The acrylic vessel is supported by two series of ropes. One set of ropes are anchored above the detector, supporting any downward forces (hold-up ropes). The other set are anchored to the rock cavity floor and will support any upward buoyant forces (hold-down ropes). Both sets are required as the detector will experience both upward and downward forces during its commissioning process and operation [59]. The main structural components of the SNO+ detector are illustrated in Figure 3.1.

### 3.1.2 Phases of Operation

Through its commissioning process, the SNO+ detector will go through three distinct phases of operation:

- **Water Phase** — The acrylic vessel was filled with 900 tonnes of ultra-pure water.
- **Scintillator Phase** — The acrylic vessel will be filled with 780 tonnes of linear alkylbenzene (LAB) mixed with 2 g/L of 2,5-diphenyloxazole (PPO), a liquid scintillator [61].
- **Tellurium Phase** — The existing liquid scintillator will be loaded with natural tellurium to a concentration of 0.5%, giving a  $^{130}\text{Te}$  mass of 1600 kg [62].

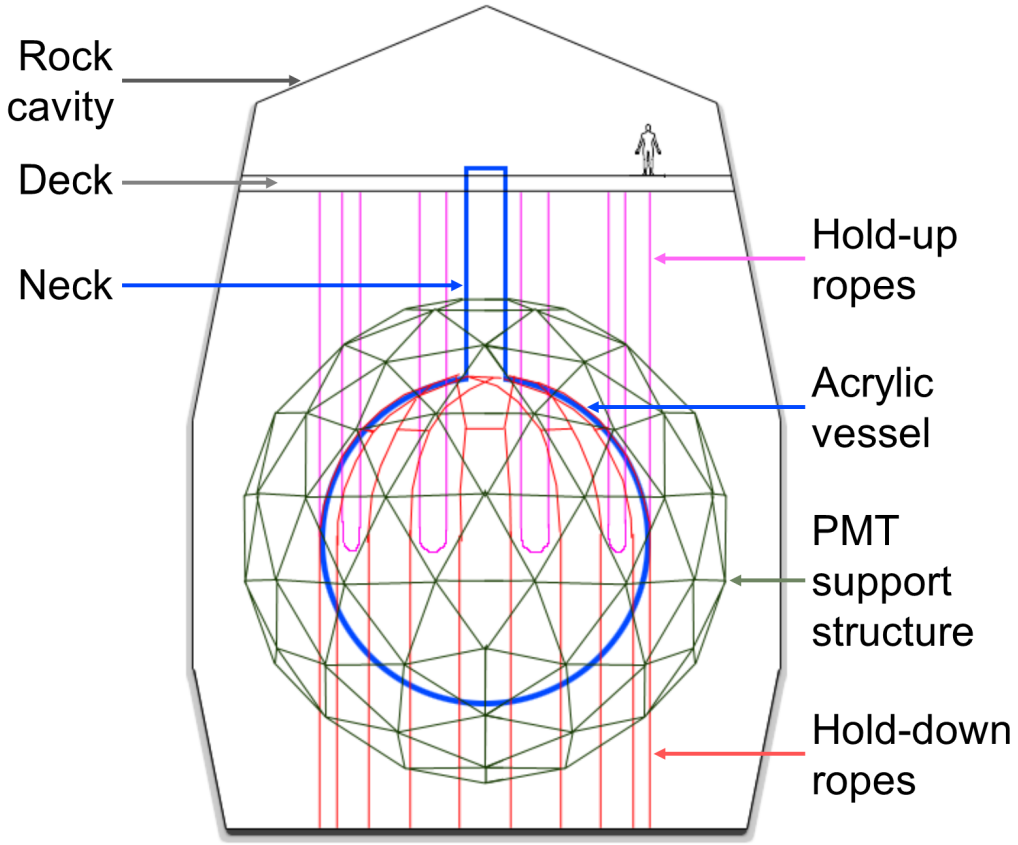


Figure 3.1: The SNO+ detector with the main structural components labeled. Modified from [60].

### 3.1.3 Differences from SNO

While the majority of the components that make up the SNO+ detector are unchanged from the SNO detector, several key upgrades have been performed:

- As liquid scintillator produces much more light than water, the overall detection rate for SNO+ is expected to be much higher than for SNO. To accommodate this rate, the electronics were upgraded to handle a higher throughput of data [63].
- While the PMTs remain the same, those that were damaged (predominately from hardware failures on the PMT bases) during the operation

of the SNO detector were repaired [64]. These repairs took place periodically as the water level surrounding the detector increased, granting access to different subsets of PMTs.

- As liquid scintillator is less dense than water, the SNO+ detector will experience buoyant forces for the first time during its operation. This necessitated the installation of hold-down ropes and the associated rope-net that counters these forces and partially covers the detector [65].
- A gas system was redesigned and installed to cover any exposed liquid scintillator with a high purity nitrogen atmosphere. This suppresses the background that would come from the radioactive decay of radon in air [61].
- Chemical plants were installed to handle the purification and processing of the LAB [61] and Te [61] that will be added to the detector. Additionally, upgrades were performed to the water purification systems.
- A series of calibration systems were designed and added. These include a series of fixed fibres coupled to lasers for optical calibrations [66] and a sealed system to store and lower radioactive sources into the detector [67].
- A system of six cameras were installed onto the PMT support structure [68]. From the high-resolution images, the positioning of the detector itself can be monitored along with that of calibration sources.

### 3.1.4 Current Status

The acrylic vessel is currently filled with water and the detector officially started its water phase of operation in May 2017. An image of the SNO+ detector, taken by the camera system, in its current operation is shown in Figure 3.2. The water phase is expected to continue until September 2018, at which point the water will be replaced with liquid scintillator.

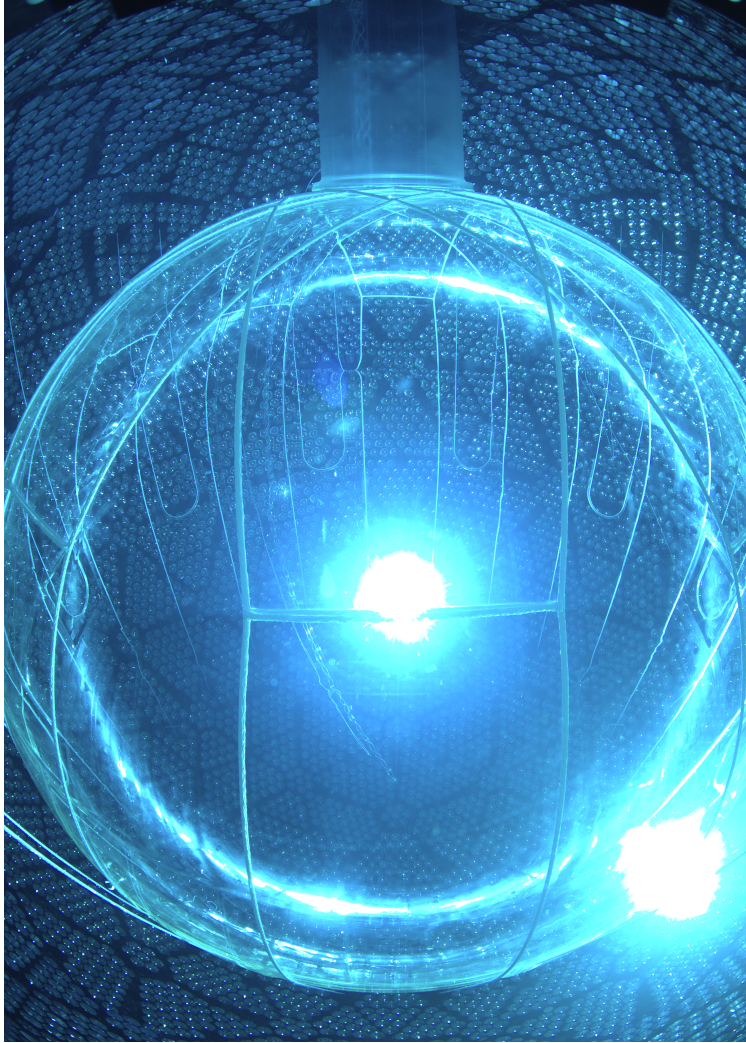


Figure 3.2: Picture of the SNO+ detector during its water phase taken by Singh using the underwater camera system on March 30, 2017 [69].

## 3.2 Physics Goals

Upon completion, the SNO+ detector's main goal is to search for the signal from  $0\nu\beta\beta$  decay. This signal is characterized by an excess of detection events at an energy of 2.5 MeV (the total energy available in  $^{130}\text{Te}$   $\beta\beta$  decay) [70]. Taking into account the expected backgrounds and detector resolution, Figure 3.3 shows what this spectrum is anticipated to look like assuming an effective neutrino mass of 100 meV.

As a large scale multi-purpose neutrino detector, the SNO+ experiment has

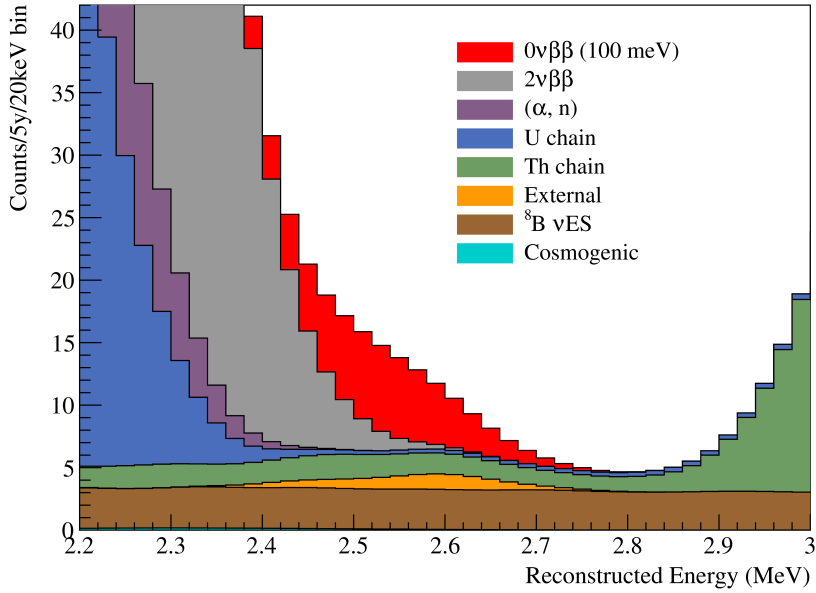


Figure 3.3: Stacked energy spectra for the  $0\nu\beta\beta$  decay signal and naturally occurring backgrounds in the SNO+ detector for a total concentration of 0.5% Te [71]. These backgrounds include natural radioactivity (U, Th, and External), induced backgrounds (( $\alpha$ ,n) and Cosmogenic), and solar neutrinos ( $^8\text{B}$   $\nu\text{ES}$ ).

an array of additional physics goals [61]. These include measurements of:

- Solar neutrinos

Measurements of  $p\text{ep } \nu$  (1.4 MeV with a well-known theoretical flux) can be used to evaluate the matter effects in neutrino oscillations (specifically in this transition range between matter and vacuum oscillations) and search for other non-standard neutrino oscillations. Measurements of  $\nu$  produced from the Carbon-Nitrogen-Oxygen (CNO) cycle could better constrain the poorly known CNO contribution to the fusion reactions in the Sun, improving our solar models [72].

- Reactor antineutrinos

SNO+'s geographic location relative to the  $\bar{\nu}_e$  flux being generated by three principle reactors (240–350 km away) results in a peaked structure

of the measured  $\bar{\nu}_e$  energy spectrum. This will allow the experiment to make a competitive measurement of the oscillation parameter  $\Delta m_{21}^2$ .

- Geoneutrinos

The interior of the Earth is heated through the energy released in the decay of radioisotopes in the earth's crust and mantle. By measuring the  $\bar{\nu}_e$  produced in the  $\beta^-$  decays, SNO+ would provide a better understanding of the heating mechanisms inside the earth.

- Supernova neutrinos

SNO+ would be able to detect many of the neutrinos produced by a nearby supernova through multiple interaction channels. This would provide direct information about the physics behind supernovae and potentially provide an alert on the SuperNova Early Warning System [73].

### 3.3 Particle Detection

#### 3.3.1 Interaction

Any charged particle that passes through a dielectric medium, with a refractive index  $n$ , at a speed greater than the local phase speed of light  $v_p$  will emit electromagnetic radiation. This radiation, called Cherenkov radiation, is emitted in a forward conical direction, with an opening angle  $\theta$  given by [74]:

$$\cos\theta = \frac{1}{n\beta} \quad (3.1)$$

This is entirely determined by the index of refraction of the medium  $n$  and the speed of the particle  $v = \beta c$ , where  $c$  is the speed of light. For a particle to emit Cherenkov radiation, its speed must satisfy:

$$v > \left( v_p = \frac{c}{n} \right) \quad (3.2)$$

For the case of water, with a refractive index  $n = 1.33$ , this corresponds to a speed of  $0.75c$  [75]. If the traveling particle is an electron, with a mass  $m$  of  $511 \frac{\text{keV}}{c^2}$ , it will require a kinetic energy  $E$  of:

$$E = (\gamma - 1) mc^2 = \left( \frac{1}{\sqrt{1 - \frac{v^2}{c^2}}} - 1 \right) mc^2 = 262 \text{ keV} \quad (3.3)$$

to create a Cherenkov photon. This minimum energy is referred to as the Cherenkov threshold. The photons are emitted with a continuous spectrum of energies, where the intensity  $I$  is proportional to the wavelength  $\lambda$  by  $I \propto \lambda^{-2}$ . This results in more light being emitted at lower wavelengths.

### 3.3.2 Detector Trigger Logic

Charged particles within the SNO+ detector are detected through the light that they produce. For the water phase of the experiment, the detector measures Cherenkov light using PMTs. A photon incident on a PMT may strike its photocathode and produce a photoelectron. This photoelectron, after passing through the PMT's dynode chain, will cause an electrical signal in the form of a voltage drop. If this is larger than a threshold value, the electronics of that PMT sends a trigger pulse.

For the SNO+ detector specifically, each PMT that triggers sends multiple trigger pulses down the electronics chain, which then performs higher logic. These include both a 93 ns long square pulse (N100) and a 48 ns square pulse (N20) [76]. These widths are chosen to match the characteristic travel times of photons across the detector. More specifically, the N100 width is chosen such that a set of photons from a Cherenkov cone will result in overlayed PMT pulses. The shorter N20 width limits this overlaying of PMT pulses to events originating from the centre of the detector.

If the total height of either of these summed pulses passes a set thresh-

old value, a global trigger (GT) is issued. This global trigger defines an “event” within the detector and results in all the associated information being saved. Multiple different trigger thresholds can be set. For example: N100Lo, N100Med, N100Hi are triggers based on the N100 pulses, where each has a different threshold value set. So it is possible, and likely, that an event within the detector passes several of these trigger thresholds.

Additionally, the detector can trigger from the charge in the PMTs directly. The voltage pulses from all of the PMTs are summed together (ESUM). If this combined voltage trace drops below a threshold value (for example, ESUMHi, ESUMLo), this can also issue a GT to the detector.

Figure 3.4 shows the event display of a typical muon event in the detector. Each individual PMT that triggered for that event is highlighted at its position on the support structure. A muon event is characterized by the large number of triggered PMTs. As with nearly all muons that pass through the detector, it is traveling in a downward direction. This is seen in Figure 3.4 as the excess of PMT charge (i.e. photons) in the bottom of the detector. As all atmospheric muons traveling upwards would be attenuated by the Earth, the small flux of upward-going muons are the result of neutrino interactions in the rock surrounding the detector [56].

Figure 3.5 shows a more typical event. The circular pattern seen is produced by the projection of the Cherenkov light cone onto the PMTs. With 24 triggered PMTs, this event is considered a high-energy event within the detector. The size of the pattern indicates that this event took place closer to the PMTs traveling in an outward direction, specifically in the water between the acrylic sphere and the PMTs.

### 3.3.3 Data Collection

During normal operation in the water phase of the experiment, the detector will collect data in periods of 1 hour. These periods are referred to as “runs”,

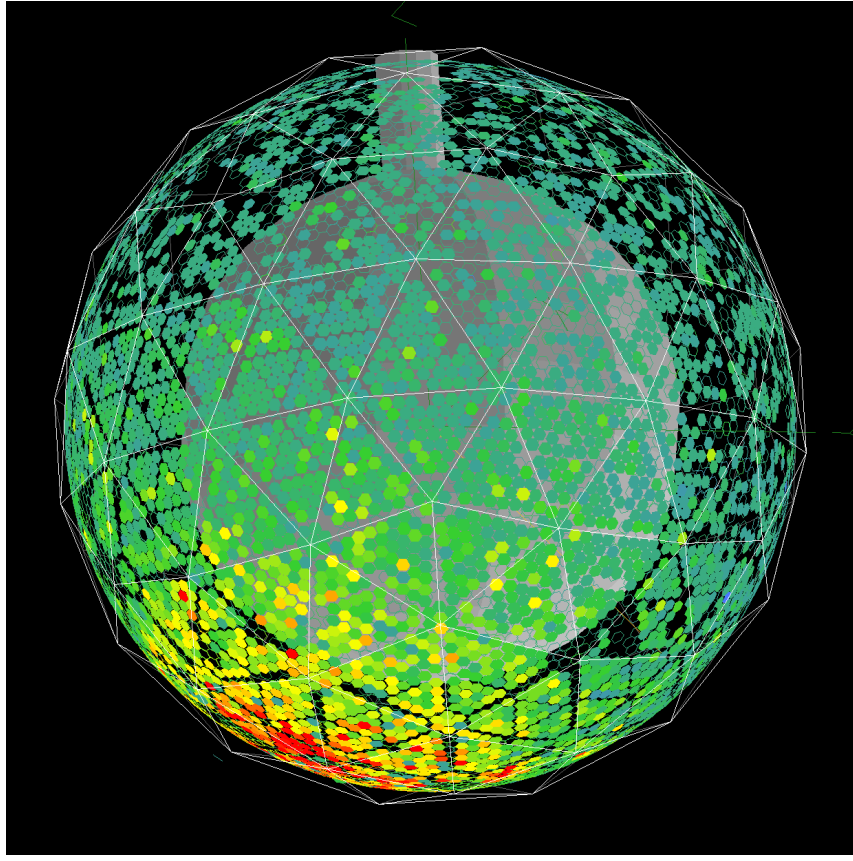


Figure 3.4: Event display of the SNO+ detector during a muon event, characterized by a large number of triggered PMTs. The colour scale indicates the charge in each PMT with red designating the largest charge and blue the smallest. Taken using XSNOED [77].

that are uniquely identified by an increasing integer (run number). Following the completion of a run, the detector automatically starts the next run, such that there is no data loss between runs. Additionally, the exact state of the detector (including information about each individual PMT) is recorded and stored within a database.

### 3.3.4 Event Reconstruction

The information that defines an event within the detector consists of the PMTs that triggered and the time at which they did so. The total charge recorded by each PMT is generally less important in the case of a water-filled detector,

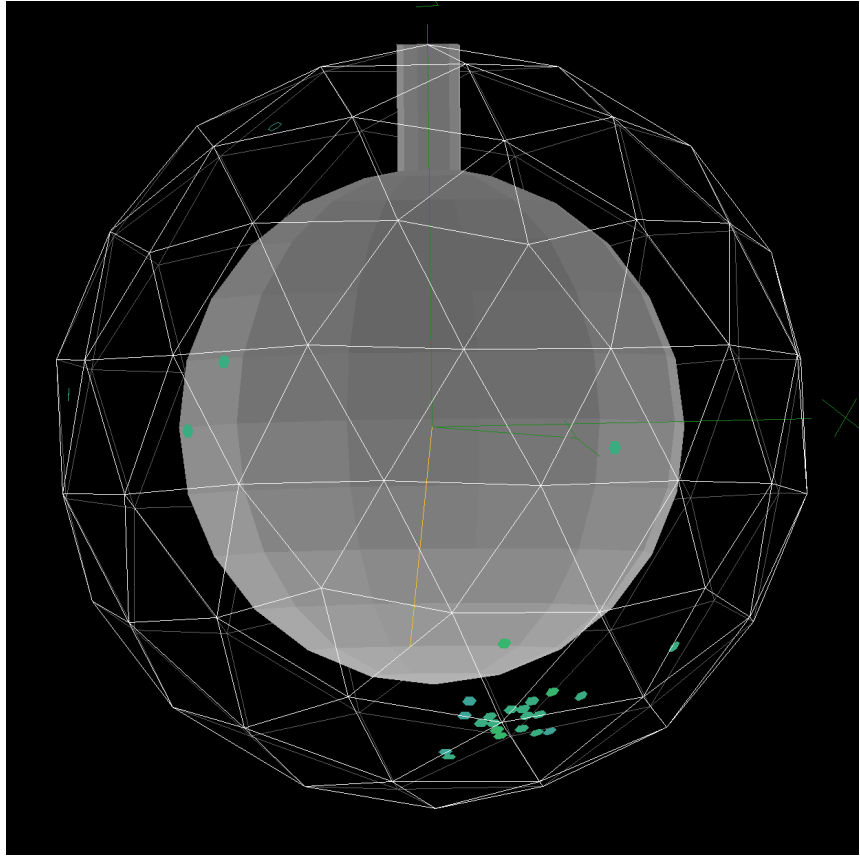


Figure 3.5: Event display of the SNO+ detector during a common triggered event. The colour scale indicates the charge in each PMT, where here it is consistent with each PMT detecting a single photon. Taken using XSNOED [77].

as in each event the likelihood of a PMT recording more than one photon is negligible. This is a consequence of the low number of Cherenkov photons that are emitted from  $O(\text{MeV})$  charged particles within the detector. In the scintillator-filled phases of the experiment, where a large amount of light is produced for these same particles, this will no longer be true. However, the number of photons detected at each PMT can be determined from the measured charge.

From this saved information, software algorithms have been developed to reconstruct the momentum, energy, and position of the particle that caused that event. These reconstructed properties enable searches for specific particle in-

teractions. For this analysis (Chapters 5–8), the reconstructions are performed using the University of Alberta developed “Alberta Fitter” [78]. This algorithm was used to reconstruct the  $(x, y, z)$  position of the particle interaction point within the detector and the direction that the particle was traveling. The time of interaction was also determined. This algorithm determines an event’s position by maximizing the likelihood of the hit times of each PMT. The energy of the particle interaction was not reconstructed using this algorithm as the computational load required was too high compared to the knowledge gain (as the number of triggered PMTs is a good proxy for energy in a water-filled detector).

## 3.4 Antineutrinos in SNO+

### 3.4.1 Local Sources

The majority of the  $\bar{\nu}_e$  that pass through the SNO+ detector in any given moment are produced from the  $\beta^-$  decay in the cores of nuclear reactors. As the flux scales with distance  $d$  as  $d^{-2}$ , most of these  $\bar{\nu}_e$  will originate from the closest nuclear reactors. In the case of the SNO+ detector, approximately 60% of this  $\bar{\nu}_e$  flux comes from the three closest power reactors (the Bruce, Pickering, and Darlington Nuclear Generating Stations). These three reactors are all Canada Deuterium Uranium (CANDU) reactors, a type of PHWR. Figure 3.6 shows the exact geographical layout. The remainder of the flux has contributions from reactors around the globe, but similarly it is dominated by those next closest reactors in the United States (also shown in Figure 3.6). The exact thermal powers and distances for these closest reactors are summarized in Table 3.1.

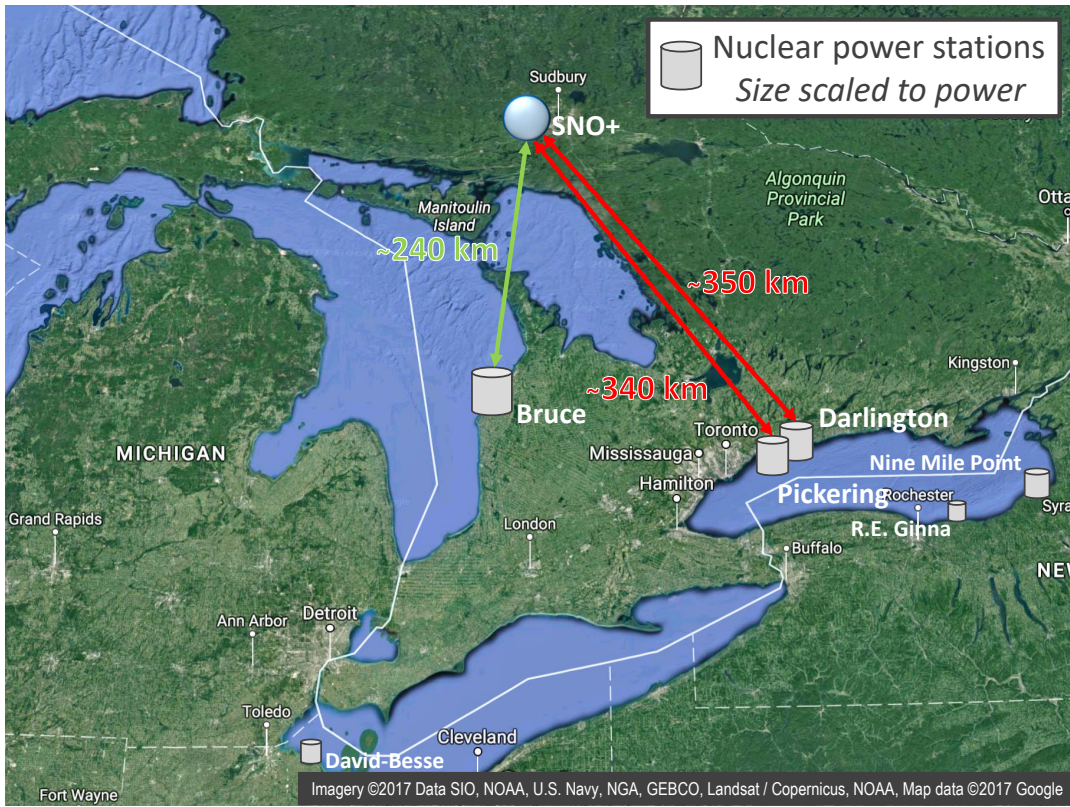


Figure 3.6: Map of the nuclear power reactors around the SNO+ detector. The three closest reactors (providing approximately 60% of the total antineutrino flux) are shown with their distances to the detector.

Nuclear Reactor	Distance [km]	Thermal Power [MW]
Bruce	240	21384
Pickering	340	10464
Darlington	349	11104
R.E. Ginna	470	1775
Nine Mile Point	500	5838
Davis-Besse	563	2817

Table 3.1: Summary of the thermal powers and distances to the SNO+ detector for the closest nuclear power reactors. Thermal powers are from [79].

### 3.4.2 Interaction Expectations

The product of the reactor-produced antineutrino energy spectrum with the energy-dependent cross-section for the IBD interaction, previously shown in Figure 2.4, gave an example of the energy spectrum of the  $\bar{\nu}_e$  as they interact (corresponding to what a detector would measure). This example is for a single nuclear reactor. Knowing the total number of antineutrinos produced from that reactor  $N(E)$  (Equation 2.2), at a distance  $L$  from a detector, the flux of antineutrinos passing through the detector can be determined:

$$\Phi_{\text{detector}}(E) = \frac{N(E)}{4\pi L^2} \quad (3.4)$$

This treats the reactor as a point-like source in relation to the detector. The rate  $R$  of antineutrinos that interact from this one reactor can be simply determined from this flux, the cross section  $\sigma(E)$ , and the number of targets (free protons) in the detector  $n_p$  as:

$$R(E) = \Phi_{\text{detector}}(E) \times \sigma(E) \times n_p \quad (3.5)$$

To determine the exact number that are expected to interact within the SNO+ detector (and their spectral shape), this calculation needs to be performed separately for all nuclear power reactors. This requires the knowledge of all of the possible contributing reactors. This information is provided by the International Atomic Energy Agency's (IAEA) Power Reactor Information System (PRIS) [79]. The information regarding the 450 power reactors that are currently operating includes each reactor's latitude, longitude, reactor type, thermal power, and load factor. These reactors are located around the world, but are predominately in the northern hemisphere.

Completing this calculation and summing over all possible reactors, the total number of antineutrinos that would interact in the SNO+ detector is

determined to be 208 per year. The energy spectrum of these  $\bar{\nu}_e$  can be seen in Figure 3.7 with the illustrated contributions from the different reactors.

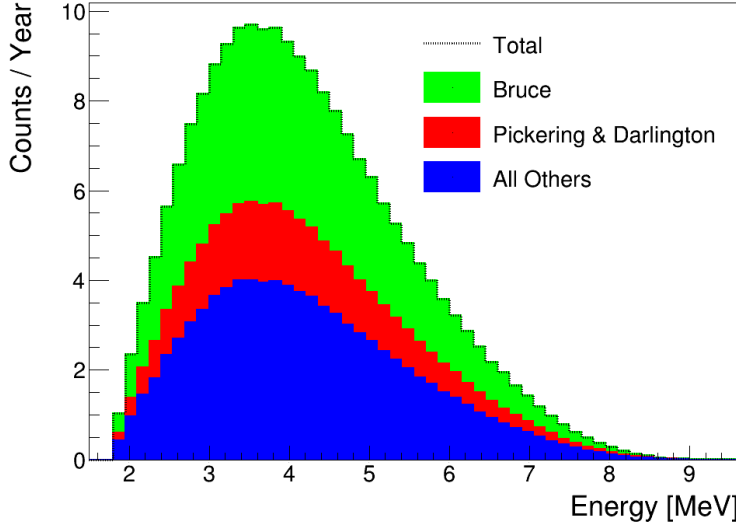


Figure 3.7: Energy of the  $\bar{\nu}_e$  that interact via IBD in the SNO+ detector. The stacked contributions from different sets of reactors to the spectrum are shown.

As the  $\bar{\nu}_e$  travel 100's – 1000's of kilometres before interacting in the detector, the relative phase of the three mass states changes. At the detector, this can result in the antineutrinos interacting as a different flavour. However, only  $\bar{\nu}_e$  can interact via the IBD reaction. As a consequence of neutrino oscillations, the overall probability of interaction is lowered. Applying the probability for oscillation using Equation 2.7 and the oscillation parameters from the Particle Data Group [41], the total estimated number of  $\bar{\nu}_e$  that are expected to interact in the detector decreases to 115 per year.

This expectation can also vary depending on the models used to calculate it. Previous work by Asahi [80] evaluated the effects of different reactor antineutrino energy spectra models, energy per fission  $Q_i$  calculations, and power fraction  $p_i$  values. Using the  $Q_i$  values as determined by the Bugey experiment [81] and those calculated by Ma et al. [82] resulted in a 0.4% difference in the total expectation. Similarly, using the power fractions  $p_i$  determined

by Baldoncini et al. [83] and those received via private communication with Atomic Energy of Canada Limited gives a 0.8% difference. Lastly, the reactor spectra models from Huber [84], Muller et al. [85], and the ILL+Vogel [86, 87] model showed a variation of 3.8% in the total expected flux.

Additionally, as nuclear fuel is “burned” the power fraction of the isotopes that make up the fuel changes. This can change the flux of antineutrinos that is emitted, and can result in a emission rate that changes with time. This time-variation is less prevalent for the case of CANDU reactors, where “online refueling” is performed [88]. In this scheme, individual fuel bundles are regularly replaced within a reactor core without shutting down the reactor. This results in a more stable neutrino emission rate over time. Similar work by Asahi [89] has evaluated the effects of these time-varying isotope fractions. This was found to have up to a 4% effect on the total flux of antineutrinos produced from a reactor core. Taking these studies into account, the systematic uncertainty on the flux of antineutrinos is estimated and corresponds to 6 interactions per year. Therefore, the expected number of interactions in the SNO+ detector is  $115 \pm 6$  per year.

As the oscillation probability is energy and distance dependent, the shape of the energy spectrum needs to be calculated. Figure 3.8 shows this energy spectrum after neutrino oscillations for the different reactors. As a result of the neutrino oscillation calculations, a three-peaked structure emerges. Looking back to Figure 2.5, this peaked structure comes from the deficits seen in the survival probability of  $\bar{\nu}_e$  with energies of approximately 3.0 and 4.5 MeV.

These features in the oscillated energy spectrum are the result of the  $\sin^2 \Delta_{21}$  term, this will allow SNO+ to make a precision measurement of  $\Delta m_{21}^2$  (as it is the only unknown that creates this spectral shape). It is expected that after 7 years of data taking with liquid scintillator, SNO+ will be able to measure  $\Delta m_{21}^2$  to a precision of  $0.2 \times 10^{-5}$  eV $^2$  [59]. This is comparable to the latest accepted value ( $7.50^{+0.19}_{-0.20} \times 10^{-5}$  eV $^2$ ), as determined by the KamLAND experiment [90]

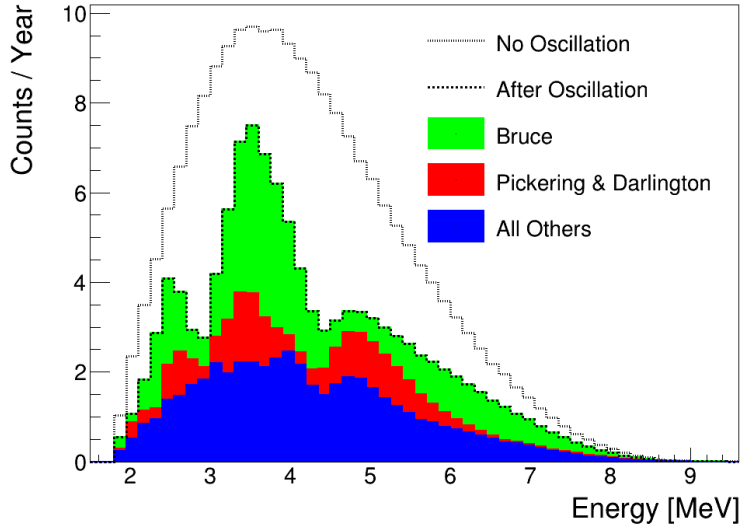


Figure 3.8: Energy of the  $\bar{\nu}_e$  that interact via IBD in the SNO+ detector. The spectra before and after neutrino oscillations are shown. The stacked contributions from different sets of reactors to the oscillated spectrum are also illustrated.

(over a 7 year period of data acquisition).

The determination of  $\Delta m_{21}^2$  is less sensitive to uncertainties in the flux and energy spectrum of antineutrinos emitted from the nuclear reactors. These uncertainties directly correspond to the rate of interactions and will therefore produce a comparably large uncertainty in the determination of  $\sin^2 \theta_{12}$ . For this reason, experiments that are designed to measure mixing angles  $\theta_{ij}$  will typically have multiple detectors (at different distances) measuring one neutrino source. By taking the measured ratio between the detectors,  $\theta_{ij}$  can be precisely determined with larger flux uncertainties. However,  $\Delta m_{21}^2$  determines the width of the peaks seen in Figure 3.8. These MeV-scale features are affected very little by changes in the unoscillated energy spectrum (at neutrino emission).

## Geoneutrinos

Along with  $\bar{\nu}_e$  that are produced in nuclear reactors, there will be  $\bar{\nu}_e$  produced from geoneutrino sources that will interact in the SNO+ detector. Geoneutri-

nos that interact via IBD have energies ranging from 1.8–3.3 MeV. Previous work by Lan [91] has shown that the number of geoneutrinos that will interact in the SNO+ detector is approximately equal to the number of those from reactors in this energy range; however, during the water phase of the SNO+ experiment, their contribution to the expected signal from all antineutrinos will be negligible. This is due to the lower energies of these  $\bar{\nu}_e$  compared to those from reactors. The lower energy  $e^+$  produced by the IBD interactions will be close to or below the Cherenkov threshold. As a consequence, very little light will be produced, making the likelihood of detecting such events low. Lastly, for the later analysis of the water-filled detector data, the chosen data selection cuts entirely exclude any possible contribution from geoneutrinos.

### 3.4.3 Inverse Beta Decay in SNO+

In order to perform this determination of  $\Delta m_{21}^2$ , the energy spectrum of the interacting neutrinos needs to be measured. For IBD, the SNO+ detector measures two events: one from the initial  $e^+$  and a second from the delayed neutron. In the case of an IBD interaction, the energy of the  $e^+$  is highly correlated to the energy of the  $\bar{\nu}_e$ . As the amount of the kinetic energy transferred to the neutron is small, the energy of the  $\bar{\nu}_e$  can be simply determined as:

$$E_{\bar{\nu}_e} \approx E_{e^+} + M_p - M_n - m_e \quad (3.6)$$

where  $E_{e^+}$  is the measured energy of the positron and  $M_p$ ,  $M_n$ , and  $m_e$  the mass of the proton, neutron, and electron, respectively. Therefore, the energy of the  $\bar{\nu}_e$  is entirely determined from the energy of the  $e^+$ . However, as there are many backgrounds that also occur in this energy range of 2–10 MeV, it becomes important to be able to distinguish the signal from this  $e^+$  from that of any other source.

As such, it is critical to detect the events from the neutron. After a neu-

tron is emitted, it will capture on a nucleus within a characteristic time scale  $O(100 \mu\text{s})$  [92,93]. By detecting a neutron shortly after a first high energy event in the detector, the pair of events can be identified as an IBD interaction. The neutron then is the key element that will allow one to identify a  $e^+$  event in the SNO+ detector as one from a  $\bar{\nu}_e$ . This coincident signal of a  $e^+$  and neutron is the foundation of reactor antineutrino detection for the current generation of such experiments. These experiments will be briefly discussed along with the SNO+ detector's role in this field. The exact search for this signal in the SNO+ detector will be described in detail in Chapter 5.

## 3.5 Current Reactor Antineutrino Experiments

The current generation of reactor antineutrino experiments rely on using IBD to make measurements. The elastic scattering interaction may also be used to detect antineutrinos, however it has a lower cross section and consequently lower event rate ( $O(10)$  lower) [42]. Additionally, the lack of a coincident signal and poorer antineutrino energy determination make it harder to distinguish the antineutrinos from backgrounds. A typical reactor antineutrino experiment will search for the coincident signal of a  $e^+$  and neutron. To distinguish this signal from backgrounds, different strategies are employed.

### 3.5.1 Detection Strategies

#### Neutron Capture Isotopes

An isotope with a high neutron capture cross section can be added into the active volume of the detector, resulting in multiple benefits. The average time it takes for a neutron to capture will decrease, enabling the use of a shorter coincidence time window. This decreases the probability of background events occurring within this time. The neutron capture isotopes are chosen such that

they produce high energy  $\gamma$  rays, increasing the neutron detection efficiency and allowing the neutron signal to be more easily distinguishable from backgrounds. Examples include gadolinium, producing an 7.9–8.5 MeV cascade of  $\gamma$  rays [94], and salt, where neutron capture on chlorine similarly produces up to 8.6 MeV of  $\gamma$  rays [95].

### Active Volume

Most reactor antineutrino experiments will employ the use of a scintillator. For large-scale liquid scintillator experiments, many more photons will be produced than for pure water detectors. For the same event in the SNO+ detector, 40 times more PMTs will detect light during its scintillator phase as compared to its water phase [96, 97]. These increased statistics provide much better detector resolutions and more easily allow for the discrimination of the 2.2 MeV  $\gamma$  ray from neutron capture on hydrogen, which may otherwise be at the detection threshold (in a pure water detector).

### Proximity

Dedicated reactor antineutrino experiments are typically situated close to nuclear power reactors,  $< 2$  km away [98]. This provides a much greater flux and allows the detectors to be considerably smaller than those located 100's of km away. At these distances, the oscillation of antineutrinos is driven by the change of  $\bar{\nu}_e$  to  $\bar{\nu}_\tau$ , enabling these experiments to make precision measurements of  $\theta_{13}$  [17].

### 3.5.2 Current Experiments

Experiments that have made measurements of reactor antineutrinos will employ one or more of these strategies. For example, Borexino (a spherical 8.5 m diameter detector with 2212 PMTs providing 34% coverage [99]) and

KamLAND (a spherical 13 m diameter detector with 1879 PMTs also providing 34% coverage [15]) are both liquid scintillator experiments. They have made measurements of reactor antineutrinos from reactors located 100–1000 km away [40, 100].

At close distances, the Daya Bay experiment has made precision measurements of oscillation parameters [17] and the energy spectrum of incoming antineutrino flux [101]. It consists of 6 gadolinium-doped LAB-based liquid scintillator detectors, at distances of 0.4–2.0 km [102] from nearby reactors. Similarly, RENO [103] with 2 detectors at 0.3 and 1.4 km, and Double CHOOZ [104] at 0.4 and 1.0 km also use gadolinium-doped liquid scintillator.

### SNO+ Experiment’s Role

When commissioned, the SNO+ detector will join KamLAND and Borexino, as another large scale liquid scintillator detector and begin making measurements of antineutrinos. This will be crucially important as the two most recent determinations of  $\Delta m_{21}^2$  disagree. These include the measurements by the KamLAND experiment through reactor antineutrinos ( $7.50^{+0.19}_{-0.20} \times 10^{-5}$  eV $^2$ ) [100] and the Super-Kamiokande experiment through solar neutrinos ( $4.85^{+1.33}_{-0.59} \times 10^{-5}$  eV $^2$ ) [105]. The SNO+ detector will be able to provide another independent measurement of  $\Delta m_{21}^2$  and help to resolve this current tension (approximately a  $2\sigma$  disagreement).

# **Chapter 4**

## **Neutron Measurements and Modeling**

Accurately simulating the neutron and its interaction through the SNO+ detector is essential to performing the search for antineutrinos by looking for the IBD reaction. In order to evaluate the accuracy of the model, a series of neutron measurements were performed in the low-background radiation laboratory at the University of Alberta. A new simulation of the detector used for these measurements was simultaneously developed. This simulation was based on the same Geant4 physics modeling packages [106] used in the SNO+ simulation. Through a series of comparisons, the accuracy of modeling neutrons using Geant4 was verified for the use in the SNO+ experiment.

### **4.1 Neutron Measurements**

#### **4.1.1 Neutron Source**

The neutrons used for this experiment were produced from an americium-beryllium (AmBe) neutron source. This type of neutron source uses the  $^{9}\text{Be}(\alpha,\text{n})$  reaction as the main production mechanism. The alpha particles that initiate

this reaction are produced from the decay of  $^{241}\text{Am}$ . The neutrons that are produced in this reaction will have energies ranging up to 11 MeV, with the energy spectrum shown in Figure 4.1. Along with the emission of a neutron, the  $^9\text{Be}(\alpha, n)$  reaction produces a  $^{12}\text{C}$  atom that will also emit a 4438 keV  $\gamma$  ray ( $57.8 \pm 2.8$ ) % of the time [107].

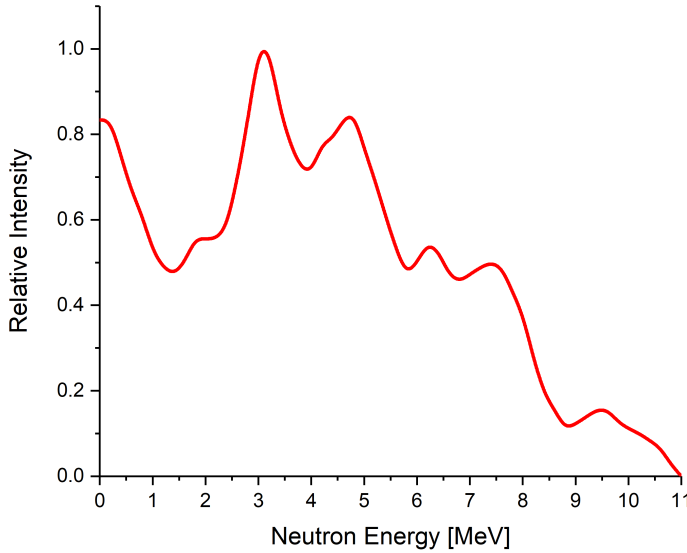


Figure 4.1: Energy of the neutrons produced from the  $^9\text{Be}(\alpha, n)$  reaction in an AmBe neutron source [108].

The specific AmBe source used in this experiment was an AM241SNA02 source produced by Eckert & Ziegler Isotope Products, Inc. The centre of the source consists of a powdered mixture of americium oxide and metallic beryllium. This mixture is encapsulated in two layers of stainless steel, where each layer is 0.8 mm thick. The source has an activity specified by the manufacturer for the  $^{241}\text{Am}$  of 5.5 MBq. However, there is no listed precision on this activity nor is there a specified neutron activity.

### 4.1.2 Neutron Reactions

In this experiment, the neutrons are not measured directly, but rather the products from neutron-induced reactions are measured. Materials are placed between the neutron source and the detector to serve as “targets” for these reactions, which include  $(n,n')$ ,  $(n,p)$ , and  $(n,\gamma)$  reactions.

Considerations made in the selection of these target materials were:

- The cross section of the different neutron reactions and the energy region over which each reaction dominates. The cross sections needs to be sufficiently high over the energies of neutrons produced by the AmBe source.
- The structure of the nuclear energy levels of the isotopes in the target material. In the case of the  $(n,n')$  reaction, energy levels that are not closely spaced are desirable. This allows any emitted  $\gamma$  rays to be fully resolved by the detector.
- The lifetimes of any unstable products produced in the neutron reactions. In the case of the  $(n,p)$  and  $(n,\gamma)$  reactions that produce unstable isotopes, the lifetimes must be sufficiently short so that enough isotopes decay over the time period of the measurements.
- The ability of the material to serve as a neutron moderator (i.e. a high relative elastic scattering cross section).
- The availability and cost of the materials for a kilogram-scale experiment.

As a result, aluminum and acrylic were chosen as target materials. The specific reactions that were observed in the measurements were:

- $^{27}\text{Al}(n,n')$  — A neutron inelastically scatters off of a  $^{27}\text{Al}$  nucleus leaving it in an excited nuclear state. The  $^{27}\text{Al}$  nucleus then decays back to the ground state (on a ps timescale) through the emission of  $\gamma$  rays. Each

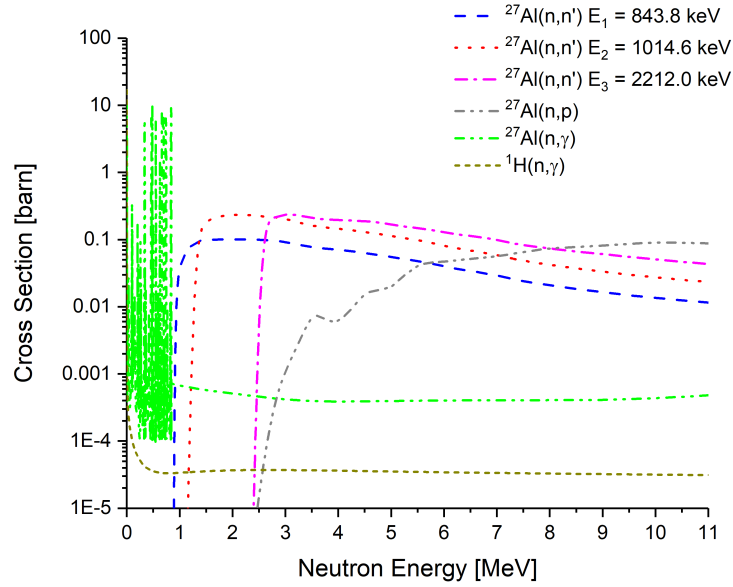
individual energy level of  $^{27}\text{Al}$  will have a different  $(n,n')$  cross section. Additionally, as a neutron needs sufficient energy to transfer to the nucleus to put it into each excited state, these reactions will have threshold energies (minimum 875 keV) [109].

- $^{27}\text{Al}(n,p)$  — A neutron captures on a  $^{27}\text{Al}$  nucleus and a proton is emitted. This creates an unstable  $^{27}\text{Mg}$  atom that will  $\beta^-$  decay to  $^{27}\text{Al}$  (half-life of 9.5 minutes). This reaction also has a threshold energy (1897 keV) as sufficient energy is required to produce the  $^{27}\text{Mg}$  isotope [110].
- $^{27}\text{Al}(n,\gamma)$  — A neutron captures on a  $^{27}\text{Al}$  nucleus producing an unstable  $^{28}\text{Al}$  atom.  $^{28}\text{Al}$  will  $\beta^-$  decay to  $^{28}\text{Si}$  (half-life of 2.2 minutes). This reaction has no threshold energy.
- $^1\text{H}(n,\gamma)$  — A neutron captures on a free proton ( $^1\text{H}$  atom) producing a deuteron ( $^2\text{H}$  atom). A  $\gamma$  ray is emitted with energy equal to the binding energy of the deuteron (2224 keV) [111]. This reaction also has no threshold energy.

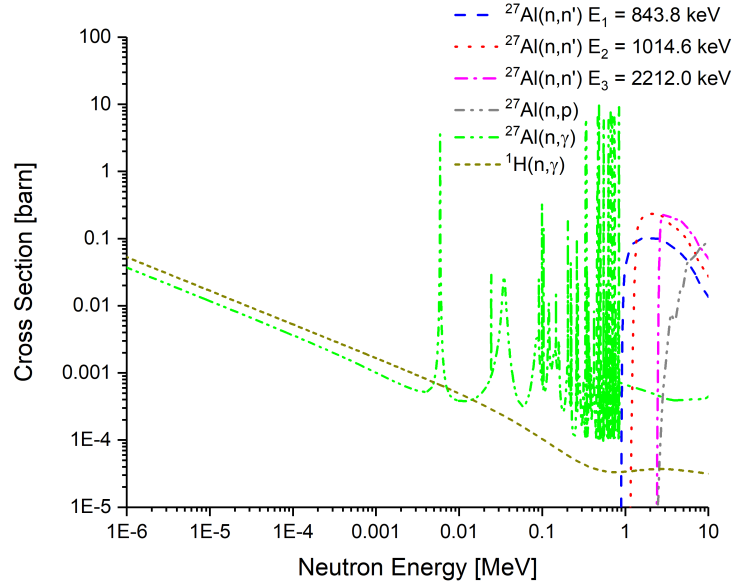
The cross sections of these four different neutron reactions are shown in Figure 4.2. It can be seen that these reactions will dominate over different ranges of neutron energies. Here the  $^{27}\text{Al}(n,n')$  and  $^{27}\text{Al}(n,p)$  reactions will be the primary reactions for neutrons with energies around 1 MeV and greater (referred to as “fast neutrons”). The  $^{27}\text{Al}(n,\gamma)$  and  $^1\text{H}(n,\gamma)$  reactions will be the only reactions for neutrons with energies in the eV scale (referred to as “thermal neutrons”). In the resonance region (1 keV – 1 MeV), the  $^{27}\text{Al}(n,\gamma)$  reaction can also be seen to be the dominant reaction.

### 4.1.3 Experimental Setup

All measurements performed in this experiment used a high purity germanium (HPGe) detector. HPGe detectors are the industry standard for making pre-



(a)



(b)

Figure 4.2: Cross sections of the different neutron reactions targeted by this experiment, shown with both a linear (a) and logarithmic (b) neutron energy scale [110].

cision  $\gamma$  ray energy measurements. The specific detector setup used was a GC12023 HPGe detector manufactured by Canberra Industries. A Canberra Lynx digital signal analyzer was used to acquire data from the HPGe detector.

The HPGe detector itself includes a cylindrical germanium crystal measuring 87.1 mm in diameter and 90.1 mm in length. It is centrally located within a cylindrical 101.6 mm diameter aluminum end cap. The end cap maintains the vacuum between the crystal (which requires cooling with liquid nitrogen for operation) and the surroundings that are at room temperature. The detector is then located at the centre of a nested rectangular shield. This shield has a 25.4 mm thick inner layer of copper and a 25 cm thick outer layer of lead. These different components can be seen in Figure 4.3. Figure 4.4 contains a photograph of the actual detector system and includes the cryogenic systems and electronics.

#### 4.1.4 Measurement Details

Each measurement was performed by irradiating a target (aluminum and/or acrylic) with neutrons from the AmBe source. This was followed by measuring the energies of any  $\gamma$  rays produced in neutron reactions with the targets using the HPGe detector. As a result of the low activity of the neutron source and the short lifetimes of the reaction products, both the source and targets needed to be placed on the detector for measurements. This simultaneous irradiation and measurement represents a prompt-gamma neutron activation analysis (PGNAA) approach [113].

A total of seven different geometric configurations of the source and targets were used for measurements. By varying the amount of acrylic in any configuration, the energy of the neutrons that initiate the reactions was changed. The high hydrogen content enables the acrylic to act as a neutron moderator. Each subsequent elastic scatter off of an atom lowers the energy of the neutron. By increasing the amount of acrylic in the configuration, the energy at which the

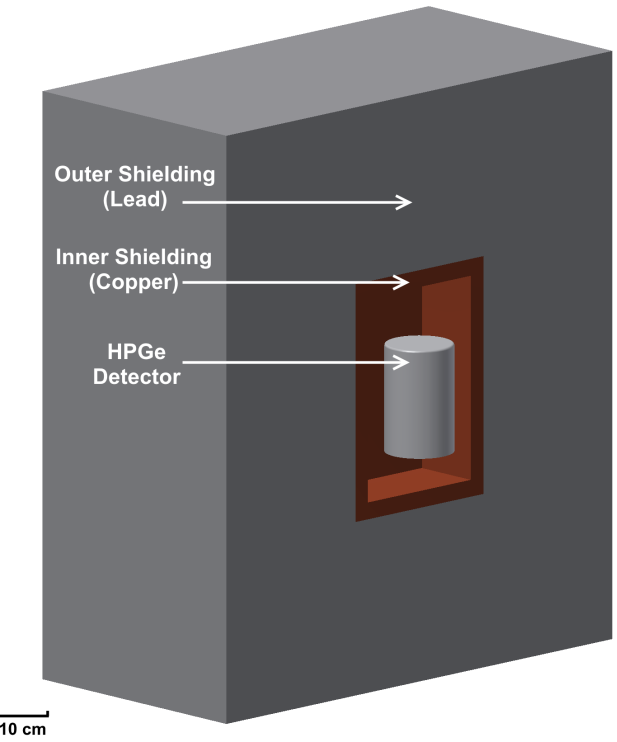


Figure 4.3: Cross sectional view of the HPGe detector system used. These different primary components are shown to scale [112].

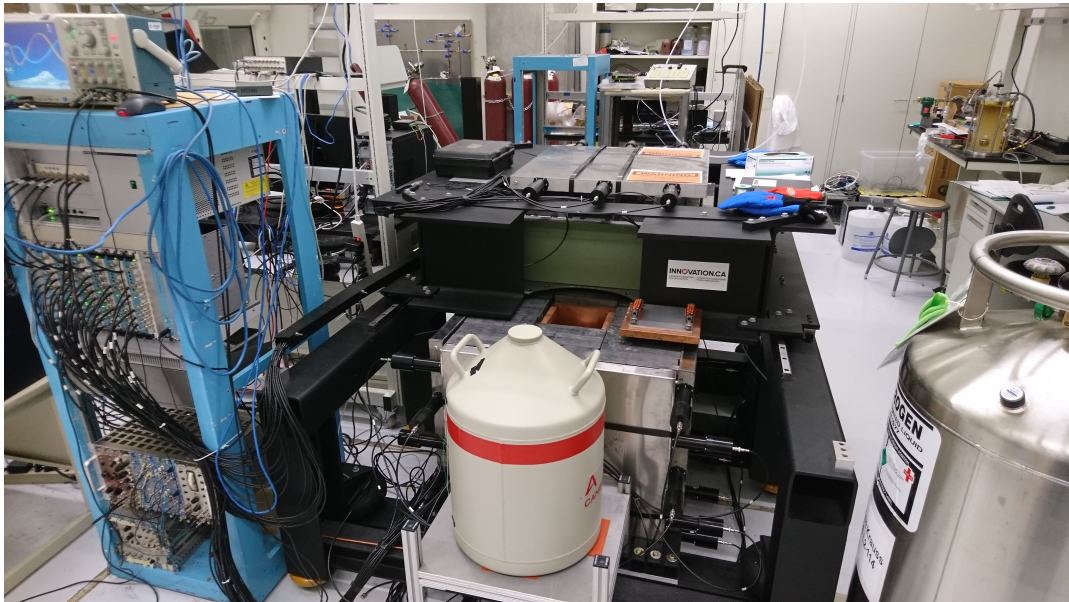


Figure 4.4: Photograph of the actual detector system used for the measurements, including shielding, cryogenics, veto panels, and electronics.

neutrons interact was effectively lowered. This permitted for a more thorough investigation of neutron interactions and resulted in a series of independent measurements.

The specific targets used in the measurements included one aluminum disk, measuring 17.7 cm in diameter and 2.7 cm in height, and six acrylic disks, each measuring 19.0 cm in diameter and 1.2 cm in height. One of the acrylics disks had a central 1.0 cm hole in which the neutron source could be placed, when necessary. The amount of neutron moderation in the measurements was varied by including a different number of acrylic plates in each geometric configuration. The exact details of the seven configurations measured are illustrated in Figure 4.5.

The result of any one measurement with the HPGe detector is a single energy spectrum with peaks corresponding to different  $\gamma$  rays, some of which are the result of neutron reactions that took place. Each measurement was performed for a period of approximately 24 hours.

#### 4.1.5 Background Measurements

Any given  $\gamma$  ray peak in the energy spectrum (with an activity  $A_{\text{meas}}$  equal to the number of counts  $N$  over the counting period  $t$ ) will also contain contributions from various background sources. There are two main sources of background for a given measurement:

- $\gamma$  rays produced from radioactivity in the detector system or the AmBe source, as well as  $\gamma$  rays produced from other neutron reactions in non-target materials.
- $\gamma$  rays produced by the neutron reactions in the target material induced by ambient neutrons naturally present in the laboratory [114].

To properly evaluate the accuracy of the neutron model, the measured energy spectra must be restricted to contain only  $\gamma$  rays produced from source

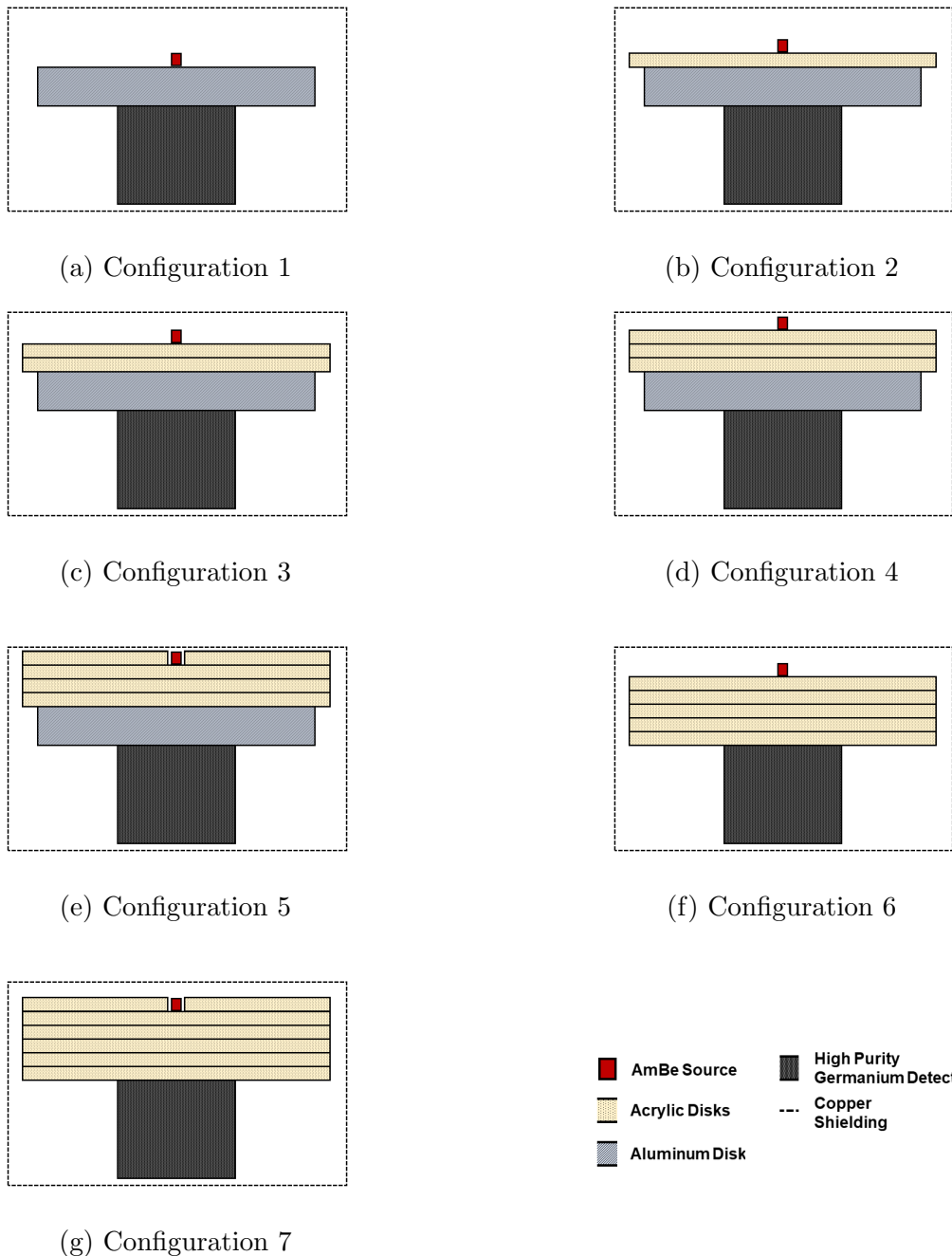


Figure 4.5: Diagrams of the seven different configurations. Each corresponds to a separate measurement that was performed with the HPGe detector system.

neutrons that interacted in the target materials. This is required as the developed model only simulates neutrons produced by the AmBe source. To do this, the activity in the peak contributed by background  $\gamma$  rays ( $A_{\text{bkgd}}$ ) and ambient neutrons ( $A_{\text{lab}}$ ) must be measured separately. The activity due to only the neutrons from the AmBe source interacting on the designated target material ( $A_{\text{reaction}}$ ) is then simply:

$$A_{\text{reaction}} = A_{\text{meas}} - A_{\text{bkgd}} - A_{\text{lab}} \quad (4.1)$$

By performing more measurements with slightly different geometric configurations, for each of the seven  $A_{\text{meas}}$ :

- $A_{\text{bkgd}}$  was determined by remeasuring the configuration, but without the target material. In this case a thin hollow cardboard spacer is used in place of the removed target(s) in order to maintain the same placement of the AmBe source and moderators.
- $A_{\text{lab}}$  was determined by repeating the measurement with the same original configuration, but without the AmBe neutron source.

An illustration of each original measurement  $A_{\text{meas}}$  with its associated  $A_{\text{bkgd}}$  and  $A_{\text{lab}}$  measurements can be seen in Figure 4.6.

#### 4.1.6 Peak Activity Determination

Following this series of measurements, a new energy spectrum is constructed by taking the energy spectra of the  $A_{\text{meas}}$  measurements and subtracting those of the associated  $A_{\text{bkgd}}$  measurements. This results in a set of background-subtracted energy spectra, where any remaining peaks are due to neutron reactions. To obtain the activities for any given peak, a linear baseline is first fit around each individual peak. The peak above the baseline is then integrated.

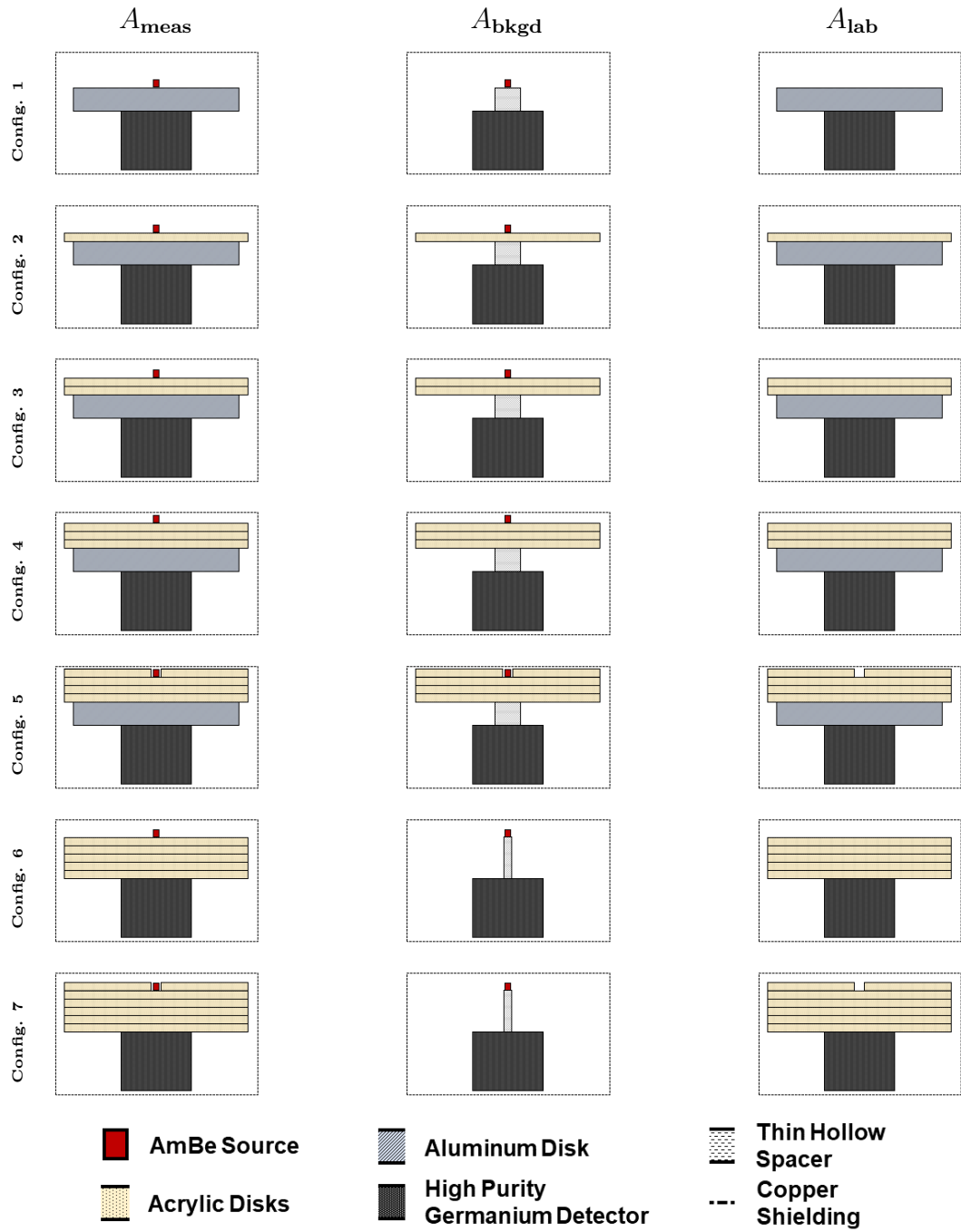


Figure 4.6: Diagrams of all the different configurations. The second and third columns illustrate the determination of the relevant backgrounds for each of the seven previous measurements (shown again in the first column). Each configuration represents a separate measurement that was taken with the detector system.

This gives an activity for that peak ( $A_{\text{meas}} - A_{\text{bkgd}}$ ), that contains contributions from all neutron sources.

Finally, any contribution to that peak from ambient neutrons is removed. If a peak is seen in an energy spectrum for the  $A_{\text{lab}}$  measurements, it is integrated and this value is subtracted from the previous background-subtracted energy spectrum. The value of  $A_{\text{lab}}$  was seen as a small correction in the case of the  $^1\text{H}(\text{n},\gamma)$  reaction for configurations 6 and 7 (at 1.2%–1.6% of the value of  $A_{\text{meas}} - A_{\text{bkgd}}$ ). For the remaining reactions and geometries, the contribution from these neutrons was negligible.

This results in a value of  $A_{\text{reaction}}$  for each individual peak in each of the energy spectra. Each peak corresponds to a specific neutron reaction induced by the AmBe source neutrons in the target materials. Each observed reaction will be discussed in detail in Sections 4.3.1–4.3.3.

## 4.2 Simulation

Simulations of the laboratory measurements taken with this detector system were performed using Geant4, version 4.10.0 patch-02 [106]. To simulate an experiment, the user must define the geometry of all components involved, specify the physics processes that may occur, and program the data collection during the particle tracking. These key aspects of the model will be described.

### 4.2.1 Geometry Definition

It is crucial to define all components within the simulation as accurately as possible. This includes the definition of all physical dimensions and materials. The simulation includes the HPGe detector (and its internal components), target materials, neutron source, and the copper and lead shielding. Any external dimensions were measured, whereas the internal components of the HPGe detector were modeled according to the data sheet included from the manufac-

turer for this specific detector.

Additionally, the source of the initial particles must be defined. For this simulation, neutrons were defined to be generated isotropically originating uniformly from within the central powder region of the AmBe source. The neutrons were generated with energies sampled from the distribution in Figure 4.1.

### 4.2.2 Physics Processes

Any physics process that could occur in the laboratory measurement must be defined within the simulation. For this model, the “Standard Electromagnetic” package was invoked to handle the interaction and transport of any  $e^-$  and  $\gamma$  rays. The decay of any unstable isotopes generated by neutron interactions was modeled using the “Radioactive Decay” physics package. This includes the production of any decay products until a stable isotopic state is reached.

Lastly, the “NeutronHP” packages were used to model the interaction and transport of any neutrons within the detector system. This data-driven model is based on measured neutron cross sections and has a nominal energy range of 0–10 MeV (ideally suited to this experiment). This is the same neutron physics package that is used in the SNO+ detector model.

### 4.2.3 Inelastic Scattering Process

During the initial stages of this experiment, it was observed that the simulation would produce a variety of unexpected  $\gamma$  rays in the case of the inelastic scattering process (i.e. the  $^{27}\text{Al}(n,n')$  reaction). Further evaluation, by probing directly into this process within the simulation, showed that these were inconsistent with what was expected through the decay of the excited  $^{27}\text{Al}$  nuclei.

Therefore, the inelastic scattering process was overridden to produce the excited  $^{27}\text{Al}$  nuclei directly (rather than the  $\gamma$  rays). The radioactive decay

process then handled the production of the  $\gamma$  rays as the nuclei de-excited. This change resulted in simulated energy spectra that were consistent with those from measurements in regards to peak location and width. A more detailed description of this simulation algorithm is found in Appendix A.

#### 4.2.4 Data Collection

Each emitted neutron from the AmBe source defines one “event” in the simulation. This includes the transport of the neutron, its interactions, and the production and transport of any secondary particles. To make an assessment of validity of the model used for neutrons, the observables of the laboratory experiment must be recreated. Here, that observable is the total energy deposited in the HPGe crystal by the  $\gamma$  rays that are produced in the interactions.

For each event, the simulated detector records this total deposited energy and stores it in a histogram. Each energy deposition has a Gaussian smear applied to it according to the measured resolution of the HPGe detector used for the previous neutron measurements. At the end of the simulation, this results in an energy spectrum that mimics a laboratory measurement using the simulated setup. This energy spectrum is directly comparable to the background subtracted energy spectra described previously in Section 4.1.6.

However, the simulation allows the user to have access to much more information. In this case, the number of neutrons produced is known and was used to determine an efficiency. This value can be used to convert from the rate of neutrons being produced by the source to the rate at which  $\gamma$  rays were detected by the HPGe detector for a given peak. The efficiency  $\epsilon$  is simply defined as:

$$\epsilon = \frac{N_{\text{peak}}}{N_{\text{simulated}}} \quad (4.2)$$

where  $N_{\text{simulated}}$  is the number of neutrons produced in the simulation and  $N_{\text{peak}}$  is the number of  $\gamma$  rays under a given peak in the simulated energy spectrum.

The efficiency will be used later to more easily assess the validity of the model.

## 4.3 Results

Performing the series of measurements shown in Figure 4.6, a number of different peaks were observed—each corresponding to a different neutron reaction. For each of the geometric configurations, an associated simulation was performed. The simulations corresponding to measurements of  $A_{\text{meas}}$  and  $A_{\text{bkgd}}$  were then subtracted in the same way as those laboratory measurements. The results from each of the different reactions observed will now be discussed.

### 4.3.1 $^{27}\text{Al}(\text{n},\text{n}')$ and $^{27}\text{Al}(\text{n},\text{p})$ Reactions

The  $^{27}\text{Al}(\text{n},\text{n}')$  reaction leaves a nucleus in one of its excited states, where it almost immediately decays back down to the ground state. For the first few states, this primarily occurs through the emission of a  $\gamma$  ray with energy equal to that state. Peaks corresponding to the first two energy levels of  $^{27}\text{Al}$  (energies of 844 and 1014 keV) were observed in all of the spectra for measurements that included the aluminum disk. Figure 4.7 shows these peaks for one geometric configuration along with the associated simulated spectrum. Additionally, a peak at 2212 keV (that corresponds to the third energy level of  $^{27}\text{Al}$ ) was observed, but at a much lower activity.

The negative peaks in the energy spectra are a result of the background subtraction. The backgrounds (from both radioactivity in the detector and shielding materials as well as the source) need to pass through the target material in the initial measurements. However, the measurements of the background spectra had these target materials removed in their configurations, resulting in less attenuation of any background  $\gamma$  rays. The subtraction of the relatively larger background peaks then results in these negative features. In the event that a negative peak overlaps one from a neutron reaction (seen for the 843.8 keV

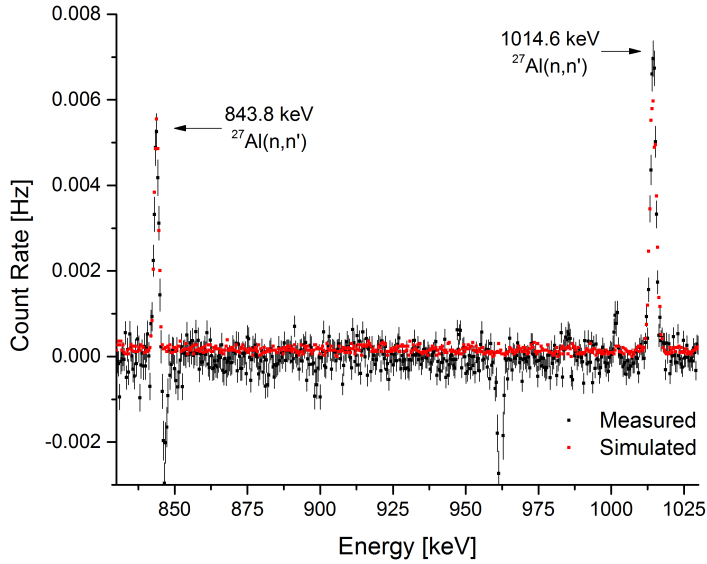


Figure 4.7: Background-subtracted measured and simulated energy spectra for the geometric configuration with the aluminum disk and four acrylic disks (configuration 5) [112].

$\gamma$  ray), that peak was not used for later activity determinations.

The  $^{27}\text{Al}(\text{n},\text{p})$  reaction produces a  $^{27}\text{Mg}$  atom.  $^{27}\text{Mg}$  will  $\beta^-$  decay back to  $^{27}\text{Al}$ . Some of the time, it will decay to an excited nuclear state of  $^{27}\text{Al}$ . In this case, the excited state of  $^{27}\text{Al}$  will decay to its ground state through the emission of the same  $\gamma$  rays seen in the  $^{27}\text{Al}(\text{n},\text{n}')$  reaction. Therefore, each of the 844 keV and 1014 keV peaks have some contribution from this reaction.

The simulation can be used to determine this contribution as this information is accessible while tracking the neutron and its interactions. From the simulation, the contribution of the  $^{27}\text{Al}(\text{n},\text{p})$  reaction is seen to be small (ranging from 2.0–3.0% over the different configurations) and is taken into account in subsequent analyses. Furthermore, the simulation can also be used to determine how long after neutron emission the interaction takes place. In the case of these reactions (which require a fast neutron), the time to interaction is  $< 10$  ns.

### 4.3.2 $^{27}\text{Al}(\text{n},\gamma)$ Reaction

The  $^{27}\text{Al}(\text{n},\gamma)$  reaction produces an  $^{28}\text{Al}$  isotope that  $\beta^-$  decays to  $^{28}\text{Si}$ . In this process, a 1778 keV  $\gamma$  ray is emitted. The corresponding peak was observed in some of the configurations that included the aluminum disk. Figure 4.8 shows this peak for all of the configurations that included the aluminum disk (configuration 1–5).

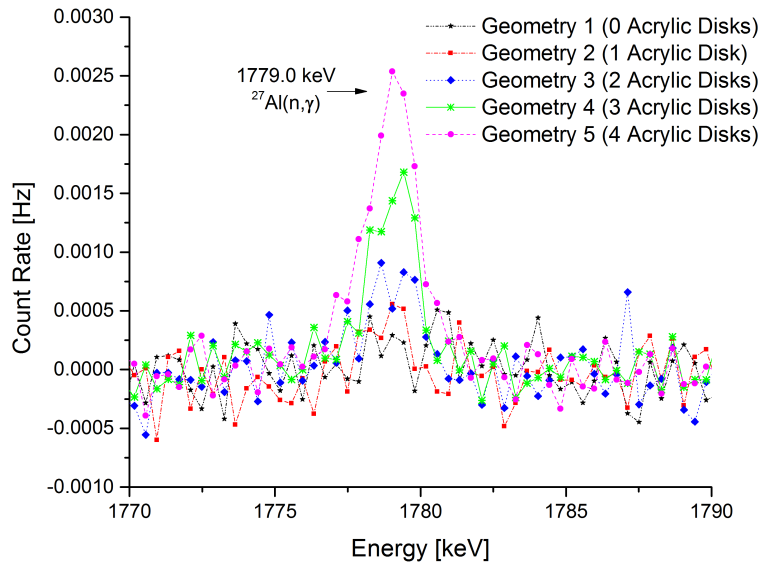


Figure 4.8: Background-subtracted measured energy spectra for the geometric configurations that included the aluminum disk (configurations 1–5). Error bars have been removed for clarity [112].

From Figure 4.2, this reaction is dominant for neutron energies below 1 MeV, down to 1 eV. However, from Figure 4.1, it is seen that the majority of the neutrons emitted from the AmBe source have energies  $> 1$  MeV. Therefore, to increase the rate of this reaction, the neutrons need to be moderated to lower energies. This effect is seen in Figure 4.8 as an increase in the peak size with the number of moderating acrylic disks.

### 4.3.3 $^1\text{H}(\text{n},\gamma)$ Reaction

The  $^1\text{H}(\text{n},\gamma)$  reaction, previously discussed in Section 3.4.3 as the reaction through which the neutron is observed in the SNO+ detector, spontaneously produces a deuteron and a 2224 keV  $\gamma$  ray. This gamma ray was observed in all of the configurations that included acrylic disks. Figure 4.9 shows the associated peak for the measurement of six acrylic disks (configuration 7).

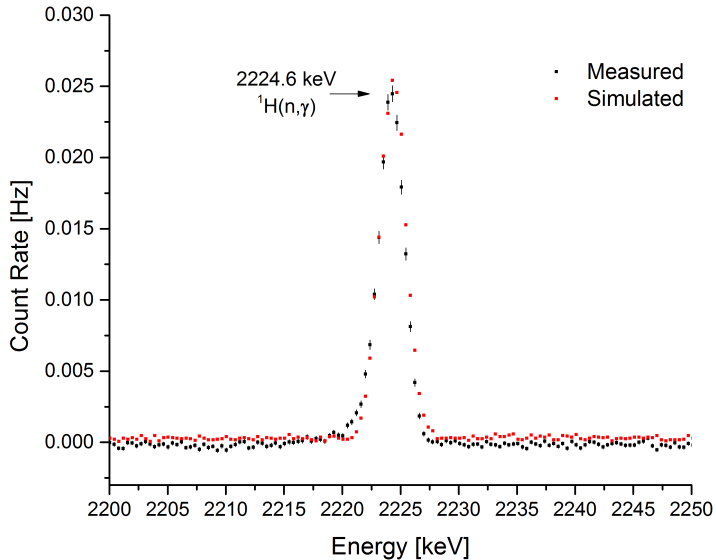


Figure 4.9: Background-subtracted measured and simulated energy spectra for the geometric configuration that included six acrylic disks (configuration 7) [112].

Again from Figure 4.2, this reaction is seen to be dominant for the lowest energy neutrons (below 1 eV). Therefore, the neutrons need to be heavily moderated before this reaction can occur. Looking at this moderation in the simulation, the  $\gamma$  ray emission occurs approximately 10–50  $\mu\text{s}$  after the neutron is emitted.

## 4.4 Model Comparison

In order to evaluate the validity of the model and to extend the scope of this experiment to serve as a calibration of this AmBe neutron source, the neutron activity of the source will be determined. A valid model should result in consistent neutron activity determinations across the many independent measurements in the different geometric configurations.

### 4.4.1 Neutron Activity Determination

The neutron activity  $A_n$  can be determined by applying the total efficiency  $\epsilon$  (determined by the simulation and defined in Section 4.2.4) to the measured activity of each peak corresponding to a neutron reaction  $A_{\text{reaction}}$ . This activity is determined as:

$$A_n = \frac{A_{\text{reaction}}}{\epsilon} \quad (4.3)$$

The neutron activity was determined separately for each of the three reactions and also for the associated applicable geometries. However, for each reaction there were several considerations that had to be taken in account.

### 4.4.2 Considerations and Corrections

#### $^{27}\text{Al}(n,n')$ Reaction

This reaction had a total of three peaks in each measured spectrum (844, 1014, and 2212 keV). In each spectrum, the 844 keV peak overlapped with a background peak of slightly higher energy (seen in Figure 4.7 as a negative peak at 846.8 keV, resulting from the  $^{56}\text{Fe}(n,n')$  reaction on the steel within the source and detector). Likewise the 2212 keV peak was overlapped with the 2224 keV peak from neutron  $^1\text{H}(n,\gamma)$  reaction (present in any configuration with acrylic disks). In general, the 2212 keV peak was more poorly resolved than the 844 keV and 1014 keV peaks. For these reasons, only the 1014 keV

peak was used to determine neutron activities for this reaction.

As the detection of the  $\gamma$  rays happens nearly simultaneously with the emission of the neutron, there is also some probability that the 4434 keV  $\gamma$  ray from the AmBe source will also deposit energy in the detector. This would result in a count that would previously contribute to the 1014 keV peak (and subsequently in the neutron activity determination) to no longer contribute, because two coincident  $\gamma$  rays present themselves as a single higher energy  $\gamma$  ray in the HPGe detector. Therefore a coincidence correction factor must be applied to the peak activity prior to determining the neutron activity.

The simulation was used to determine this correction factor. A further series of simulations were performed for all of the configurations with the aluminum disk (configurations 1–5) this time using 4434 keV  $\gamma$  rays as the initial particles. The result was a small correction that ranged from 3.2–6.1% of the total peak activity. Performing the simulations of the  $\gamma$  rays and the neutrons separately is not ideal, as it does not take into account possible correlations in the energy spectra. Namely, the energy spectrum of neutrons emitted with accompanying 4434 keV  $\gamma$  rays may differ from the total energy spectrum (of all neutrons). However, as the inelastic scattering cross section is relatively flat over the applicable range of energies, the impact this may have on the already small coincidence correction is expected to be negligible with regards to the calculated neutron activities.

### **$^{27}\text{Al}(\text{n},\gamma)$ Reaction**

Without sufficient neutron moderation, the  $^{27}\text{Al}(\text{n},\gamma)$  reaction would not occur at a high enough rate to observe a 1778 keV peak. This was the case for configurations 1 and 2, where very little to no acrylic was present. Without a peak, the activity of the neutron source was not possible to determine. It was therefore only calculated for configurations 3–5.

A coincidence correction factor was unnecessary in the case of this reaction.

This is because the emission of the 1778 keV  $\gamma$  ray occurs after the  $^{28}\text{Al}$  nucleus decays. A half-life of 2.2 minutes ensures that the detector will record this  $\gamma$  ray separately from the 4434 keV  $\gamma$  ray.

### $^1\text{H}(\text{n},\gamma)$ Reaction

The 2224 keV  $\gamma$  ray associated with this reaction was observed in all configurations with acrylic disks. However, in the case of the configurations that also included the aluminum disk (configurations 2–5), this peak overlapped with the 2212 keV peak from the  $^{27}\text{Al}(\text{n},\text{n}')$  reaction. Therefore, a neutron activity was not determined for those cases.

Similarly, a coincidence correction was also unnecessary. While the emission of the 2224 keV  $\gamma$  ray happens at the same time as the  $^1\text{H}(\text{n},\gamma)$  reaction, there is a 10–50  $\mu\text{s}$  time difference between neutron emission and the reaction. This results in any coincidence between the two being rejected as pile-up by the HPGe detector. This rejection, resulting in dead time, is corrected for by the data acquisition system when the live time of the measurement is determined.

### $\gamma$ ray Calibration

The measurement of neutron activity using this method relies on the accuracy in modeling the  $\gamma$  ray detection efficiency of the HPGe detector. This was evaluated by using radioactive calibration sources to obtain measured detection efficiencies. These efficiencies were then compared to those obtained from corresponding simulations of these sources.

The most precise calibration source used was a  $^{60}\text{Co}$  point source, with an activity known to 1.9%.  $^{60}\text{Co}$  simultaneously emits two  $\gamma$  rays with energies of 1173 keV and 1332 keV [115]. These  $\gamma$  rays may both be detected by the HPGe detector, in which case they sum to a single peak at 2505 keV. As these  $\gamma$  rays are in the same energy range of those from the measured neutron-induced reactions, this calibration is the most representative for the detection efficiency

comparison in this experiment.

A measurement and simulation were performed with the source placed at the centre of the detector's end cap. Further measurements were performed where the source was moved radially outwards from the centre in 1 cm increments. This allowed for a rough evaluation of the modeling of the internal components of the HPGe detector. The detection efficiencies determined from these measurements and simulations are compared in Figure 4.10.

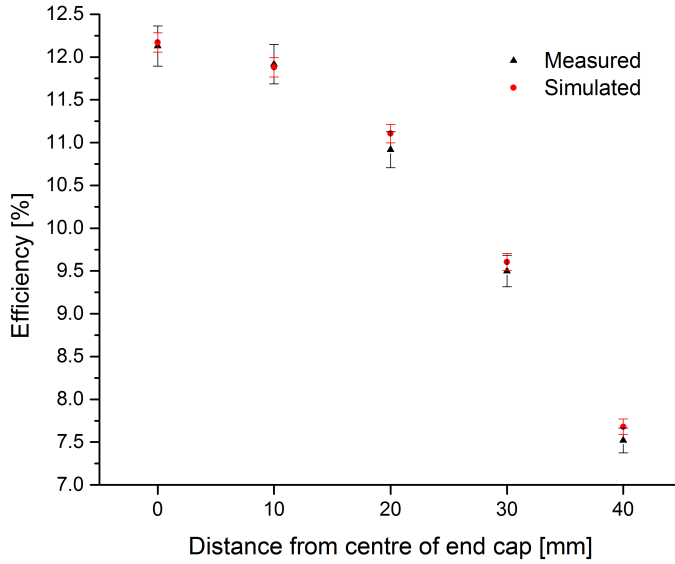


Figure 4.10: Measured and simulated  $^{60}\text{Co}$  detection efficiencies (combination of the 1173 keV, 1332 keV  $\gamma$  rays and their 2505 keV sum peak) as a function of the source distance from the centre of the HPGe end cap [112].

For all positions, the efficiencies showed good agreement between measurement and simulation. It was concluded that the simulation can model the  $\gamma$  ray detection for this HPGe detector to a precision of 1.9%. This is included as an uncertainty on the determined neutron activities.

### 4.4.3 Neutron Source Activity

The neutron activity of the AmBe source was determined for each applicable reaction for each of the seven configurations. These activities are shown together in Figure 4.11. A fit to this data yields a neutron source activity of  $307.4 \pm 5.0$  n/s.

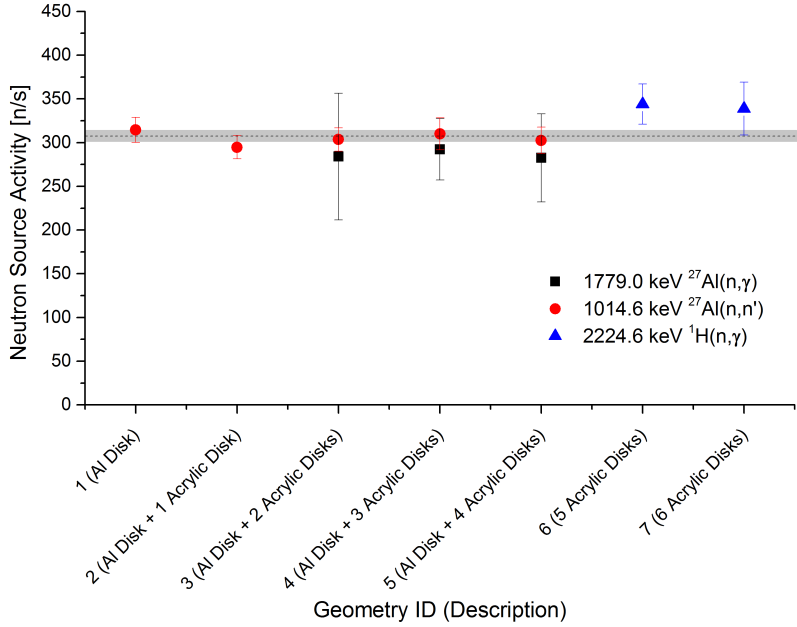


Figure 4.11: Neutron source activities determined for applicable reactions for each of the seven geometric configurations. The dashed line corresponds to a fit to the data and an activity of  $307.4 \pm 5.0$  n/s [112].

### Systematics

Two main systematics in this experiment were further evaluated. This experiment is entirely dependent on recreating the laboratory measurements in the simulation. Within the simulations, the different materials are all defined to be perfectly aligned. More specifically, the cylindrical detector, aluminum disk, acrylic disks, and AmBe source are all concentric.

In reality, the physical placement of these objects on top of the detector (within the copper and lead shielding) may not be as precise, where sub-mm

precision would be preferred. This results from these targets needing to be placed one at a time from the top. This is especially problematic in the case of placing the aluminum disk (and subsequent acrylic disks) as the aluminum disk entirely obscures the view of the HPGe detector.

In order to estimate the uncertainty associated with this, a further set of simulations were made. An uncertainty of 5 mm in the position of the disks relative to the central axis of the HPGe was assumed (placement of the acrylic disks and neutron source was more precise due to the transparency of the acrylic and similar radii of these disks).

The other systematic in this experiment originates from the knowledge of the neutron energy spectrum of the AmBe source. To evaluate this, another series of simulations were performed. In these simulations, the relative intensity of different regions in the spectrum were shifted by up to 10%.

The results of this evaluation are summarized in Table 4.1. The dominant systematic results from the relative placement of the disks and neutron source. While the effect of the neutron energy spectrum is non-negligible, it is much smaller in comparison. These systematic uncertainties were included with the statistical uncertainties in Figure 4.11.

Systematic	Effect on Neutron Activity
Source/target positioning $^{27}\text{Al}(\text{n},\gamma)$	5.3–19.1%
Source/target positioning $^1\text{H}(\text{n},\gamma)$	5.9–6.2%
Source/target positioning $^{27}\text{Al}(\text{n},\text{n}')$	1.8–3.3%
Neutron spectrum $^{27}\text{Al}(\text{n},\gamma)$	0.8–3.0%
Neutron spectrum $^1\text{H}(\text{n},\gamma)$	0.8–2.9%
Neutron spectrum $^{27}\text{Al}(\text{n},\text{n}')$	0.1–3.2%

Table 4.1: Effects of the different systematics evaluated. The range is shown over the applicable geometric configurations for each reaction [112].

## Alternative Calculation

Alternatively, the neutron activity can be calculated directly from the measurement of the 4434 keV  $\gamma$  ray emitted by the neutron source. To do this, one

further measurement was taken with the AmBe source placed directly on the detector. The efficiency of detecting this  $\gamma$  ray with the HPGe detector was then determined by performing a simulation of this measurement. Figure 4.12 shows the energy spectra obtained by this measurement and simulation.

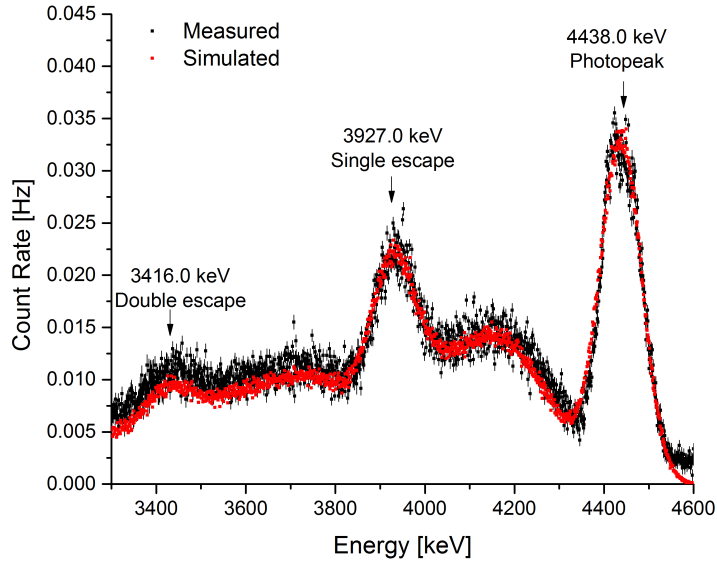


Figure 4.12: Measured and simulated energy spectra showing the 4438 keV  $\gamma$  ray that is emitted by the AmBe neutron source. [112].

To perform this measurement of the high energy 4434 keV  $\gamma$  ray, an attenuator needed to be placed between the HPGe detector and the data acquisition system. Without this addition, the electronic signal would be outside of the range of the system. However, the reduction in the electronic signal results in the poorer resolution seen in Figure 4.12 relative to the other measured  $\gamma$  rays (at lower energies).

This efficiency is used to determine the number of 4438 keV  $\gamma$  rays emitted by the source. Applying the ratio of these  $\gamma$  rays to emitted neutrons ( $0.575 \pm 0.028$ ), the activity of the neutron source can again be determined [107]. This calculation yields a neutron activity of  $305 \pm 16$  n/s. This is consistent with the value previously determined from the neutron reactions.

As this activity is determined independently of any neutron interactions, this lends further support to the correct modeling of neutrons in the simulation.

## 4.5 Inelastic Scattering Evaluation

As the inelastic scattering process in the model was the only one found to possibly pose a problem in regards to modeling the SNO+ detector, it was further evaluated. First, the inelastic scattering cross sections of the different elements that make up the SNO+ detector were explored. During the tellurium phase, the active volume will be primarily composed of hydrogen, carbon, and tellurium. There will also be some oxygen and nitrogen in the additional compounds (1,4-Butanediol and Dodecylamine [116]) that are needed in order to add tellurium into the liquid scintillator and maintain its chemical stability.

The inelastic scattering process has a threshold neutron energy (which depends on the structure of the nuclear energy levels of a given isotope). If the elastic scattering process is dominant compared to the inelastic scattering process, the neutron would be first moderated to lower energies. At these lower energies, the inelastic process will not be possible and will no longer occur. At the lowest energies, the neutron will capture (through an  $(n,\gamma)$  reaction).

### 4.5.1 Cross Sections

The inelastic and elastic scattering cross sections of these five main elements are shown in Figure 4.13. The cross sections are scaled by the natural abundance of each isotope. This provides a better impression as to the reactions that will predominantly take place within the SNO+ detector. It should be noted that for the case of neutrons produced via IBD, the energies range up to around 100 keV. In the case of calibrations taken using an AmBe source, the energies of the neutrons range up to 11 MeV.

Based on these cross sections, the inelastic process will be negligible for

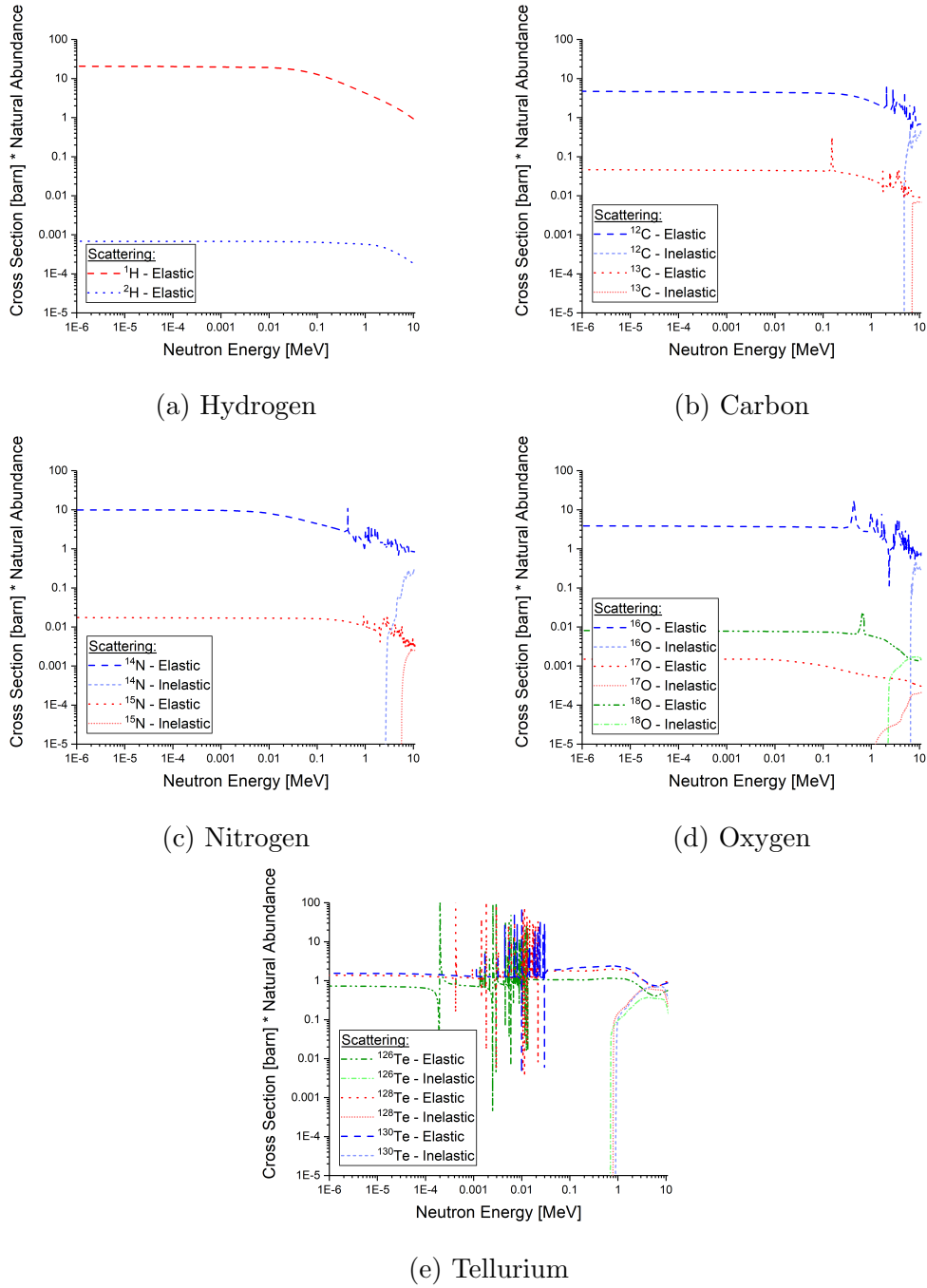


Figure 4.13: Neutron elastic and inelastic scattering cross sections for the main elements that make up the SNO+ detector. The cross sections are scaled by the natural abundance to better represent the contribution of each isotope. Data from [110].

the cases of hydrogen, carbon, nitrogen, and oxygen. The sole process where it may have any noticeable (albeit small) effect is inelastic scattering off tellurium. Based on the threshold energies of around 1 MeV, it would only occur during calibrations with the AmBe source. Therefore, only the inelastic scattering process off tellurium was further investigated.

#### 4.5.2 Measurements

Measurements were performed by placing a 3.4 kg metallic tellurium ingot on the HPGe detector. Due to the brittle nature of metallic tellurium, the ingot was enclosed within a plastic bag to maintain the cleanliness of the detector system. The AmBe source was then placed directly on top of the tellurium.

The measurement was again performed over a period of approximately 24 hours. Similarly, a background measurement, which included the source being placed on top of a hollow spacer of equal height to the ingot, was made. Figure 4.14 shows the energy spectra obtained from these measurements. The energy range in these spectra shows all of the peaks that were present after background subtraction. A further measurement of the tellurium ingot alone showed that there was no contribution from ambient neutrons.

Previously, the baseline that surrounds each observed peak was relatively flat, resulting in a straightforward linear fit and subtraction. The baseline seen here in Figure 4.14 is much more complicated. This adds to the difficulty of making an exact comparison to the associated simulations. There are also peaks that are more prominent in the spectrum without the tellurium (for example, the 846.8 keV peak from  $^{56}\text{Fe}$ ). Here these originate from radioactivity/interactions in the source itself, where the resulting  $\gamma$  rays are less attenuated without the placement of the tellurium ingot between the source and the detector. They also help illustrate the cause of the negative peaks in some of the previous energy spectra.

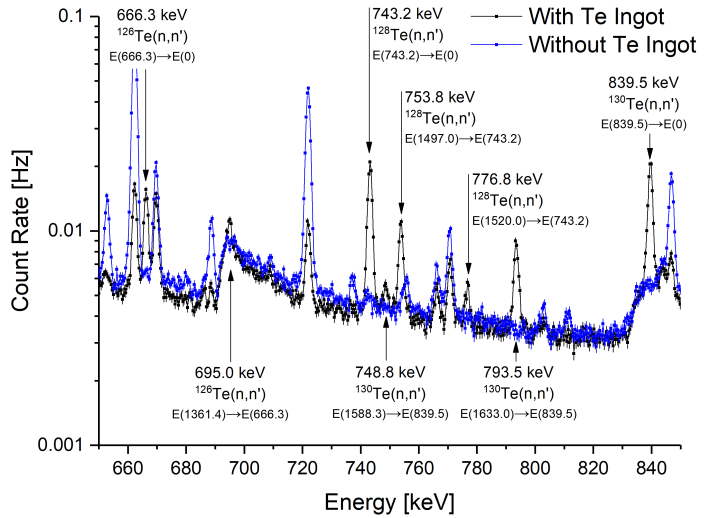


Figure 4.14: Measurement of the tellurium ingot with and without the neutron source. All of the peaks due to neutron inelastic scattering are labeled with their corresponding isotopes and nuclear energy level transitions.

### 4.5.3 Simulation

The simulation was performed in the same manner as before. The exact dimensions of the ingot were difficult to precisely model as the ingot itself was obscured by the plastic bag and small visible pieces of the ingot had broken off. However, the mass in the simulation was identical to that of the physical ingot.

Two simulations were performed using the same modified inelastic process (described previously in Section 4.2.3). This included a simulation of the source and ingot followed by a second simulation with the source placed on top of the hollow spacer. Two more simulations were performed, using the default inelastic scattering process (the same that is used in the SNO+ detector model).

### 4.5.4 Results and Discussion

Each energy spectrum for the ingot had the corresponding spacer energy spectrum subtracted. This was first done for the measured spectra seen in Figure

4.14, followed by the two pairs of simulations. A comparison of each simulated background-subtracted energy spectrum to the measurement is shown in Figure 4.15.

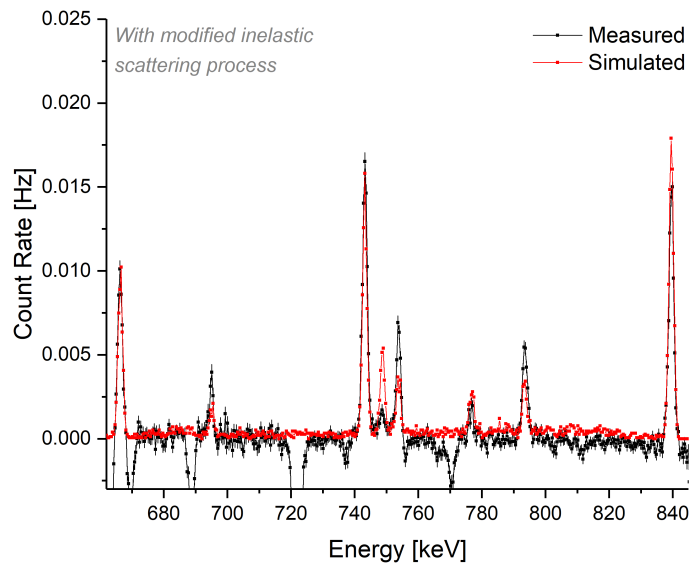
The challenge presented by the complicated baseline of these measurements from Figure 4.14 is seen here as a large amount of negative peaks (due to the decrease in attenuation between the two measured spectra). This further complicates the comparison when these features are in close proximity to peaks from the  $\text{Te}(n,n')$  reaction.

However, based on Figure 4.15, it is clear that the neutron inelastic scattering reaction is taking place and is able to be reproduced by the simulations. In addition, the physics process that models this reaction in the SNO+ simulation has no major difference when compared to the modified one that was used in the experiment. While a modification to this process was needed to properly model neutron interactions on aluminum, it does not need to be incorporated into the SNO+ model.

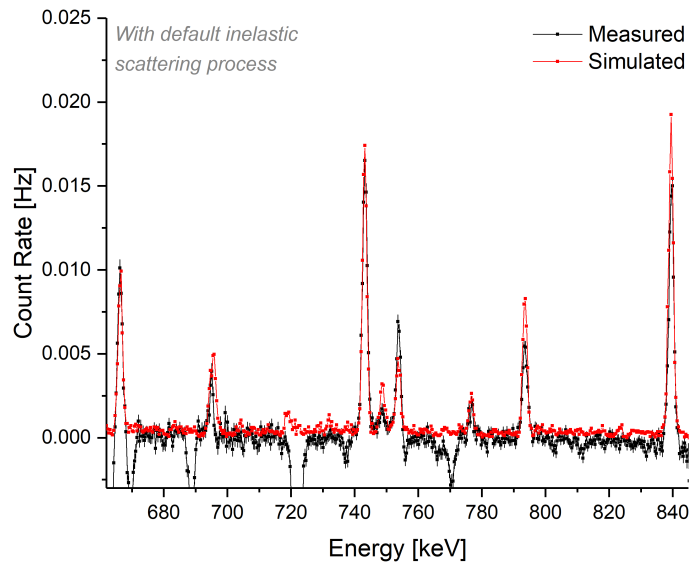
### Additional Considerations

One additional benefit of this measurement is a rough gauge on any cosmogenic activation of tellurium. Cosmogenic protons and neutrons that interact with tellurium may produce unstable isotopes [117]. Certain long-lived isotopes can potentially pose a problem to the SNO+ detector during its operation if they have high-energy decay modes [118]. For this reason, the tellurium to be added to the SNO+ detector is currently being stored underground to allow such isotopes to decay prior to use. During the laboratory measurements with the tellurium ingot, no other peaks were observed in the background-subtracted spectrum from Figure 4.14, other than those from  $\text{Te}(n,n')$  reactions. Therefore, there was no clear problem encountered in regards to the cosmogenic neutron activation of tellurium.

One further consideration to be made is the potential impact of thermal



(a) The inelastic scattering process was modified to produce excited Te ions directly.



(b) The inelastic scattering process was unchanged.

Figure 4.15: Measured and simulated energy spectra for neutron reactions induced on tellurium. All of the different peaks are the result of neutron inelastic scattering off the primary isotopes of tellurium.

neutron capture ( $(n,\gamma)$  reactions) that may take place during the tellurium phase of the SNO+ experiment. For slow neutrons ( $< 1$  eV), the capture cross section for these reactions for the main isotopes of tellurium ( $^{126}\text{Te}$ ,  $^{128}\text{Te}$ , and  $^{130}\text{Te}$ ) is roughly the same as for hydrogen [119]. If a neutron were to capture on a tellurium isotope rather than hydrogen, it would no longer create the characteristic 2.2 MeV  $\gamma$  ray that enables the distinction of an antineutrino signal. Instead, longer lived ( $O(10 \text{ min})$ – $O(10 \text{ hrs})$ ) unstable tellurium isotopes would produce  $e^-$  and  $\gamma$  rays at a variety of energies [120–122].

The relative reaction rate  $R$  can be determined from the cross sections  $\sigma$  and the number density  $\rho$  by:

$$\frac{R_{\text{H}}}{R_{\text{Te}}} = \frac{\sigma_{\text{H}} \rho_{\text{H}}}{\sum_A \sigma_{A\text{Te}} \rho_{A\text{Te}}} \quad (4.4)$$

During the tellurium phase, the SNO+ liquid scintillator will be 0.5% tellurium by mass. Performing this calculation and summing over the different tellurium isotopes, the rate of capture on hydrogen will be approximately 5000 times larger than on tellurium. This will impact less than one neutron from IBD over the lifetime of the SNO+ experiment and therefore, the impact of tellurium on the reactor antineutrino signal is negligible in this regard.

## 4.6 Conclusions

This experiment consisted of a multitude of measurements of an AmBe neutron source made using a HPGe detector. These measurements showed that a variety of neutron reactions took place. These included  $^1\text{H}(n,\gamma)$ ,  $^{27}\text{Al}(n,\gamma)$ ,  $\text{Te}(n,n')$ , and  $^{27}\text{Al}(n,n')$ . They also demonstrated the effect of acrylic as a neutron moderator (through the neutron elastic scattering reaction). These reactions probed an effective neutron energy range of 10 MeV down to below 1 eV.

In addition, a Geant4 model for this specific HPGe detector was developed. The simulation of all of the measurements performed consistently showed good agreement with the corresponding measurements. This allowed for an activity calibration of the neutron source itself. The previously unknown activity was determined to be  $307.4 \pm 5.0$  n/s. Lastly, based on the results of this experiment, Geant4 was shown to be an appropriate software package to model the neutron reactions that will take place in the SNO+ detector.

# Chapter 5

## Simulations and the Antineutrino Search Algorithm

To design an analysis that will enable a comprehensive search for any antineutrinos that have interacted in the SNO+ detector, their signal must be well understood. More specifically, how the individual signals (from both the  $e^+$  and neutron) appear in the detector must be determined. This is typically done through a combination of Monte Carlo simulations and calibrations.

The signal from the neutron will be best determined by performing calibrations (discussed in Section 6.1); however, determining the  $e^+$  signal requires the use of simulations. As the  $e^+$  span a wide energy range, that is specific to each individual detector (as oscillations will differ between detectors), there is no calibration source that exactly replicates their signal.

To best identify the antineutrino signal, an understanding of the backgrounds in the detector is also required. An optimal search would maximize the acceptance of the antineutrino signal while simultaneously maximizing the rejection of backgrounds. This is also done through the development of a Monte Carlo simulation. The following sections will detail how the signals from antineutrinos are simulated for the SNO+ detector and establish how they will appear. From this information, a search algorithm was designed to specifically

extract this signal from the detector data. Lastly, a Monte Carlo simulation was developed that replicates the measured detector backgrounds.

## 5.1 SNO+ Monte Carlo Simulation

Over many years, the SNO+ collaboration has developed a framework that includes a Monte Carlo simulation of the detector and a platform on which to perform analyses of the data. This framework, called the Reactor Analysis Tool (RAT), bases its Monte Carlo simulations on the Geant4 Toolkit and incorporates ROOT libraries [123] for data handling and analysis.

A main advantage is that any data (whether collected by the detector or simulated) is stored in a universal file structure. RAT then allows for analyses (for example, event reconstruction) to be performed on the data and also be stored in the same format along with it. The outcome is that analysis algorithms (such as the one that searches for antineutrinos) can be applied identically to the detector data, calibration data, and Monte Carlo simulations.

### 5.1.1 Antineutrino Simulation

#### Initial Particles

When performing a simulation, the number of particles to simulate is specified. For a reactor-produced antineutrino, the important initial information is the distance that it traveled and its energy. These are determined using the “Reactor Generator” component of RAT [124]. At the beginning of every simulation, this performs the calculation described in Section 3.4.2, where it determines the contribution of every nuclear power reactor to the antineutrino energy spectrum. For each antineutrino, it will then sample from this energy distribution and correspondingly sample and designate a reactor.

## Particle Production

With the initial antineutrino chosen, the IBD reaction is simulated. This produces both a  $e^+$  and a neutron within the simulation. These are produced at the same location and time. Locations are chosen uniformly within the central water volume of the detector. As these particles are propagated within the simulation, many different physical processes are modeled. These include the scattering, ionization, and annihilation of the  $e^+$  along with the scattering and capture of the neutron. Any subsequent particles ( $e^-$ ,  $e^+$ , and  $\gamma$  rays) produced during the scatter or neutron capture are also modeled.

A full optical model of the detector is incorporated into the simulation. Firstly, the production of Cherenkov photons is modeled. These photons are propagated through the various optical media (water, acrylic, PMT glass) where they may be refracted, reflected, or absorbed within/at the boundaries of these media. The photons are tracked until they are lost to absorption in a medium/at an interface. If this occurs at the photocathode of a PMT, a simulated pulse may be produced.

## Simulated Events

If enough PMTs produce simulated pulses (for a simulated  $e^+$  or neutron), the detector will trigger. The same trigger logic is applied to the simulated PMT pulses as for the data collected by the detector. This simulated event is then stored in the same format as detector data. This allows for the same reconstruction and analysis algorithms to be run on simulated data as on detector data.

The simulated events will have much more information stored. This includes everything regarding the initial particles (like energy, direction, position) along with the trajectories of those particles. Additionally, all of the physical processes that occurred are stored. The same information is stored for any primary or secondary particles produced.

## Simulated Runs

To best model the operation of the detector, RAT has a feature where a specific run can be exactly simulated. With a user-specified run number, it takes detector state information from the database for that run. A simulation is then performed with a total length corresponding to that of the run. The exact operating conditions at the time are simulated (these include the threshold settings on each individual PMT and the overall detector trigger settings). When performing simulations of an antineutrino signal, a low rate ( $< 1$  Hz) for IBD events is used. This ensures that enough events are simulated, while keeping the probability negligible that two separate IBD events will be coincident with one another.

These simulations assume that there are no neutrino oscillations. Oscillations are applied separately to the these simulated runs using the “Reactor Oscillations Processor” [125]. The origin (reactor core) and energy of each neutrino is known. The survival probability (Equation 2.7) is then calculated for each neutrino. A random number between 0 and 1 is generated and if it is greater than the survival probability, the neutrino event is removed from the simulated data set. This results in a data set corresponding to the expected measurement of antineutrinos following the appropriate energy spectrum. This method has the advantage that separate data sets can be generated (using different oscillation parameters) without the need to resimulate. For these simulations, the oscillation parameters were taken from the Particle Data Group [41](the latest released values in 2018 [46] do not differ for the relevant oscillation parameters).

At the time, data collected by the SNO+ detector also had a blinding scheme applied to it with regards to the invisible nucleon decay analysis [96]. This scheme had all events with  $n_{\text{Hit}} \geq 39$  removed from the data set. The same scheme can be applied to the simulated antineutrino runs. This chapter shows the simulations before blinding is applied to fully illustrate the antineu-

trino signal. However, for the optimizations in Chapter 6 and the efficiency determinations in Chapter 7, the blinded simulations are instead used to properly correspond to the data analysis in Chapter 8. The impact of this blindness is quantified later in Section 7.2.

## 5.2 Antineutrino Event Selection

### 5.2.1 Time Coincidence

By producing this high statistics set of antineutrino simulations, one can determine what IBD will look like within the SNO+ detector. The important characteristic is the coincident signal. This manifests itself as two events that both triggered the detector within a short period of time. From these simulations, the exact time between the emission of the  $e^+$  and the emission of the 2.2 MeV  $\gamma$  ray (from neutron capture) is shown in Figure 5.1.

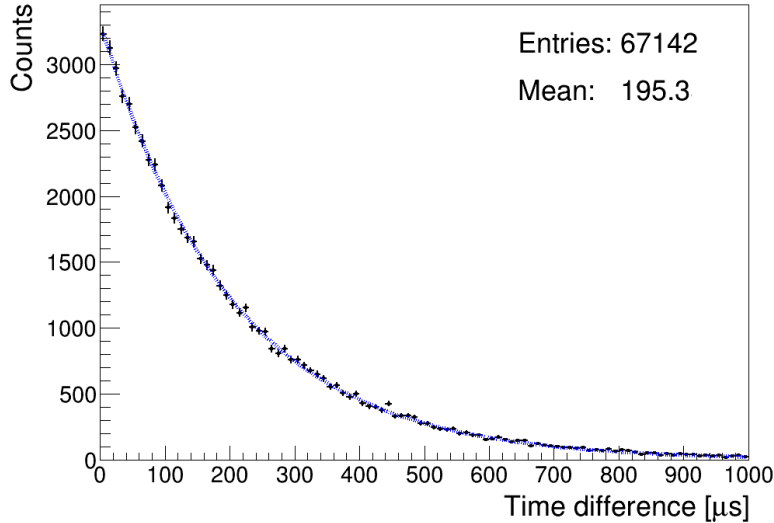


Figure 5.1: Time difference between the emission of the  $e^+$  and the emission of the 2.2 MeV  $\gamma$  ray from an IBD event in the SNO+ simulation. The blue dashed line represents an exponential decay fit to the data.

This shows that the majority of the neutrons (> 90 %) will capture and

trigger the detector within a period of  $500 \mu\text{s}$ . This provides a starting point for the time scale on which to base the later search. This time difference of events  $N(\Delta t)$  is expected to follow an exponential distribution:

$$N(\Delta t) \propto e^{-\frac{\Delta t}{\tau}} \quad (5.1)$$

Performing a fit of this function to the distribution in Figure 5.1 gives a time constant  $\tau$  of  $202.02 \pm 0.87 \mu\text{s}$ . This quantity is referred to as the mean neutron lifetime and is specific to the medium that the neutron travels through. This value is comparable to other such measurements [92,93]. A more thorough comparison is performed in Section 7.1.3 after more determinations are made.

### 5.2.2 Position Difference

After the reconstruction algorithms have been applied to the simulated data, each triggered event will have a reconstructed position  $(x, y, z)$  (with the exception of failed reconstructions). The coincident event pairs are separated by a distance  $d$ :

$$d = \sqrt{(x_2 - x_1)^2 + (y_2 - y_1)^2 + (z_2 - z_1)^2} \quad (5.2)$$

The exact position of both the  $e^+$  and neutron as it is emitted and the neutron as it is captured are known within the simulation. This allows for the exact distance to be determined for each event pair. This is represented in Figure 5.2, which shows that the neutron is much more likely to travel a short distance before capturing, rather than traversing the detector, and suggests that this spatial correlation may be used in a search. Performing this same distance determination now using the reconstructed positions for each event yields the distribution in Figure 5.3.

Using the reconstructed positions of each event yields a much broader distribution. This is due to the spatial resolution of the reconstruction algorithms. With the low amount of light, it is difficult to precisely determine the position.

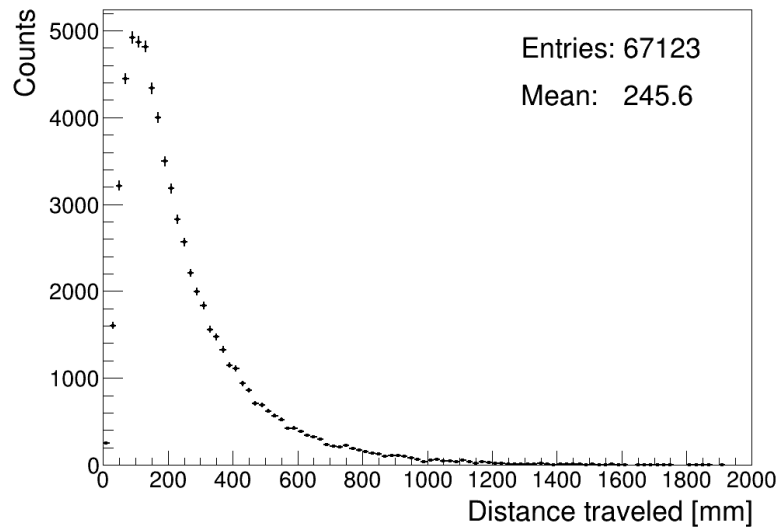


Figure 5.2: Distance that the neutron from IBD travels from the point of emission to the point of capture in the SNO+ simulation.

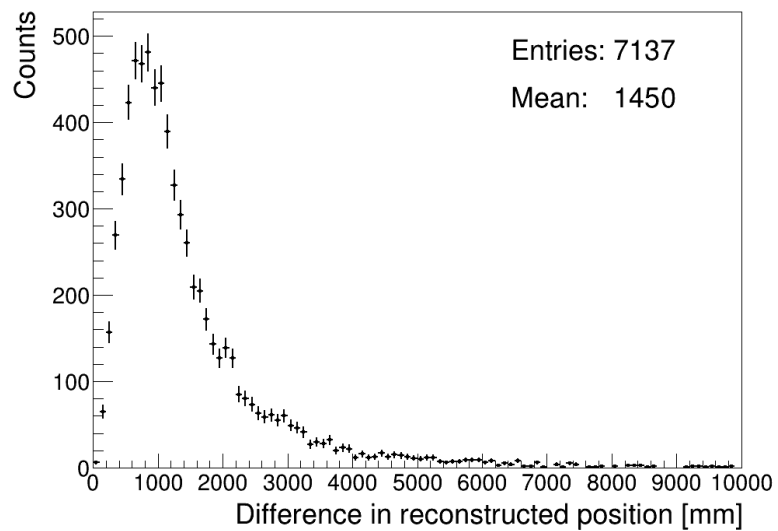


Figure 5.3: Reconstructed distance between the  $e^+$  event and the neutron event from IBD in the SNO+ simulation.

The spatial resolution can be estimated by comparing the known position of the event in the simulation to the reconstructed position. These comparisons, performed separately for the  $e^+$  and neutron, are shown in Figure 5.4. As the reconstructed position difference is a measurable quantity, it illustrates that by looking for events that reconstruct within 1–2 m of each other, the antineutrino signal may be distinguishable.

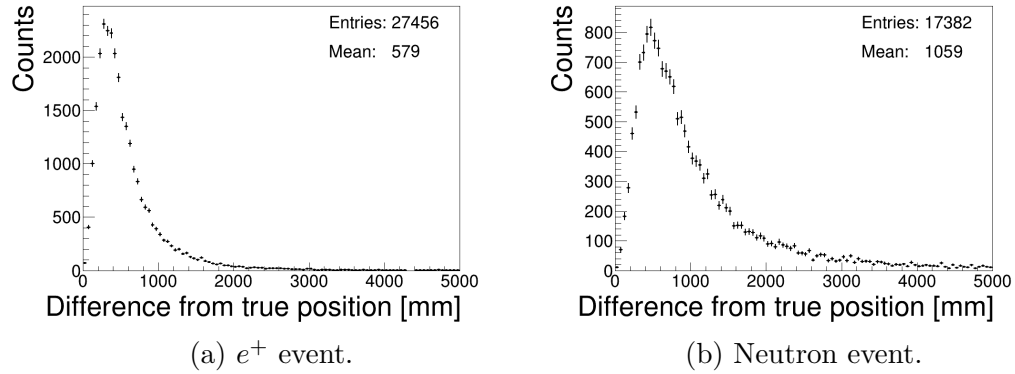


Figure 5.4: Difference between the reconstructed position and the true position for each event in the SNO+ IBD simulation.

### 5.2.3 Number of PMTs

One main characteristic of each event includes the number of PMTs that detected photons (referred to on the SNO+ experiment as “nHit”). This number is approximately proportional to the energy of the particles that produced the light. Each event pair will have two nHit values associated with it. Figure 5.5 shows the 2-dimensional distribution of these values for the simulated signal.

While the neutrons produce little light and consequently have low nHit values, the  $e^+$  produce much more light. The high nHit values of the  $e^+$  events (higher than most backgrounds) can potentially be used to search for antineutrinos in detector data.

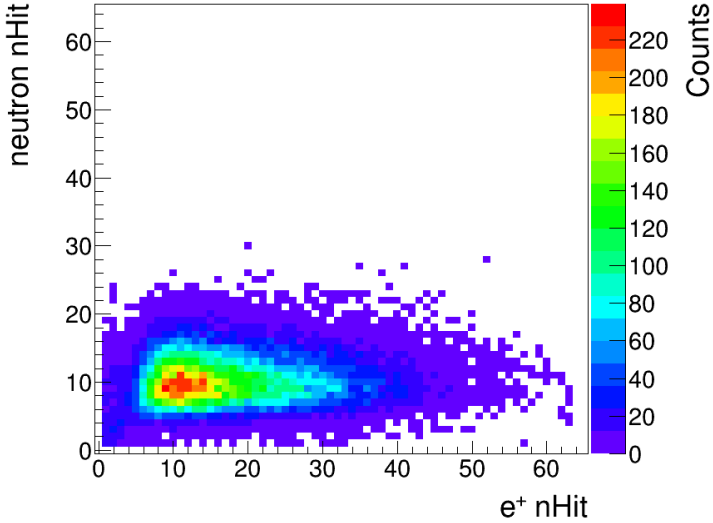


Figure 5.5: nHit distribution of both the  $e^+$  and neutron events from IBD in the SNO+ simulation.

### 5.3 Search Algorithm

With an expectation of how antineutrinos will look like in the SNO+ detector, an analysis algorithm was designed to search for this signal.

Triggered events, whether produced by the simulation or collected by the detector, are stored sequentially in time. Each event is uniquely identified by its GTID (global trigger ID, an increasing integer) and the run number. All other information, including the results of the reconstruction algorithms, are stored along with these identifiers. Therefore, a search for coincident pairs of events first requires looking at each individual event in the data set.

#### 5.3.1 Algorithm Overview

As the data sets are very large (upwards of  $10^9$  events in detector data stored in several terabytes of data files), the search algorithm uses a two-pass approach.

## First Pass

The first pass over the data set finds and extracts coincidences. It is designed with criteria in mind to keep nearly all event pairs from antineutrinos. At its core, it is structured as a set of two nested loops:

For each event, index  $i$  (starting from the beginning and going forward in time):

If event  $i$  has a reconstructed position and is within the central water volume ( $r < 6000$  mm):

For each event, index  $j$  (starting from  $i+1$  and going forward in time):

If event  $j$  is within 1000  $\mu\text{s}$  of event  $i$  and also within the central water volume ( $r < 6000$  mm):

Store all information regarding event pair  $i$  and  $j$  as a single entry.

Loop until the next event  $j$  is  $> 1000 \mu\text{s}$  later in time than event  $i$ .

Loop until the end of the data file.

In case multiple events occur within the 1000  $\mu\text{s}$  time window, each possible coincidence is tested and potentially stored. This ensures that the extracted subset of event pairs consists of all possible coincidences.

This pass of the search algorithm produces a list of coincident event pairs in the data. The associated information for each individual event in the pair is stored alongside each entry. The goal of this first pass is to greatly reduce the size of the data files. It is designed to be run only once over any data set.

## Second Pass

With a comprehensive list of all possible coincidences in the data set, the second pass of the algorithm applies further criteria to identify possible antineutrino signals. This involves the application of cuts on the fiducial volume, time difference, position difference, and nHit.

This pass is applied as a single loop over the coincidence pairs produced by the first pass:

For each event pair:

If the pair has a time difference of  $\Delta t < \Delta t_{\max}$ :

If each event is within a fiducial volume  $r < r_{\text{FV}}$ :

If each event is within a specific nHit range

$[nHit_{\min}, nHit_{\max}]$ :

If the pair has a position difference of  $< d$ :

The event pair is considered an ‘‘antineutrino candidate’’.

Loop until the end of the event pair data file.

The fiducial volume cut  $r_{\text{FV}}$  and the nHit cut  $[nHit_{\min}, nHit_{\max}]$  can be specified such that they differ for the first event ( $e^+$ ) and the second event (neutron). The total number of event pairs that pass all of the above conditions are the number of events in the dataset that appear as antineutrinos.

## 5.4 Background Monte Carlo

To design a final set of selection criteria that will maximize the acceptance of signal and rejection of background, an accurate model of the background in the detector is needed. Traditionally, this would be performed by modeling each individual source of background within the detector using Monte Carlo simulations. The resulting distributions from those simulations can then be compared

against those from the antineutrino simulations to determine an optimized set of selection criteria.

### 5.4.1 Drawbacks and Alternative

For the case of the coincident signal from antineutrinos, a Monte Carlo simulation of the background requires one to simulate all possible sources of background at the same time (rather than simulating each source individually). This is required as two different independent sources of background can be coincident (referred to as an “accidental coincidence”) and produce a pair of events that appear as an antineutrino. This method presents two main problems:

- Current estimates of the radioactive backgrounds that occur within the SNO+ detector have a total rate of 10,000’s of decays per second [126]. Simulating enough live time to obtain sufficient statistics for the background model’s distributions is unfeasible (from a computational time standpoint).
- Some radioactive background rates have been quantified through assays, though many are still not well understood [127]. As estimates change, it becomes even more impractical to repeat the full simulation.

Given the coincident nature of the antineutrino signal, an alternative approach can be taken. First, one principal hypothesis must be made: that all of the backgrounds to the antineutrino signal are from accidentals. Specifically, two uncorrelated background events that trigger the detector within a short time are the background to antineutrinos. At this time, this is only a hypothesis that will be tested and not a definitive statement.

### 5.4.2 Toy Monte Carlo Approach

The data already collected by the detector provides a measured set of distributions for events within the SNO+ detector. More specifically, the distribution

of the time between each triggered event, where the events reconstruct, and the nHit of each event are known. Using the assumption that the backgrounds to antineutrinos are accidental pairs of these such events, a “fake” set of coincidences was constructed from this information.

Individual events were created with a sampled position and nHit based on the events that triggered the detector using one of the physics-based triggers (i.e. not a calibration trigger). They were then randomly put in coincidence based on the time differences seen in detector data. Sampling to generate event pairs in this way defines a toy Monte Carlo approach to producing the background simulation.

### 5.4.3 Event Generation

#### Individual Event Data

The foundation of the toy Monte Carlo are the data from which the event pairs are sampled. These data were taken in the period from September 5, 2017 to September 8, 2017. Only runs that passed all data quality cuts (labeled as “golden” runs) are used. The exact subset of runs used is detailed in Appendix C. This subset of runs corresponds to 2.6 live days of data taking. Data cleaning cuts are applied using the “analysis mask”, detailed in Appendix B. This subset is a small fraction of the total data collected by the detector (69.7 live days). Choosing a smaller subset of data made it computationally possibly to rerun the search algorithm many times (necessary when looking for optimal cut parameters, Chapter 6).

While many events trigger the detector, many will fail to pass data cleaning and/or fail to reconstruct. Only events that pass data cleaning and successfully reconstruct are considered as possible contributors to a background that may look like the antineutrino signal (those that fail are removed from the data set). The distributions of these individual events from the detector-collected data

are shown in Figure 5.6 and form the basis of the toy Monte Carlo simulation. These include: the separation of events in time; radii at which they reconstruct; and their nHit.

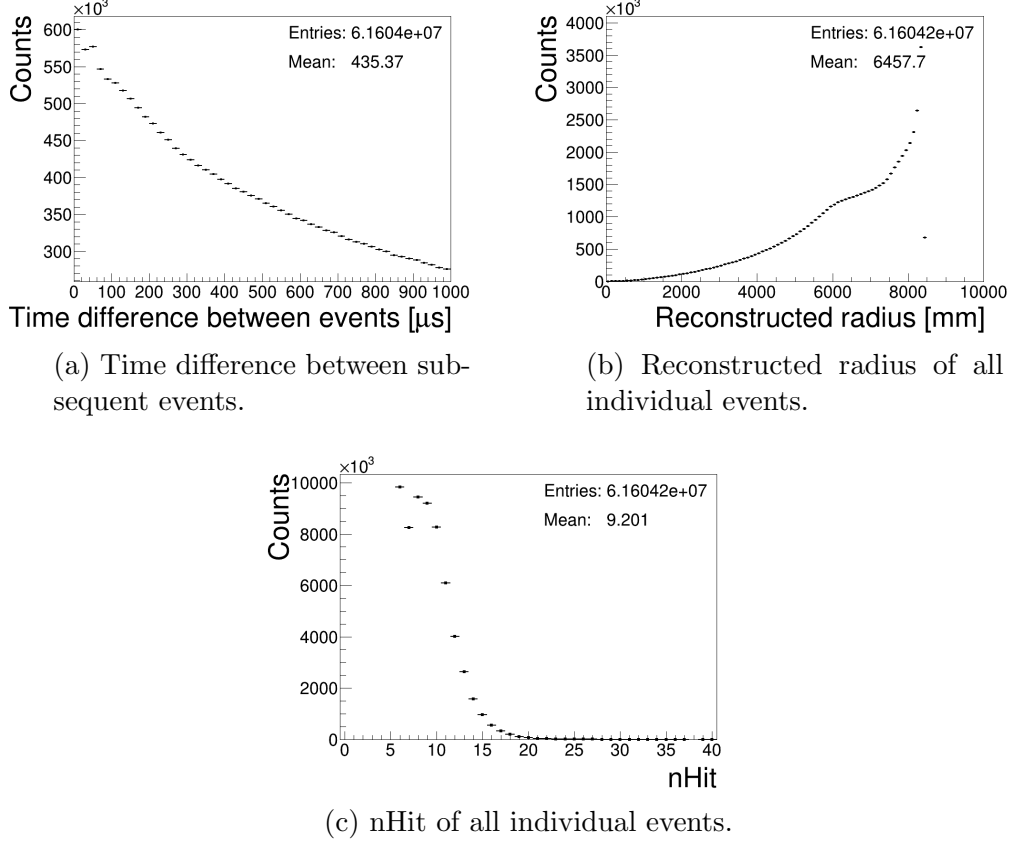


Figure 5.6: Distributions from the data collected by the SNO+ detector over 2.6 live days. Only events that pass data cleaning and successfully reconstruct contribute to these distributions.

## Correlations

Prior to sampling from these distributions to generate fake event pairs, the possible correlations between these variables need to be evaluated. For the three different sampling variables, there are three possible pairs of correlations. To evaluate these, the detector data was reanalyzed plotting each pair of variables in two dimensions. Figure 5.7 shows these three 2-dimensional histograms. For

each figure, rather than displaying counts, each y-axis bin has been normalized individually to better see any structure.

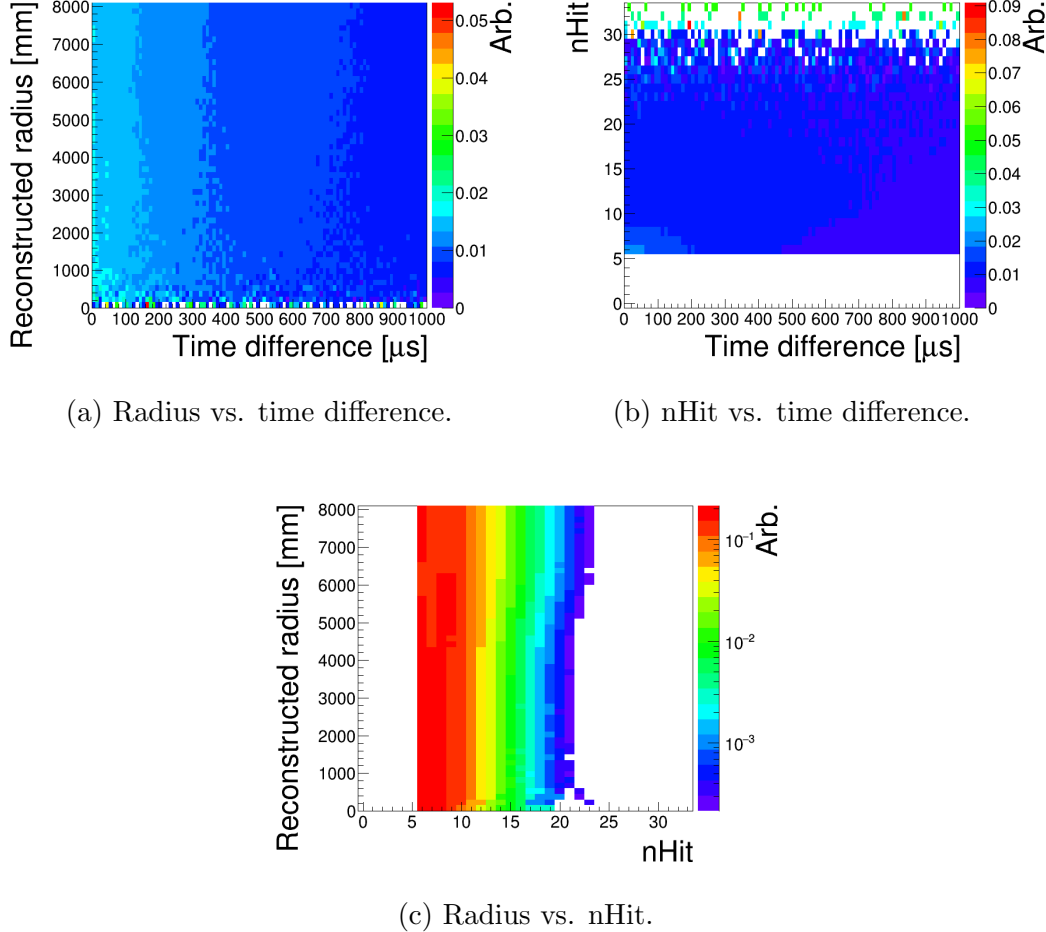


Figure 5.7: Two dimensional distributions of 2.6 live days data collected by the SNO+ detector. Each y-axis bin has been normalized individually.

From the distributions seen in Figures 5.7a and 5.7b, it is clear that there is no correlation between the time between events and the reconstructed radius or nHit of those events. This is expected if the events are independent of one another (i.e. one event should not affect the next).

There is some visible structure in the relationship between an event's reconstructed position and its nHit. Events that are closer to the acrylic have a

slightly larger nHit. This is expected as these events on average have less light attenuated. Additionally, there are more low nHit events closer to the centre of the detector. This is also expected as the N20 triggers are designed to increase sensitivity to central events. The correlation between an event's position and its nHit will need to be taken into account later when sampling.

### Sampling: Time Difference

Each iteration of the toy Monte Carlo begins by generating a pair of fake events. That pair of events is first assigned a time difference. This is performed in several steps. First an exponential is fit (Figure 5.8a) to the time difference between events  $\Delta t$  in the detector data seen in Figure 5.6a (first restricting this data to only events that reconstruct with the central water volume):

$$W_{\Delta t} = a e^{-b \Delta t} \quad (5.3)$$

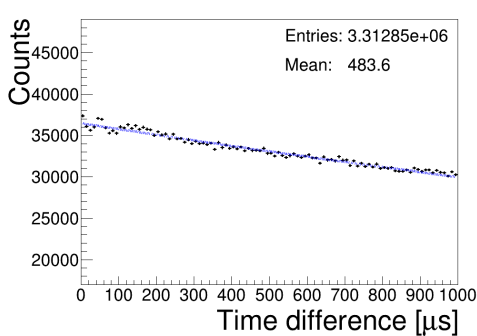
with  $a$  and  $b$  as fit parameters. Afterwards, the value of  $a$  is set to 1 to increase sampling efficiency.

A random time  $\Delta t_i$  from  $0 - 1000 \mu\text{s}$  is generated. The value of the exponential function at that time  $W_{\Delta t}(\Delta t_i)$  is evaluated. Finally, a uniform random number between 0 and 1 is drawn. If this number is less than  $W_{\Delta t}(\Delta t_i)$ ,  $\Delta t_i$  is kept as the time difference for that event pair. Otherwise, a new  $\Delta t_i$  is generated and the process repeats until a suitable value is found.

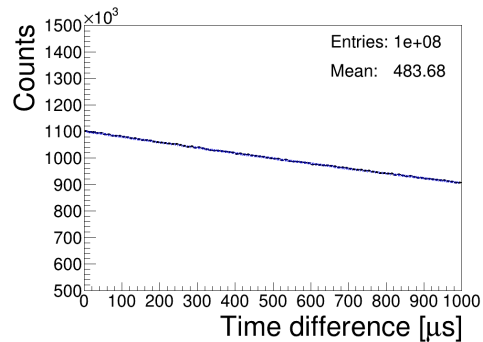
After completing the iterations, the time difference between the fake events is plotted along with the exponential function  $W_{\Delta t}$  in Figure 5.8b. The agreement simply confirms that the sampling method worked appropriately.

### Sampling: Position

With the time difference now determined, each of the two events in the pair needs position and nHit information. The position of each event is determined



(a) SNO+ detector data.



(b) Toy Monte Carlo.

Figure 5.8: Distribution of time between events in (a) SNO+ detector data and (b) toy Monte Carlo generated event pairs. The exponential function (dashed blue) is fit to the data in (a) and this same function (with a different normalization) is plotted in (b).

separately and is initially chosen such that it is uniform within the central water volume of the detector. This is done by generating a set of  $(x, y, z)$  coordinates where each is chosen as a uniform random number between  $-6000$  mm and  $6000$  mm. If the chosen  $(x, y, z)$  has a radius of  $< 6000$  mm, it is kept, otherwise the process is repeated.

A correction is applied to the chosen uniform  $(x, y, z)$  position. Namely, the relative weight in detector data events reconstructing at the radius  $|(x, y, z)|$  is applied. To determine this weight, each  $x$ -axis bin of the reconstructed radius distribution of Figure 5.6b is divided by the volume represented by that bin (a hollow spherical shell). The resulting weighting function is shown in Figure 5.9. Its maximum has been normalized to 1 to increase sampling efficiency. This function shows that there are more events closer to surface of the acrylic (expected as there are more radioactive backgrounds there) and closer to the centre of the detector (expected as the N<sub>2</sub>O triggers increase sensitivity to these). This weighting ensures that the generated random positions also reflect these phenomena.

The weight is applied by drawing another uniform random number between 0 and 1. If it is less than the value of the weighting function (linearly interpo-

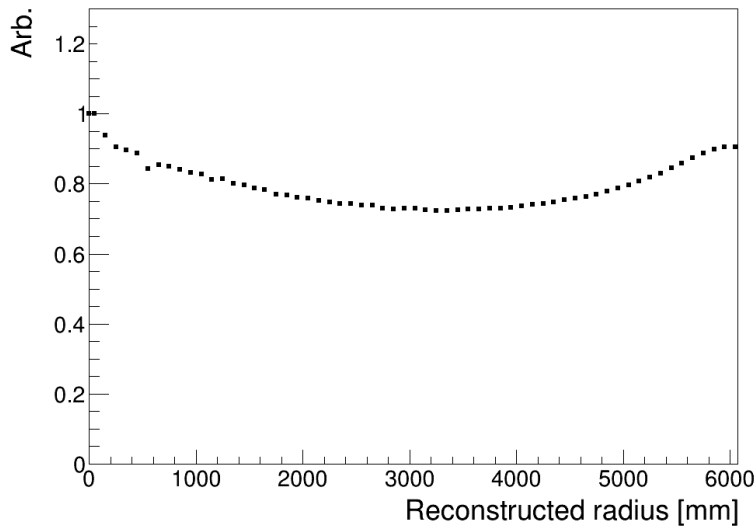


Figure 5.9: Relative probability of an event reconstructing at a given radius within the SNO+ detector.

lating between the points in Figure 5.9) at that radius  $|(x, y, z)|$ , the position is kept, otherwise the process repeats from the beginning with a new uniform  $(x, y, z)$ . The distribution of the radii of the generated positions is compared to those of detector data in Figure 5.10. The agreement here simply shows that sampling uniformly in position and applying relative weight reproduces the radial distribution.

The sampling is performed in this way (using one-dimensional weighting in radius) rather than weighting directly from the three-dimensional  $(x, y, z)$  distribution of detector data due to the statistics. The three-dimensional  $(x, y, z)$  has too many bins, resulting in many having very few to no entries and thus becoming problematic for sampling.

### Sampling: nHit

Lastly, the nHit of each individual event in the pair is chosen. This is done by first taking the projection of the  $y$ -axis bin in Figure 5.7c corresponding to the radius of the sampled event. This results in an nHit distribution for events

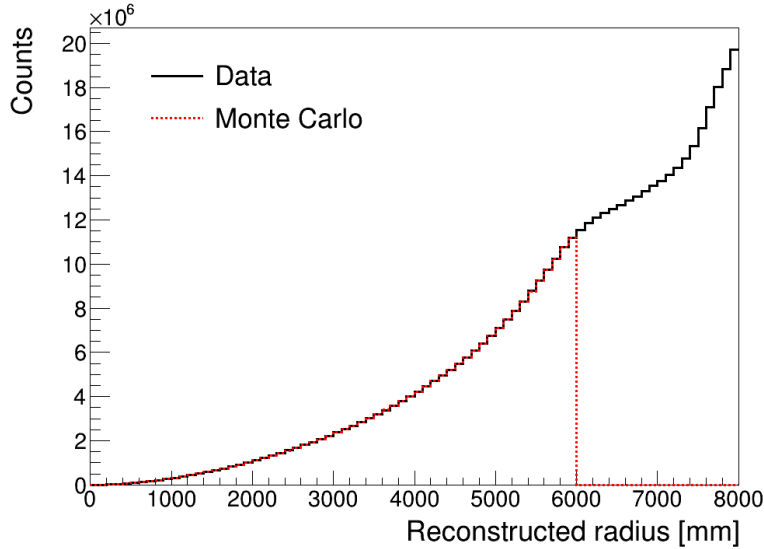


Figure 5.10: Distribution of the reconstructed radii of events in the SNO+ detector data compared to those produced by the toy Monte Carlo.

that would reconstruct at that radius in the detector data. The nHit value is sampled using a uniform random integer generated between 6 – 40. This range is chosen to maximize sampling efficiency. Below 6 nHits, events cannot reconstruct, and above 40 nHits, there are too few events in data.

Another uniform random number is generated between 0 and 1. If this number is less than the value in the nHit distribution at the sampled nHit, the sampled nHit is kept. Otherwise this process repeats with a new sampled nHit until a suitable value is found. Figure 5.11 shows the total nHit distribution of all of the sampled events compared to that of the events in the detector data. Agreement here also only suggests that the sampling was performed correctly.

#### 5.4.4 Comparison to Data

Iterating  $10^8$  times in the manner described in Section 5.4.3, a set of Monte Carlo event pairs was generated. This set of event pairs mimics the subset of data that the antineutrino search (Section 5.3.1) first pass produces (i.e. a subset of events where  $\Delta t < 1000 \mu\text{s}$  and  $r < 6000 \text{ mm}$ ). When the

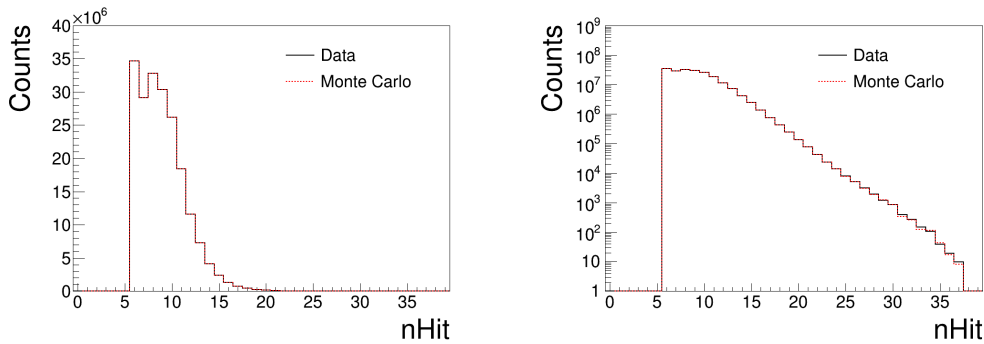


Figure 5.11: Distribution of the  $n_{\text{Hit}}$  of events that reconstructed within the central water volume (radius less than 6000 mm) of the SNO+ detector. Detector data is compared to the toy Monte Carlo simulation, shown in both linear and logarithmic scales.

search is performed over the detector data for the 2.6 live days, approximately 3 million such event pairs are found, so the Monte Carlo contains a factor of  $> 30$  increased statistics. The following comparisons will all be made to this same data subset. To produce these comparisons, the second pass of the antineutrino search is performed identically on both the detector data and Monte Carlo generated subset of event pairs.

The second pass initially selects event pairs where both are within a fiducial volume, where  $r < 5500$  mm. Figure 5.12 shows the comparison of the time difference of the surviving event pairs between the detector data and the toy Monte Carlo simulation. The agreement in this figure indicates that the event pairs that are in coincidence in data follow the overall timing of all events.

Events that then have a time difference  $> 500 \mu\text{s}$  are subsequently removed. Figure 5.13 shows the comparison of the position difference between the remaining event pairs. The agreement seen in this figure supports the assumptions made earlier in the sampling. Namely, that events are uniformly distributed in position within the detector (with corrections that oversample at the centre and at the acrylic) and that the positions of the two events in each pair are uncorrelated.

A very small shift can be seen between the detector data and the Monte

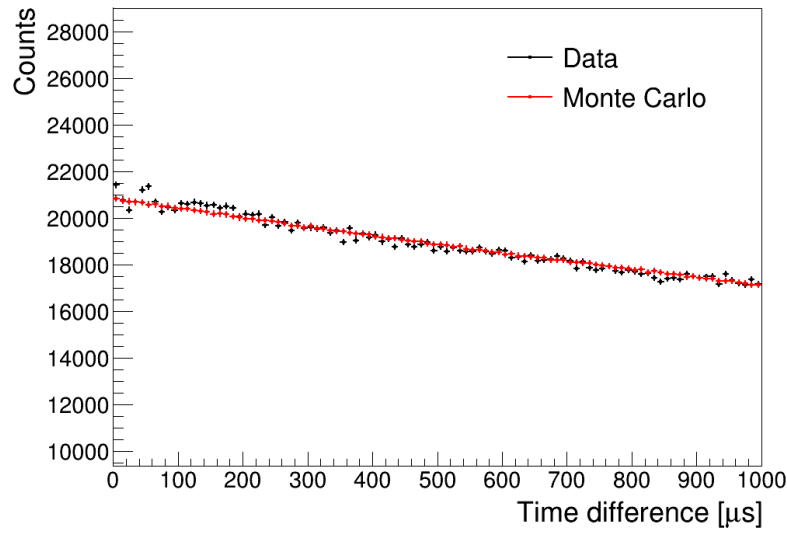


Figure 5.12: Distribution of the time between events in the SNO+ detector data compared to those produced by the toy Monte Carlo simulation. The subset of event pairs includes only those where both are within a 5500 mm fiducial volume.

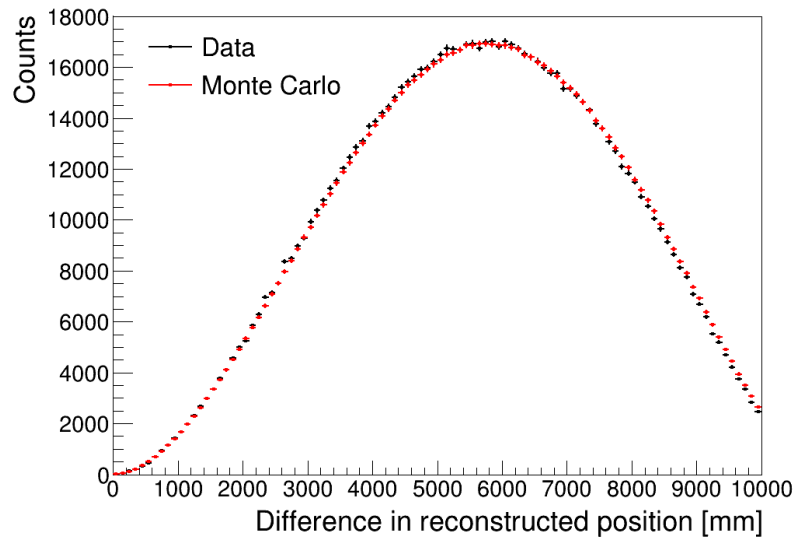


Figure 5.13: Distribution of the position difference between coincident events in the SNO+ detector data compared to those produced by the toy Monte Carlo simulation. The subset of event pairs includes only those where both are within a 5500 mm fiducial volume and have a time difference of  $< 500 \mu\text{s}$ .

Carlo simulation, where the data have slightly closer positions on average. During this time period of data collection, there was an area of increased radioactivity in the water outside of the acrylic vessel (as a result of water recirculation) [128]. This area was located near the top of the detector and consequently resulted in a slightly higher total event rate in the upper hemisphere (as some of these external events will reconstruct to within the central volume). With a higher event rate in the upper hemisphere, there is a slightly increased probability that event pairs will be closer together on average.

Lastly, only events that have a position difference of  $< 2000$  mm are kept. Figure 5.14 shows the side-by-side comparison between the nHit of these remaining event pairs. Although the statistics are poor for the detector data, a similar structure is seen in both distributions. This indicates that the events that are coincident in time and space within the detector each follow the overall nHit distribution of detector data.

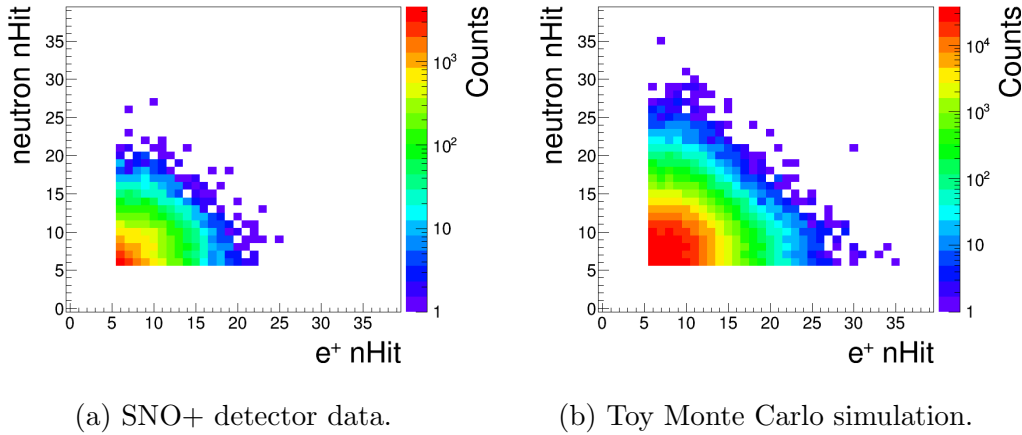


Figure 5.14: Distribution of the nHit of each event pair in the SNO+ detector data compared to the toy Monte Carlo simulation. This includes only the subset of event pairs that are within a 5500 mm fiducial volume, have a time difference of  $< 500 \mu\text{s}$ , and a position difference of  $< 2000$  mm.

### 5.4.5 Conclusions

Based on the agreement seen in these comparisons, it is concluded that the original hypothesis is correct. This indicates that the primary background to the antineutrino signal comes from accidental coincidences between uncorrelated events within the detector.

More importantly, the results of the antineutrino search on the toy Monte Carlo generated event pairs provide high statistics distributions to serve as background. Additionally, this background Monte Carlo contains no signal (whereas the detector data it was being compared to may have some contribution from antineutrinos). This toy model will enable the subsequent optimization of the antineutrino selection criteria.

## 5.5 Wavelength Shifter Improvements

Pure water Cherenkov detectors are not normally used to detect antineutrinos, rather different strategies are normally employed (Section 3.5.1). The difficulty in using a pure water detector was illustrated in Figure 5.5, where the neutrons produce very little light (around the detector’s threshold). This also poses a challenge in reconstructing the position of such interactions, seen in Figure 5.4.

The same Monte Carlo simulation, described in Section 5.1, was used to explore how the SNO+ detector can be improved in regards to measuring the signal from antineutrinos. Prior to the beginning of its water phase, the possibility of adding a wavelength shifting compound into the water was evaluated.

### 5.5.1 Overview

The number of Cherenkov photons produced by charged particles increases with shorter wavelengths [129]. This causes more of this light to lie in the violet and ultra-violet (UV) part of the electromagnetic spectrum. However, most PMTs

become insensitive to light at low wavelengths. This effect is illustrated in Figure 5.15 for the SNO+ PMTs [130].

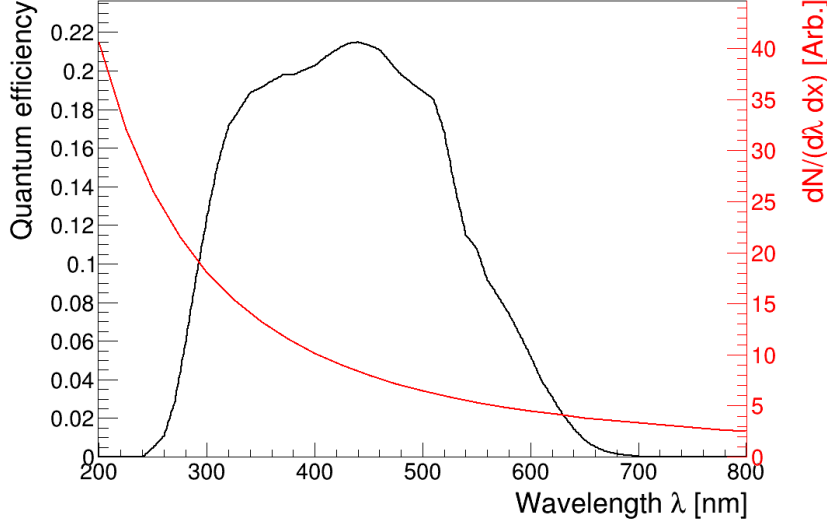


Figure 5.15: Cherenkov emission compared to the quantum efficiency of the SNO+ PMTs as a function of wavelength.

Additionally, UV photons are unlikely to be transmitted through the acrylic as the absorption length drops sharply for photons below 350 nm [131]. To increase the detection of the Cherenkov photons, wavelength shifters may be used. These are compounds that absorb the UV photons and subsequently re-emit them at longer wavelengths.

Previous work by Dai et al. [132] evaluated the effect of using such wavelength shifters for future phases of the SNO experiment. A similar evaluation was performed at the University of Alberta. The results of this evaluation, specifically for the case of the reactor antineutrino signal, will be detailed.

### 5.5.2 Wavelength Shifter Details

The wavelength shifter in question consisted of 1,4-Bis(2-methylstyryl)benzene (Bis-MSB). This compound has been previously evaluated and meets the radio-purity and acrylic compatibility standards of the SNO+ experiment. Bis-MSB

was proposed to be added to the water to reach a concentration of 0.005 ppm, corresponding to a total mass of 80 g.

At this concentration, the absorption length of the photons with wavelengths below 400 nm is approximately 10 cm [133]. With a fluorescence time of 1.5 ns, the emission of light at longer wavelengths happens shortly after absorption [134]. These photons are emitted following the spectrum shown in Figure 5.16 [97], which also includes the relative absorption coefficient.

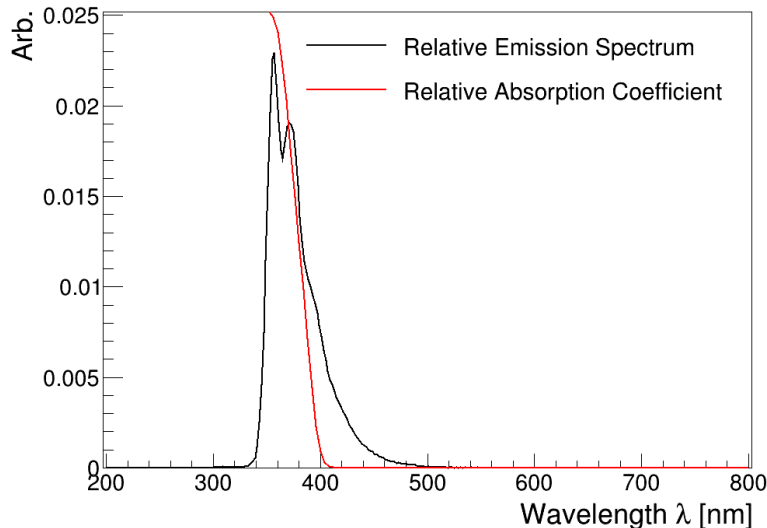


Figure 5.16: Relative Bis-MSB absorption coefficient and emission as a function of wavelength.

The re-emitted photons have a greater probability of being detected compared to the original Cherenkov photons. This effect has been shown to result in approximately 2.6 times more detected photons for an event in the detector, at these concentrations [135].

### 5.5.3 Reactor Antineutrino Effect

The absorption and re-emission of the wavelength-shifted photons was incorporated into the Monte Carlo simulation of the SNO+ detector. Simulations

of IBD interactions in the detector were performed with the inclusion of wavelength shifter for the closest three nuclear reactors: the Bruce, Pickering, and Darlington nuclear reactors.

At the time of these simulations, the SNO+ detector was not yet filled with water. Consequently, these trigger settings are not representative of the current operating conditions. For these simulations, the lowest trigger setting had a nominal value of 12 nHit (compared to the actual current lowest value of 7 nHit).

Figure 5.17 illustrates the effect that the wavelength shifter has on the nHit of the  $e^+$  and neutron events. This is the principal advantage of the wavelength shifter. As a result of this increase, a much greater total number of neutron events are seen to trigger the detector (at these thresholds). For the  $e^+$  events, slightly more events are also seen to trigger the detector. The increased nHit is seen a broadening of Figure 5.17a to Figure 5.17c, where the total integral increases slightly. As a result of this broadening, the peaked structure that results from neutrino oscillations can potentially be distinguished (crucially important to make a measurement of  $\Delta m_{12}^2$ ). With these simulated trigger settings, four times more simulated IBD event pairs triggered the detector.

The increased nHit of each event also allows for a more precise reconstruction. Additionally, the isotropically re-emitted light is advantageous for reconstructing the event positions. The impact of the wavelength shifter on the position difference distribution between simulated IBD event pairs is shown in Figure 5.18. The addition of Bis-MSB into the detector results in a slightly narrower distribution.

#### 5.5.4 Outlook

The addition of Bis-MSB into the water during the water phase of the SNO+ experiment was determined to be advantageous to the search for antineutrinos. Ultimately, the decision was made to not proceed with the addition of

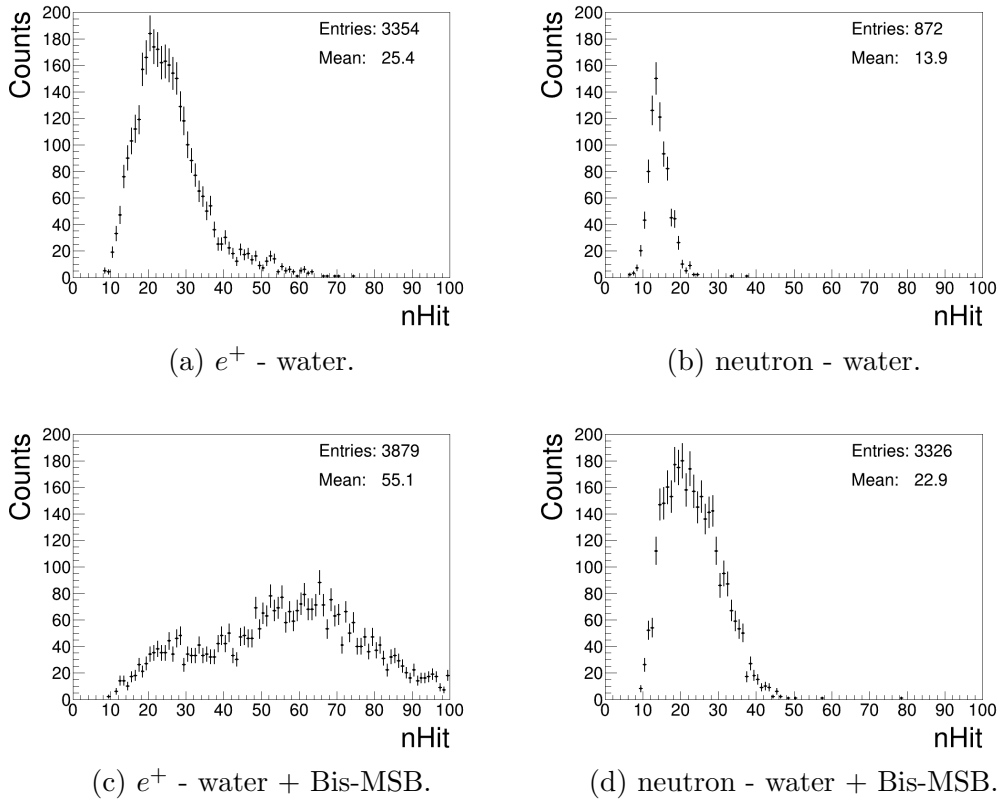


Figure 5.17: nHit distributions for the  $e^+$  and neutron events for the cases of water only and water with Bis-MSB.

wavelength shifter for two primary reasons:

- The recirculation and repurification of water within the detector would remove any added Bis-MSB. This would require the constant addition of Bis-MSB, making it difficult to maintain stable optical properties over time. The recirculation is necessary to remove embedded radioactivity that will leach out of the acrylic during the water phase.
- The water phase of the experiment is temporary and short. The water phase is designed as a transitional phase before the addition of liquid scintillator. During this phase, the goals include obtaining an understanding of the backgrounds and performing solar neutrino and nucleon decay analyses. The addition of a wavelength shifter was seen as an unnecessary

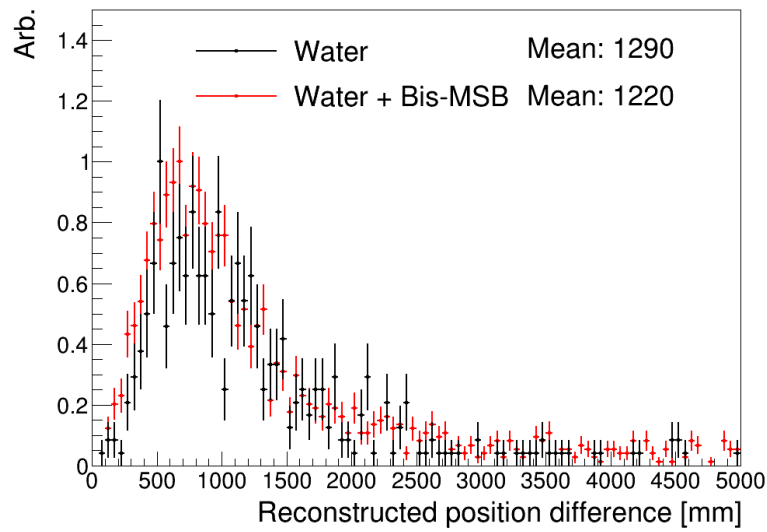


Figure 5.18: Comparison of the reconstructed position difference between events for the cases of water and water with Bis-MSB.

complication during this short phase.

In the event of extended data collection with a water Cherenkov detector, the addition of wavelength shifter is a viable possibility to increase sensitivity to low energy neutrino physics, one case being reactor antineutrinos.

# Chapter 6

## Optimizing the Search for Antineutrinos

With an algorithm and a set of Monte Carlo simulations for both the antineutrinos and the background, a final set of selection criteria can be chosen and a search can be performed. However, the uncertainty on how well the simulation models the complex antineutrino signal is large. To better determine what this signal will look like in the SNO+ detector, a physical calibration was performed.

### 6.1 AmBe Source Calibration

An AmBe source is ideal for this calibration as it very closely mimics the signal of IBD. The first part of coincident signal differs (a 4.4 MeV  $\gamma$  ray versus a 0–8 MeV  $e^+$ ), though, importantly, the second part of the signal is identical. As the 4.4 MeV  $\gamma$  ray and the  $e^+$  travel a negligible distance (compared to the reconstruction’s spatial resolution) before producing light, the AmBe calibration source can be used to precisely determine the time difference and position difference distributions expected from an antineutrino signal. Crucially, it determines exactly what an event from a neutron will look like in the detector.

This is difficult to model as neutrons produce events that are near the detector's threshold.

### 6.1.1 AmBe Source

The AmBe source used for the calibrations is an SNA02 that was manufactured by CERCA's Radioactivity Standards Laboratory (LEA) [136]. Similar to the source used in the experiments performed in Chapter 4, this source consists of powdered mixture of americium and beryllium encapsulated in two layers of 0.8 mm thick stainless steel. To enable the connection of the source onto the hardware that lowers it into the detector, the source has a further three layers of Delrin plastic encapsulation (with a total thickness of 13 mm) [136]. This additionally conforms to the cleanliness requirements of the SNO+ experiment.

The activity of this specific source was previously measured by Loach to be  $68.70 \pm 0.74$  n/s [137]. Correcting for the time since this measurement, the source strength was  $67.28 \pm 0.72$  n/s at the time of the SNO+ calibrations.

### 6.1.2 Deployment

The AmBe source was deployed within the SNO+ detector over the period of January 19–21, 2018 [138]. During this time, a total of approximately 15 hours of data were collected with the detector while the AmBe source was inside. This data set consisted of a 3 hour long central run followed by a series of 30 minute runs where the source position was changed along the  $x$ ,  $y$ , and  $z$  axes of the detector.

The off-centre runs will prove useful in later quantifying any non-linearities and biases in the neutron detection, which affect the uncertainties associated with the detection efficiency of an antineutrino signal. However, the high statistics central run provides the best data to show how neutrons will appear in the SNO+ detector. Figure 6.1 shows the time, reconstructed radii, and nHit dis-

tributions of all events that form this data set (including both AmBe source signals and backgrounds). These distributions are directly comparable to those seen earlier in Figure 5.6 for backgrounds only.

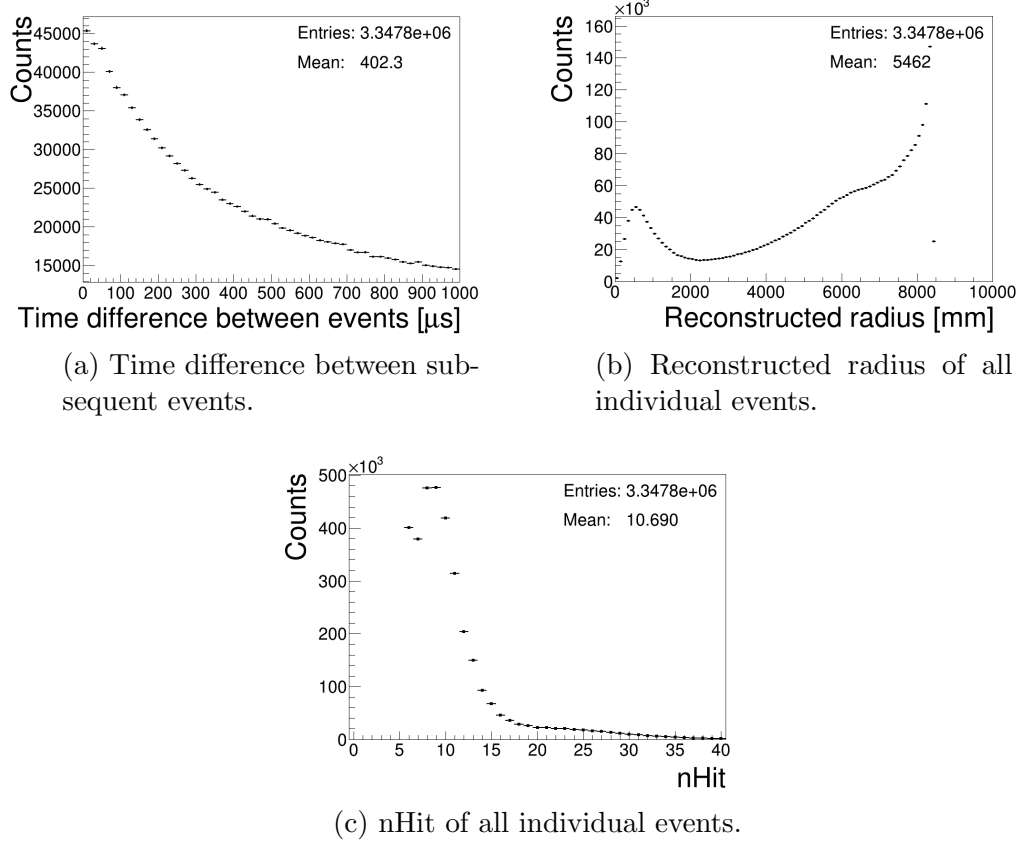


Figure 6.1: Distributions from the data collected by the SNO+ detector with a centrally-placed AmBe source for three hours. Only events that pass data cleaning and successfully reconstruct contribute to these distributions.

### 6.1.3 Neutron Detection

To determine whether an event is a neutron, the 4.4 MeV  $\gamma$  ray is used as a “tag”. Over 50% of the neutrons emitted by the source also have a 4.4 MeV  $\gamma$  ray that accompanies them. In these cases, the emission of the neutron and the  $\gamma$  ray happens simultaneously. The  $\gamma$  ray will scatter or pair produce, triggering the detector very shortly afterwards. The neutron will first thermalize

and eventually capture, but on a much longer time scale. By searching for events in the data set that are separated closely in time, those from neutrons can be distinguished.

### Neutron Identification

To extract the coincident pairs of events (of the  $\gamma$  ray and neutron), the same analysis algorithm described previously in Section 5.3 was used. This produces a list of coincident event pairs where both events have triggered the detector within  $1000 \mu\text{s}$  of each other and have reconstructed within the central water volume.

The neutron is uniquely identified by first looking for a high energy event (here choosing those with an  $\text{nHit} \geq 20$ , above most backgrounds) followed by a second event. Additionally, as the neutron source is placed at the centre (to a precision of  $O(\text{mm})$ ), an aggressive fiducial volume cut is used (3000 mm for both events). This removes the contribution of the increased backgrounds closer to the surface of the acrylic (as they may also be coincident with events from the AmBe source) while preserving the contribution from the neutrons. 3000 mm is much farther than the mean travel distance of the neutron (approximately 200 mm) and many times the reconstruction resolution (roughly 1000 mm from Figure 5.4b). Therefore these criteria will not remove reconstructed neutron events and bias the position difference distribution.

#### 6.1.4 Results

Following the identification of  $\gamma$  ray–neutron coincidence pairs in the data set, several of the different event parameters to be used in the antineutrino search were explored. To better illustrate that these events are from the AmBe source (and differ greatly from the background) comparisons were made to data collected without the AmBe source in the detector.

The comparison data set consists of 2.7 live days of data from January 16–25, 2018, around the same time period as the AmBe calibrations (exact details can be found in Appendix C). The same treatment of looking for coincidence pairs within  $1000 \mu\text{s}$  of each other, followed by applying an  $n\text{Hit} \geq 20$  criteria on the first event and requiring both be within a 3000 m fiducial volume, is applied. These distributions are plotted separately for clarity.

## Time Difference

The time difference between all the event pairs is shown in Figure 6.2 for both the AmBe source and the detector data.

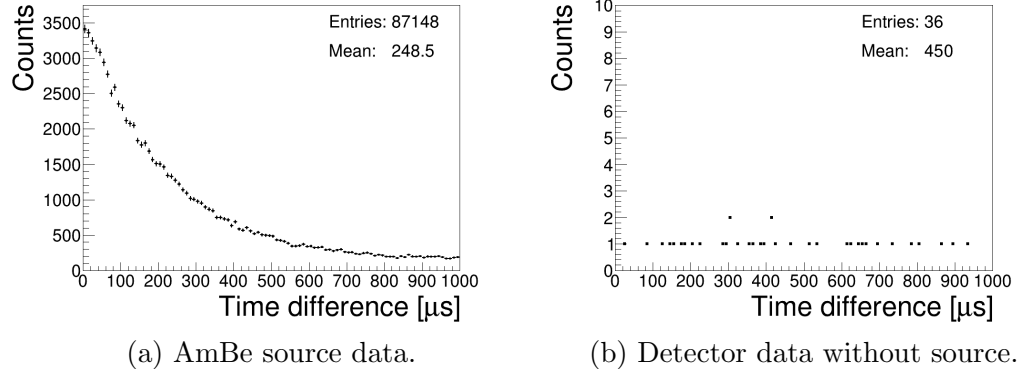


Figure 6.2: Time difference between each event and the next subsequent event in the corresponding data sets.

These plots illustrate the thermalization and capture time of the neutron. Figure 6.2a for the AmBe source also greatly resembles Figure 5.1 (from the antineutrino simulation). Figure 6.2b shows that after the application of fiducial volume and  $n\text{Hit}$  cuts on detector data, very few events survive. This distribution provides the best possible indication of the time separation between the  $e^+$  and the neutron events in an antineutrino signal.

After a time of roughly  $10 \mu\text{s}$  when the neutron initially thermalizes [139], the time difference between events is then also expected to follow an exponential distribution similarly to Figure 5.1. Figure 6.2a shows the time between

each event and the next event. However, there is a contribution from events that are not  $\gamma$  ray-neutron pairs. These are primarily  $\gamma$  rays that are in random coincidence with other  $\gamma$  rays (either from the neutron source or radioactive backgrounds). These coincidences would also be expected to follow an exponential distribution, but with a much longer time constant. This is seen in Figure 6.2a as it levels off to a non-zero value. A fit was performed for the two expected exponential functions that create this distribution:

$$\Delta t = a_n e^{-\frac{\Delta t}{\tau_n}} + a_{\text{bkgd}} e^{-\frac{\Delta t}{\tau_{\text{bkgd}}}} \quad (6.1)$$

where  $\tau_n$  and  $\tau_{\text{bkgd}}$  are the time constants for the neutrons and backgrounds and  $a_n$  and  $a_{\text{bkgd}}$  the corresponding normalization constants. The range of time coincidences was extended up to 2000  $\mu\text{s}$  to better constrain the fit to the background. Figure 6.3 shows the fit to the data where the background component  $a_{\text{bkgd}} e^{-\frac{\Delta t}{\tau_{\text{bkgd}}}}$  is overlaid. This gives a time constant  $\tau_n$  of  $208.1 \pm 1.2 \mu\text{s}$ . This is a measurement of the neutron lifetime in water by the SNO+ detector. A thorough comparison of this lifetime to Monte Carlo simulations and literature values is found later in Section 7.1.3.

The fit shows excellent agreement with the data everywhere, with the exception of the first bin. This bin, corresponding to the number of coincidence pairs within 10  $\mu\text{s}$ , is slightly lower than the fit. This occurs partly due to few  $\mu\text{s}$  it takes for the neutron to first thermalize, before which the capture probability is low [139]. However, there is also an electronic lockout that follows any triggered event in the detector. After the detector triggers, it is prevented from triggering again for a period of 440 ns [140]. This results in a reduction of 4.4% in the number of coincidences in this bin. Correcting the first bin by this factor and repeating the fit results in an insignificant change in the neutron lifetime.

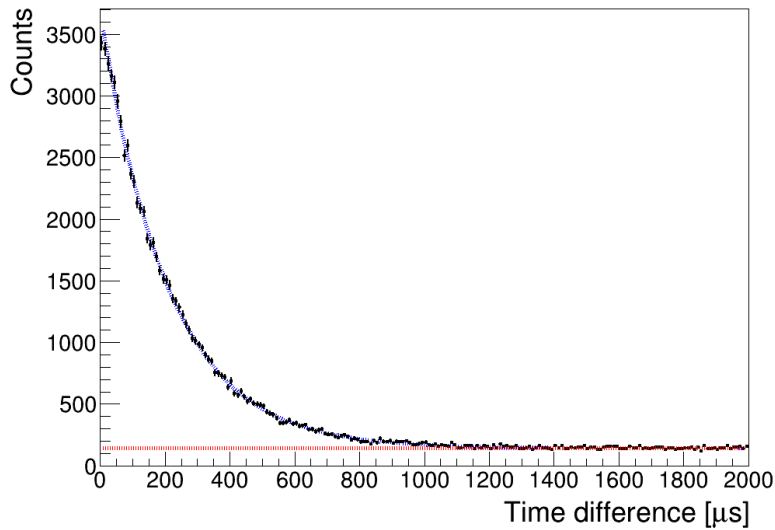


Figure 6.3: Time difference between each event and the next subsequent event for data collected with the AmBe source. The blue dashed line represents a fit to the data and the overlaid red line shows the background component of the fit.

### 6.1.5 Position Difference

The same comparison is performed for the difference in reconstructed positions, shown in Figure 6.4.

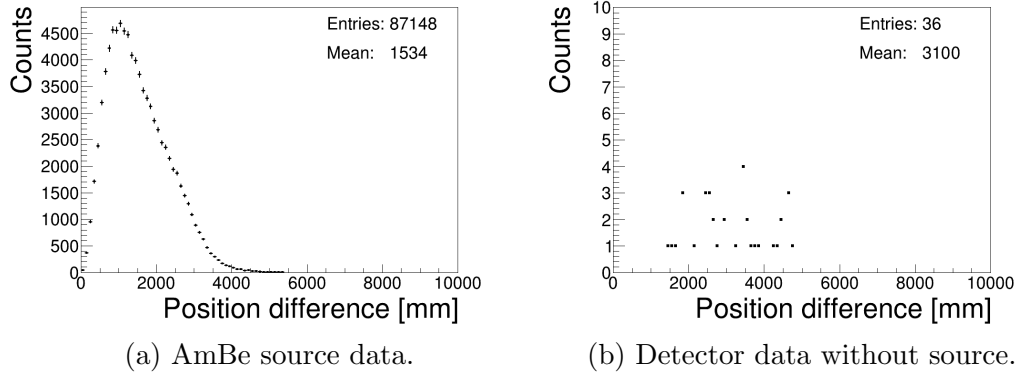


Figure 6.4: Reconstructed position difference between event pairs in the corresponding data sets.

A similar trend is seen in this distribution, where it resembles that of the

antineutrino simulation shown previously in Figure 5.3. Given that this parameter is based on the reconstruction of neutron events in the detector, it will also provide the best estimate of this distribution for an antineutrino signal.

### 6.1.6 nHit

From the plots shown so far, it is concluded that measured events pairs occurred close in time and space. To definitively determine if some of these events were neutrons, the nHit of the triggered events must be evaluated.

The signal from a tagged neutron first includes a high energy event from the 4.4 MeV  $\gamma$  ray (high in nHit), followed by a second lower energy event (low in nHit). To remove the maximal amount of contamination from backgrounds, a different set of selection criteria was applied. To fully describe the nHit distribution of the 4.4 MeV  $\gamma$  ray, no nHit cut was used on the first event.

Aggressive cuts, requiring a time difference of  $< 200 \mu\text{s}$  and position difference of  $< 1000 \text{ mm}$  (keeping a 3000 mm radius requirement), were instead used. This dramatically reduces background contamination, as the probability for background events occurring within this short time interval and small spatial region is negligible. Applying these cuts, the nHit distributions of the two events in each coincident pair are constructed and shown in Figure 6.5.

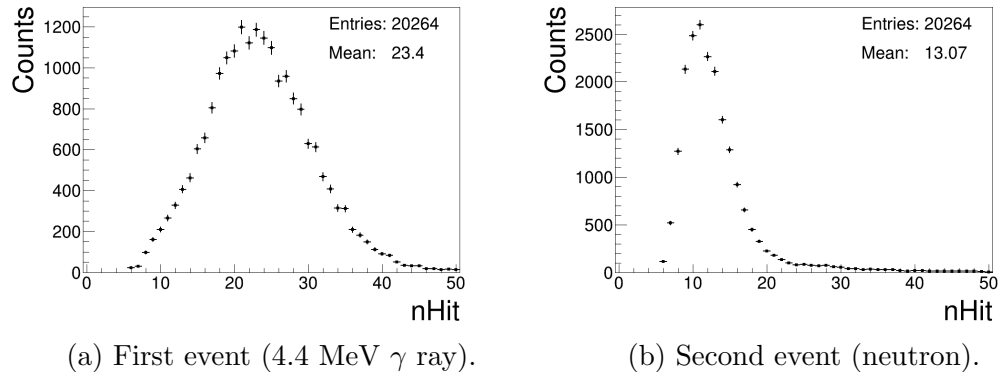


Figure 6.5: nHit distribution of the individual events in the coincidence event pairs for data collected with the AmBe source.

Observing the expected high energy event followed by a second lower energy event suggests that the data constitutes a measurement of neutrons in the SNO+ detector.

The nHit distribution of the 4.4 MeV  $\gamma$  ray cannot be directly used to determine cuts for the  $e^+$  of the antineutrino signal. Instead, simulations must be used. However, the nHit distribution of the neutron will be used later to explore the possibility of additional antineutrino selection criteria.

## 6.2 Cut Optimization

The simulations of the antineutrino signal, the toy Monte Carlo simulation of the background, and the AmBe source calibrations provide the key components needed to create an optimized search for antineutrinos. To do this, separate data sets are required: one with only signal and one with only background.

The background model is straightforward and has already been shown to well represent the data collected by the detector in Section 5.4. This data set, containing the simulated coincidence pairs, will be used directly as the background.

The signal data set is more complicated. While the AmBe source calibration provides the best representation of what a possible antineutrino signal would look like, the first event differs between the calibration data and IBD events (a 4.4 MeV  $\gamma$  ray vs. a 0–8 MeV  $e^+$ ).

To choose the best values for the selection criteria, the AmBe source data was used preferentially where possible. This includes the optimization of the following selection criteria:

- Time difference
- Position difference
- Neutron nHit

As the AmBe source does not replicate well the  $e^+$  of the IBD signal, and is also a point-source (whereas antineutrino interactions occur uniformly), the following selection criteria will require the use of the antineutrino simulation:

- Positron nHit
- Fiducial volume

Ideally, a multivariate approach would be used to perform these optimizations to exploit any correlations between the different search criteria. This approach requires a single set of events that represents the signal. As two different sources will be used to most accurately represent the expected antineutrino signal, it is not possible to properly construct such a set of events. Therefore, it was also not be possible to optimize all selection criteria simultaneously. However, as these selection criteria have been and will be shown to be largely uncorrelated, the result from these primarily 1-dimensional optimizations would differ little from a multivariate approach.

An optimum value for each selection criterion was be chosen. This consists of looking at how the signal acceptance changes as a function of that cut variable, and how the background acceptance changes correspondingly. With each data set (reactor antineutrino simulation, background simulation, and AmBe data), the total number of events  $N_{\text{total}}$  consists of all event pairs that reconstructed within the central water volume and with a time difference of  $< 1000 \mu\text{s}$ . The signal acceptance ( $SA$ ) after any applied cut is defined as:

$$SA = \frac{\text{Number of signal event pairs passing the cut}}{\text{Total number of signal event pairs}} = \frac{N_{\text{sig meas}}}{N_{\text{sig total}}} \quad (6.2)$$

where  $N_{\text{sig meas}}$  represents the number of signal events that would be “measured” after this cut is applied. Likewise the background acceptance ( $BA$ ) is

defined as:

$$BA = \frac{\text{Number of background event pairs passing the cut}}{\text{Total number of background event pairs}} = \frac{N_{\text{bkgd meas}}}{N_{\text{bkgd total}}} \quad (6.3)$$

At an optimal cut value, a high  $SA$  and a low  $BA$  are desired. The best significance is obtained when the following value is maximal:

$$\frac{N_{\text{sig meas}}}{\sqrt{N_{\text{bkgd meas}}}} \quad (6.4)$$

This is related to the  $SA$  and  $BA$  as:

$$\frac{N_{\text{sig meas}}}{\sqrt{N_{\text{bkgd meas}}}} = \frac{N_{\text{sig total}}}{\sqrt{N_{\text{bkgd total}}}} \frac{SA}{\sqrt{BA}} \quad (6.5)$$

As the term  $\frac{N_{\text{sig total}}}{\sqrt{N_{\text{bkgd total}}}}$  is constant while varying the cut parameter, it is enough to maximize  $\frac{SA}{\sqrt{BA}}$  to obtain the optimial value of a given cut parameter. A more thorough treatment of this effect is detailed in Appendix D. The following sections will describe this procedure individually for the different selection criteria.

### 6.2.1 Time Difference

The most fundamental criterion to optimize is the time difference, as a coincident event pair uniquely defines an IBD detection. This parameter can possibly be optimized independently of other parameters as two events that separately trigger the detector should not have correlations (each will produce a unique burst of light in the detector). However, in the case of an antineutrino signal, the time difference between neutron emission and capture is slightly correlated to the distance that the neutron travels, as shown in Figure 6.6. This shows that a neutron that takes a longer time to capture will travel a slightly longer distance (relative to its point of emission).

This same correlation was looked at in the AmBe source data, as shown in

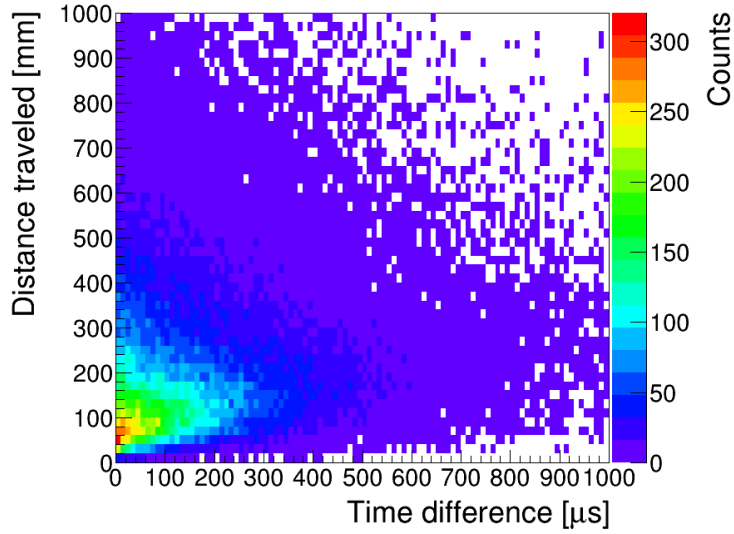


Figure 6.6: Simulated time difference between the emission and capture of the neutron vs. the distance that it has traveled.

Figure 6.7. Here the time difference between events is shown against the reconstructed position difference between them. After the reconstructions, which further smear the position difference, there is no apparent correlation between these two parameters.

With a known neutron capture lifetime, the  $SA$  for antineutrinos is described by the following cumulative distribution function, using  $\tau$  as found in the fit of the data in Figure 6.3:

$$SA = 1 - e^{-\frac{t}{\tau}} \quad (6.6)$$

The  $BA$  was determined from the Monte Carlo simulation by Equation 6.3. These two values as a function of the time difference cut parameter can be seen in Figure 6.8. The  $\frac{SA}{\sqrt{BA}}$  curve has a maximum at a time difference of  $275 \mu s$ . At this value, 73.2% of the signal is kept and 71.0% of the background is rejected.

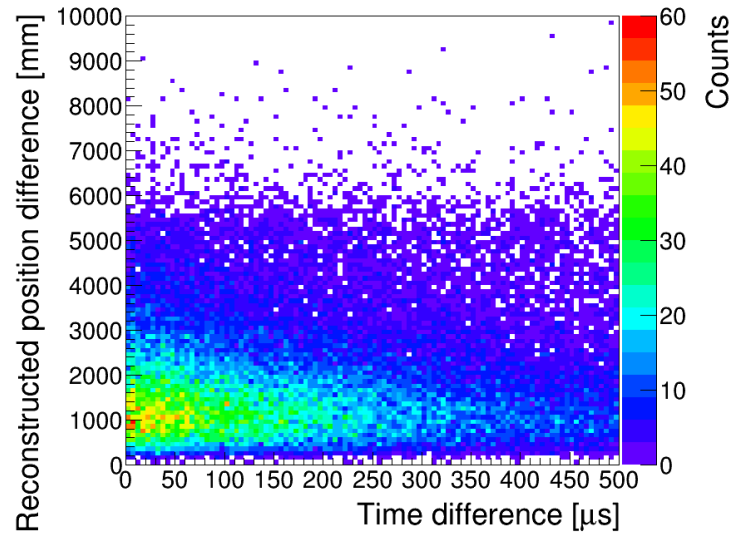


Figure 6.7: Time difference between the events in each coincidence pair from the AmBe source data vs. the difference in the reconstructed positions of that pair.

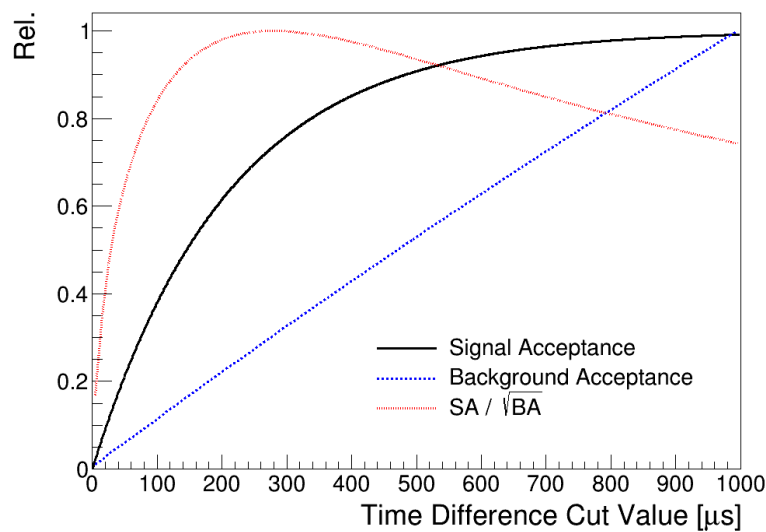


Figure 6.8: Signal and background acceptance as a function of the time difference cut value for coincidence event pairs. The optimal value is found to be  $275 \mu\text{s}$ .

## 6.2.2 Position Difference

The other primary criterion that allows for a drastic reduction in background is the position difference. This was also optimized based on the data collected with the AmBe source. The distribution of this parameter from the AmBe source is shown relative to the distribution from the background simulation in Figure 6.9.

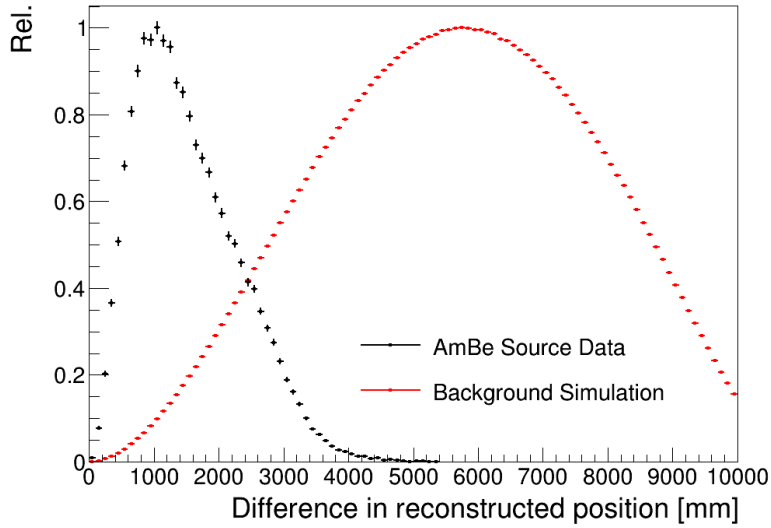


Figure 6.9: Position difference between event pairs for the data collected with the AmBe source compared to the background simulation.

The large separation between these two distributions provides a large discriminating power between signal and background events. The  $SA$  and  $BA$  were constructed from these distributions as a function of this cut parameter to select the optimal value (Figure 6.10).

The  $\frac{SA}{\sqrt{BA}}$  curve has a clear maximum at an aggressive cut value of 1250 mm. Using this value, 45.3% of the antineutrino signal is kept, while 99.2% of the background is rejected.

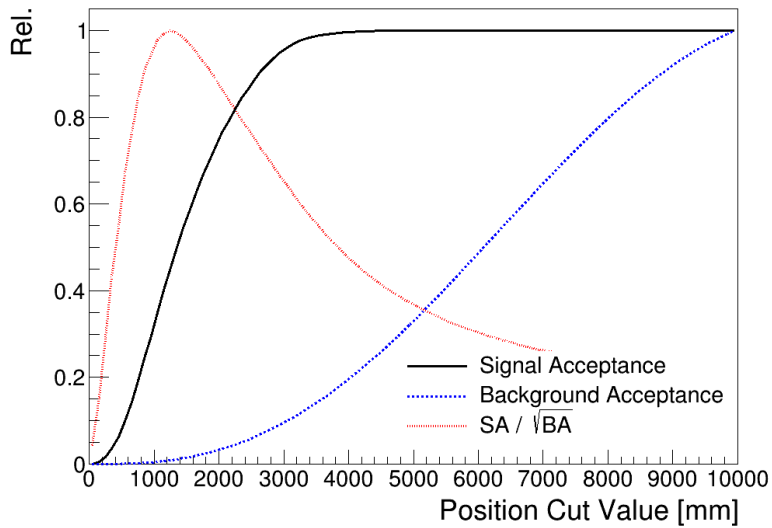
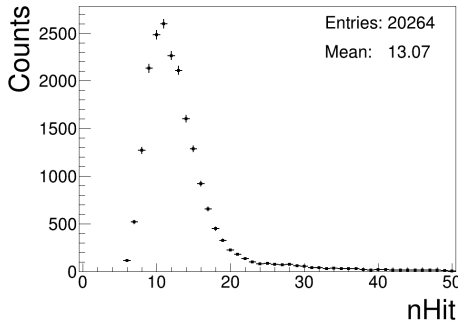


Figure 6.10: Signal and background acceptance as a function of the position difference cut value for coincidence event pairs. The optimal value is found to be 1250 mm.

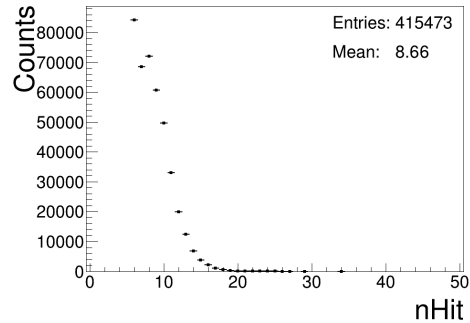
### 6.2.3 Neutron nHit

The last cut parameter that was determined using the AmBe source data is based on the neutron. An nHit cut was explored to determine if any discrimination can be performed to select a possible neutron event over background events. The nHit distributions of the neutron (the second event in the coincidence data set from the AmBe source) and of the simulated backgrounds are compared in Figure 6.11.

These distributions first show that the neutron appears in the same energy range as the backgrounds. This is expected due to the nature of the particles that trigger the detector as a result of neutron interactions. In the case of neutron capture, a 2.2 MeV  $\gamma$  ray is produced. This  $\gamma$  ray will need to produce a charged particle before any light can be emitted in a water-Cherenkov detector. This happens through either pair production, Compton scattering, or the photoelectric effect. Due to the variability in these processes, this will typically result in multiple  $e^-$  produced with a wide variety of energies. Each



(a) AmBe source data.



(b) Background simulation.

Figure 6.11: nHit distribution of the second event in the coincidence event pairs for data collected with the AmBe source compared to the background simulation.

$e^-$  needs to be above the Cherenkov threshold to produce light and once below will no longer emit light. Therefore, some of the energy transferred by the  $\gamma$  ray to these  $e^-$  is not detectable.

The primary backgrounds in the detector come from the decay of naturally occurring radioisotopes present within the central water volume. Many of these backgrounds will also produce  $\gamma$  rays and  $e^-$  with energies in the range of 1–2 MeV. These particles then similarly produce Cherenkov light. This results in the similar distributions in Figure 6.11, as there is little difference in the particles producing light here compared to the neutrons.

Figure 6.11a, however, does show that there is a non-zero population of events with large nHits ( $> 20$ ) in the AmBe source data compared to the background simulation. The IBD simulations (Figure 5.5) showed that there should be very few neutrons that produce this much light. This indicates that these events are coincidence pairs where the 4.4 MeV  $\gamma$  rays from two separate excited  $^{12}\text{C}$  decays are produced within a short time. However, at lower values of nHit, the contribution from this is very small compared to that from neutron events.

Given the similarity of the neutron nHit distribution with that of detector

backgrounds, it may not provide a discriminating power. Therefore, no cut was placed on the neutron nHit in the search for antineutrinos.

#### 6.2.4 $e^+$ nHit

The only method to estimate the nHit distribution from the first event in the coincidence pair (the  $e^+$ ) is through the antineutrino simulation. From Section 5.1, this distribution is shown in Figure 6.12b alongside the data from the AmBe source for comparison.

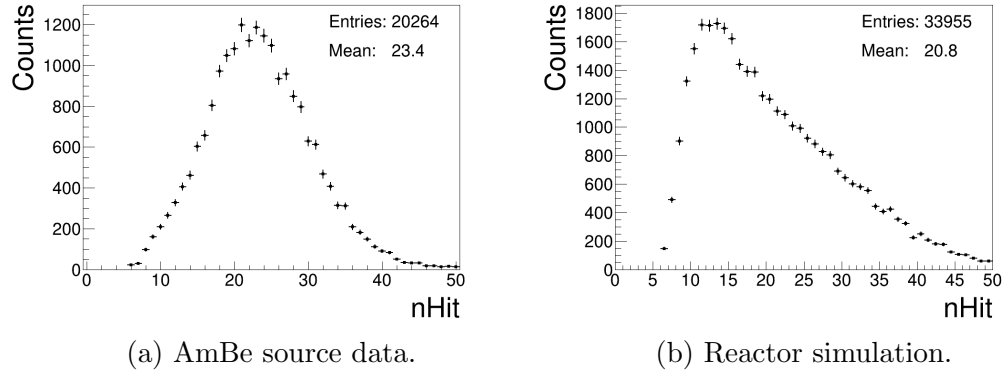
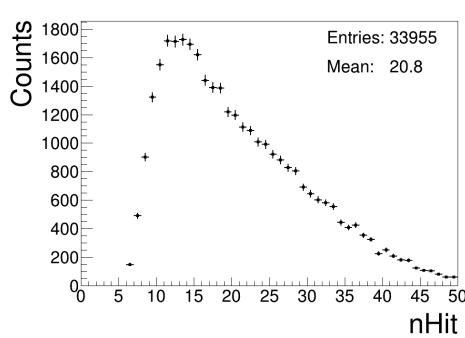


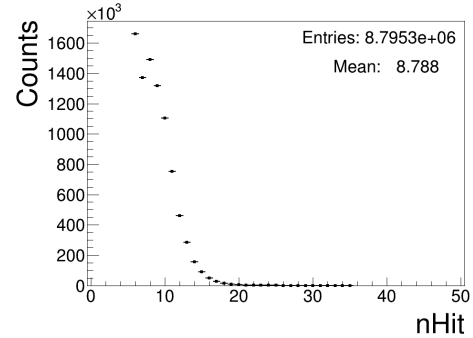
Figure 6.12: nHit distributions of the first event in the coincidence event pairs for the corresponding data sets.

The two distributions differ in that the spectrum for the  $e^+$  is broader as it extends up to higher energy, illustrating why the AmBe source data cannot be used to perform this optimization. Figure 6.13 shows the  $e^+$  nHit distribution compared to that of the background simulation.

As there are very few backgrounds above nHit values of 20, a minimum nHit cut on the first event was tested. For nHit values below 20, the background signal becomes exponentially large. The *SA* and *BA* will be constructed such that they are the fraction of events that survive compared to the total number of events with  $n\text{Hit} \geq 15$  (looking only into the high energy region). These parameters as a function of the nHit cut value are shown in Figure 6.14.



(a) Reactor simulation.



(b) Background simulation.

Figure 6.13: nHit distributions of the first event in the coincidence event pairs for the corresponding data sets.

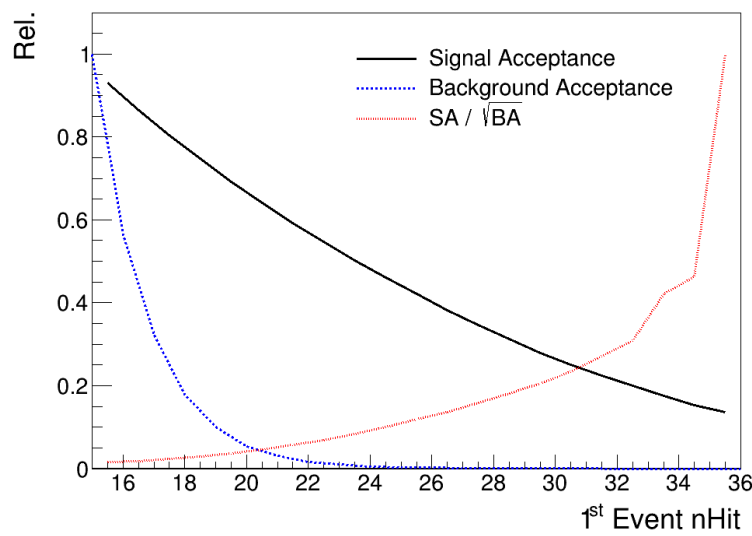


Figure 6.14: Signal and background acceptance as a function of the minimum nHit cut value on the first event of each coincident event pair.

In the nHit distribution of the background events, there are a negligible amount of events with  $n\text{Hit} > 35$ . This is seen as the curve becoming asymptotic at high  $n\text{Hit}$ , after which there are no remaining event pairs in the background data set. While this does not provide an optimal choice for a minimum  $e^+$  nHit cut, it does indicate that such a cut should be used and a high nHit value taken. For this reason, no such cut will be defined yet, but it will be applied on the final data set.

### 6.2.5 Fiducial Volume

The interactions from antineutrinos will occur uniformly within the central water volume. As the AmBe source is a point source when placed within the detector, the antineutrino simulation must again be used to determine cuts based on the absolute positions.

It is well known that at the surface of the acrylic (and beyond), there is increased radioactivity. This results in a larger amount of background events that reconstruct to radii around 6000 mm. For this reason, fiducial volumes are typically used to select only events that occur within a smaller spherical subregion of the detector.

This fiducial volume cut was applied by requiring a maximum reconstructed radius. Any events that reconstruct with a radius larger than this value were removed. Moreover, a fiducial volume cut is applied to both events in each pair. If one or more of the events fail this condition, the pair is rejected.

To determine the optimal value, the SA and BA values were constructed for radii cut values ranging from 1000 to 6000 mm. Figure 6.15 shows how these change as a function of this cut parameter.

The  $\frac{SA}{\sqrt{BA}}$  curve is maximal when using a radius cut of 5000 mm. Alternatively, a separate fiducial volume could be applied to each of the two events in a given pair (as each event pair has two different radii associated to it). This option was explored and likewise the  $\frac{SA}{\sqrt{BA}}$  surface was constructed, shown in

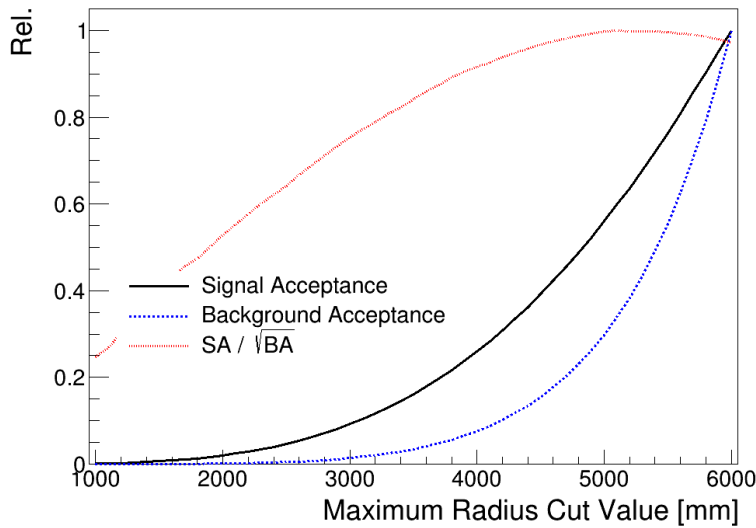


Figure 6.15: Signal and background acceptance as a function of the radius cut value applied to both events in each coincident event pair. The optimal value is found to be 5000 mm.

Figure 6.16.

Performing this optimization in two dimensions yields the same optimal value of 5000 mm for both events. Additionally, the shape of the surface in Figure 6.16 resembles a rotation of the one-dimensional curve in Figure 6.15. This demonstrates that there is no benefit to using two different fiducial volume cuts.

### 6.2.6 Final Selection Criteria

Completing this process, the antineutrino search now has a well-defined list of conditions to apply to detector data. These are summarized in the Table 6.1.

Any pair of events in the detector that passes all of these criteria will be considered an “antineutrino candidate”. With a defined antineutrino search algorithm and a full set of selection criteria, the absolute expectation for the measured signal can now be determined.

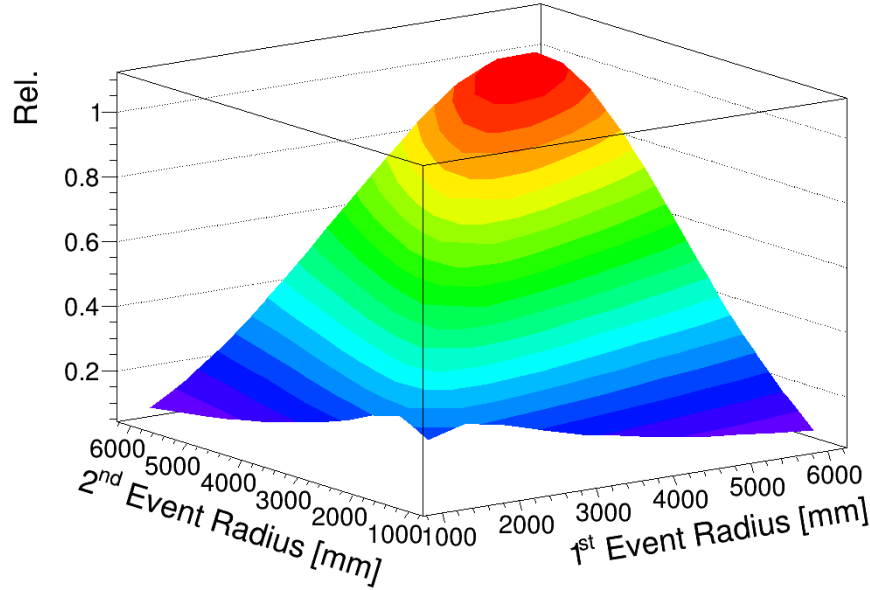


Figure 6.16:  $\frac{SA}{\sqrt{BA}}$  as a function of the radius cut value applied separately to each event in the coincident event pairs. The optimal value is found to be 5000 mm for both events.

Cut Parameter	Minimum Value	Maximum Value
Time difference	–	275 $\mu$ s
Position difference	–	1250 mm
1 <sup>st</sup> event nHit	TBD in Chapter 8	–
2 <sup>nd</sup> event nHit	–	–
1 <sup>st</sup> event radius	–	5000 mm
2 <sup>nd</sup> event radius	–	5000 mm

Table 6.1: Values of the selection criteria used to identify a coincident event pair as an antineutrino candidate.

# Chapter 7

## Signal Efficiency

The signal efficiency is defined as the fraction of IBD events from antineutrinos that pass all of the cuts. Applying this to the previous signal expectation of 115 interactions per year gives the expected rate. To determine the efficiency, a combination of the AmBe source data and the reactor Monte Carlo simulations were used. This again ensures the most accurate determination of the efficiency.

As different simulated and measured data sets were used, the total efficiency of detecting an antineutrino  $\epsilon_{\text{total}}$  was broken up into multiple components,

$$\epsilon_{\text{total}} = \epsilon_{\text{neutron}} \cdot \epsilon_{e^+} \cdot \epsilon_{\text{FV}} \quad (7.1)$$

where:

- $\epsilon_{\text{neutron}}$  is the “neutron tagging” efficiency (i.e. the probability of identifying the following neutron).
- $\epsilon_{e^+}$  is the efficiency of detecting the  $e^+$  (after any nHit cuts are applied).
- $\epsilon_{\text{FV}}$  is the probability that both of the two above events reconstructed to positions within the specified fiducial volume.

Each of these three components are determined separately and will be discussed in the following sections.

## 7.1 Neutron Tagging Efficiency

The neutron tagging efficiency  $\epsilon_{\text{neutron}}$  is defined as the probability of identifying a neutron within the detector. It was determined by looking at the number of neutrons that trigger the detector and pass selection cuts from the AmBe calibration source. Neutrons are “tagged” as part of a coincident signal. Therefore this was done by looking at neutrons that are coincident with 4.4 MeV  $\gamma$  rays from the AmBe source. This efficiency also includes multiple components:

$$\epsilon_{\text{neutron}} = \epsilon_{\text{trigger}} \epsilon_{\Delta t} \epsilon_{\Delta d} \quad (7.2)$$

where:

- $\epsilon_{\text{trigger}}$  is the probability of the detector triggering for a neutron interaction (and also successfully reconstructing).
- $\epsilon_{\Delta t}$  is the fraction of neutrons remaining after applying the time difference cut.
- $\epsilon_{\Delta d}$  is the fraction of neutrons remaining after applying the position difference cut.

### 7.1.1 $\gamma$ ray Event Rate

To determine the efficiency of tagging a neutron, the number of neutrons with corresponding 4.4 MeV  $\gamma$  rays needed to first be determined. With the rate of neutrons precisely known, the rate of these  $\gamma$  rays was measured to determine the expected rate of  $\gamma$  ray–neutron pairs.

This ratio is driven by the energy of the  $\alpha$  particles that interact with the  ${}^9\text{Be}$  nuclei. This energy is affected by factors such as the source type, source composition, and grain size (in the case of powdered sources such as the one used). Therefore, the ratio can vary and is specific to each individually produced AmBe source.

This measurement of the overall rate of 4.4 MeV  $\gamma$  rays was determined by looking at the three hour long run where the AmBe source was placed at the centre of the detector. As the total rate is desired, no cuts were applied to the data set. To extract the rate of these  $\gamma$  rays, the nHit distribution of all events that trigger the detector was examined.

The nHit distribution of the 4.4 MeV  $\gamma$  rays has already been determined previously in Sections 6.1.6. The background to this measurement constitutes all events that triggered the detector, but that were not from particle interactions caused by the AmBe source. The corresponding distribution of these background events is known from the 2.7 days of data taken around the time of the calibrations. These two distributions are compared in Figure 7.1. The nHit distributions for the AmBe source data and background data were then converted to rates and are shown in Figure 7.2.

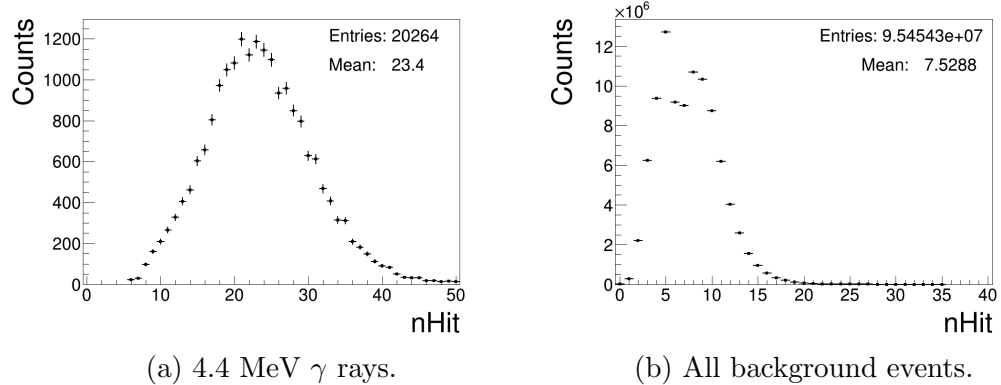


Figure 7.1: nHit distribution of the 4.4 MeV  $\gamma$  ray (a) compared to the nHit distribution of all events from data collected without the source (b).

A large fraction of the 4.4 MeV  $\gamma$  rays from the AmBe source produce enough light that they lie above most backgrounds. This is seen to occur when nHit values are  $\geq 20$ . This region also lies above the neutron contribution to the spectrum (shown for AmBe data in Figure 6.5b). Some of these  $\gamma$  ray events do, however, extend into the lower nHit region.

First a background subtraction of the spectra in Figure 7.2 was performed.

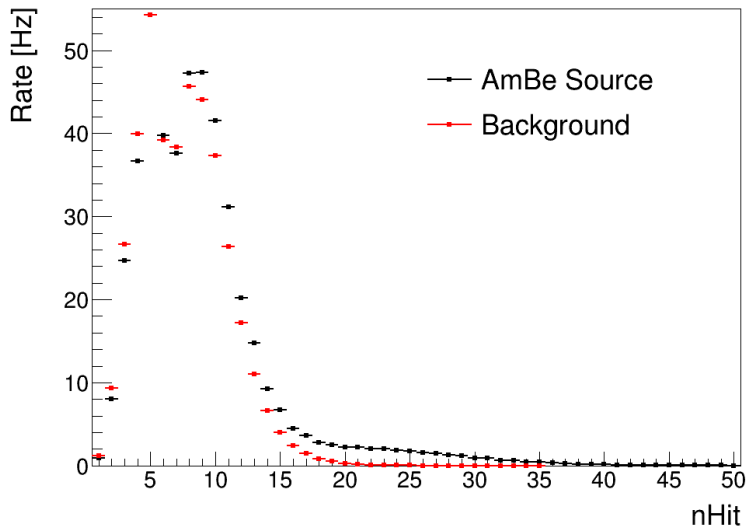


Figure 7.2: nHit distributions of all events for data collected with and without the AmBe source.

Afterwards, only contributions from the AmBe source remain (i.e. from the  $\gamma$  rays, neutrons, and any other radioactive backgrounds inherent in the source hardware). By looking at the high nHit region, the contribution from the 4.4 MeV  $\gamma$  ray could be isolated. This was done by fitting the measured nHit distribution for this  $\gamma$  ray in the region of 20–40 nHit, shown in Figure 7.3.

The fit of the  $\gamma$  ray nHit distribution is integrated to give a total rate of  $34.8 \pm 1.6$  Hz. There is a small probability that the 4.4 MeV  $\gamma$  ray will sometimes fail to trigger the detector. From simulations of this AmBe source measurement, the 4.4 MeV  $\gamma$  ray was found to nearly always (99.5 % of the time) trigger the detector. Applying this slight correction to the  $\gamma$  ray rate and dividing by the neutron rate measured by Loach [137] gives a  $\gamma$  ray to neutron ratio of  $0.520 \pm 0.025$  for this specific AmBe source. Table 7.1 briefly summarizes the relevant statistics in regards to the number and type of particles produced in the three hour central run.

This  $\gamma$  ray to neutron ratio differs from the most recent measurements:  $0.596 \pm 0.015$  [141] and  $0.575 \pm 0.028$  [107]. However, in both these experiments

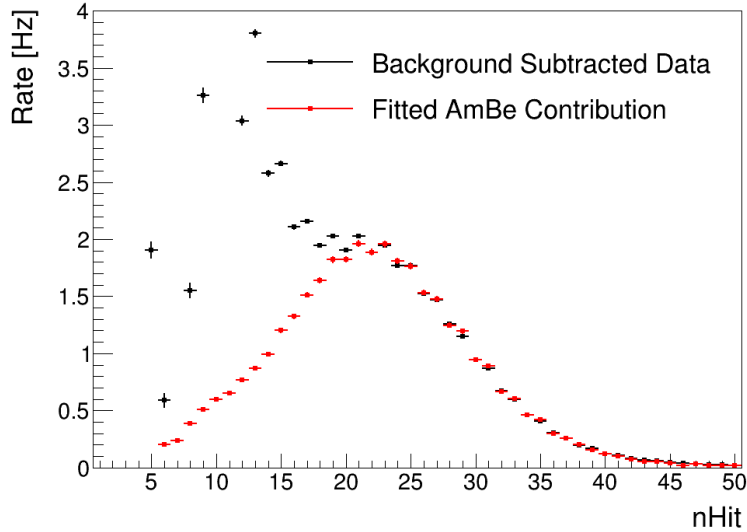


Figure 7.3: Background subtracted nHit distribution of all events in the data collected with the AmBe source. The fitted contribution of the 4.4 MeV  $\gamma$  ray is overlaid.

AmBe Source Statistics	
Number of neutrons produced	$(6.784 \pm 0.073) \times 10^5$
$\gamma$ ray to neutron ratio	$0.520 \pm 0.025$
Number of $\gamma$ ray - neutron pairs produced	$(3.53 \pm 0.16) \times 10^5$

Table 7.1: Summary of the number of particles produced by the AmBe neutron source over the three hour long central run.

the AmBe sources used were  $O(100)$  times stronger than the SNO+ AmBe source. On top of the source to source variation, part of this discrepancy can also come from the small size of the SNO+ source, where surface effects can be more pronounced. Older measurements of a similar strength source ( $0.75 \pm 0.11$  [142]) help illustrate the degree to which this ratio can vary.

### Systematic Uncertainty: nHit Distribution

The rate determination for the 4.4 MeV  $\gamma$  rays relies entirely on knowledge of their nHit distribution. To estimate the accuracy of this distribution, it was compared to the distribution obtained from Monte Carlo simulations of the AmBe source measurements. This comparison is shown in Figure 7.4.

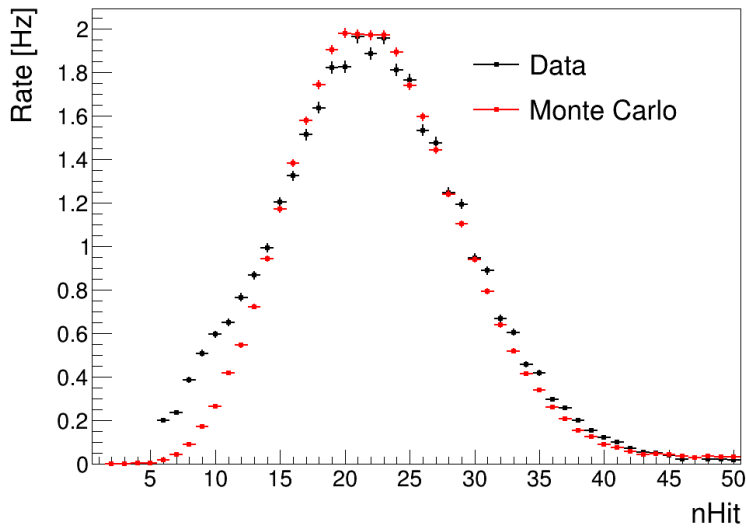


Figure 7.4: Measured nHit distribution of the 4.4 MeV  $\gamma$  ray compared to the corresponding Monte Carlo simulation.

The two distributions show good agreement with the exception of the lowest nHit region. Events in this region are notoriously difficult to model as they are very close to the threshold of detection. Additionally, there may be a small remnant contribution from accidental coincidences with backgrounds. The fit to the background subtracted data was repeated, this time using the nHit distribution as determined from the simulation. This resulted in a 4.6% difference from before and is included as the systematic uncertainty on the  $\gamma$  ray rate.

### 7.1.2 Tagging Efficiency Determination

Accidental coincidences in the AmBe source data originate from the 4.4 MeV  $\gamma$  ray being in coincidence with another such  $\gamma$  ray or in coincidence with a background event. To minimize the contribution of these coincidences, the time difference cut was applied along with the position difference cut. This provides the most accurate neutron tagging efficiency, but does not allow for the separate determination of the trigger efficiency  $\epsilon_{\text{trigger}}$  at this time.

These cuts were applied using the previously determined optimal values of  $275 \mu\text{s}$  and  $1250 \text{ mm}$ . The event pairs that remained in the data set corresponded to the number of detected  $\gamma$  ray-neutron pairs. This gives an efficiency of detecting such pairs  $\epsilon_{\gamma-n}$  of  $0.100 \pm 0.014$ . Again, as the  $4.4 \text{ MeV}$   $\gamma$  ray will sometimes fail to trigger the detector, the neutron tagging efficiency  $\epsilon_{\text{neutron}}$  is determined as:

$$\epsilon_{\text{neutron}} = \frac{\epsilon_{\gamma-n}}{\epsilon_\gamma} \quad (7.3)$$

The efficiency of a  $4.4 \text{ MeV}$   $\gamma$  ray triggering the detector  $\epsilon_\gamma$  was previously found to be 99.5% using simulations of this AmBe source measurement. This slight correction gives a neutron tagging efficiency of  $0.101 \pm 0.014$ .

As the distributions for the time difference and position difference between these event pairs is known, the trigger efficiency  $\epsilon_{\text{trigger}}$  was estimated. From Sections 6.2.1 and 6.2.2, the fraction of events that survive the selection cut values is known. This corresponds to efficiencies of  $\epsilon_{\Delta t} = 0.731 \pm 0.010$  and  $\epsilon_{\Delta d} = 0.453 \pm 0.049$ . Using Equation 7.2, the probability of a neutron triggering the detector and successfully reconstructing is therefore estimated to be  $0.303 \pm 0.042$ .

### 7.1.3 Systematic Uncertainty

#### Detection Anisotropy

One main source of systematic uncertainty with regards to applying this neutron tagging efficiency onto a search for antineutrinos comes from variations in reconstruction and triggering as a function of position. Namely, the reconstruction and trigger efficiencies may not be the same close to the edge of the detector as at the centre. To evaluate this effect, the data from the non-central AmBe runs were analyzed. This data set consists of a series of half-hour long runs that were performed at various  $(x, y, z)$  positions, as listed in Table 7.2.

To best estimate any systematic effect, the neutron tagging efficiency was

AmBe Source Run Positions (x, y, z) [mm]			
(0, 0, 0)	(0, 0, -1500)	(0, 3000, 0)	(0, -1500, -1500)
(0, 0, 1500)	(0, 0, -3000)	(0, 5000, 0)	(0, -1500, 1500)
(0, 0, 3000)	(0, 0, -4500)	(0, -1500, 0)	(0, 1500, 1500)
(0, 0, 4500)	(0, 0, -5000)	(0, -3000, 0)	(0, 2500, -2500)
(0, 0, 5000)	(0, 0, -5500)	(0, -4500, 0)	(0, -2500, -2500)
(0, 0, 5500)	(0, 1500, 0)	(0, 1500, -1500)	

Table 7.2: List of AmBe source positions for which calibration data was collected with the SNO+ detector.

determined in the same manner as in Section 7.1.2 for each of the non-central AmBe runs. Figure 7.5 shows how this efficiency varies as a function of the radius at which the source was placed. These variations include effects due to changes in the trigger efficiency and reconstruction resolution at different detector locations.

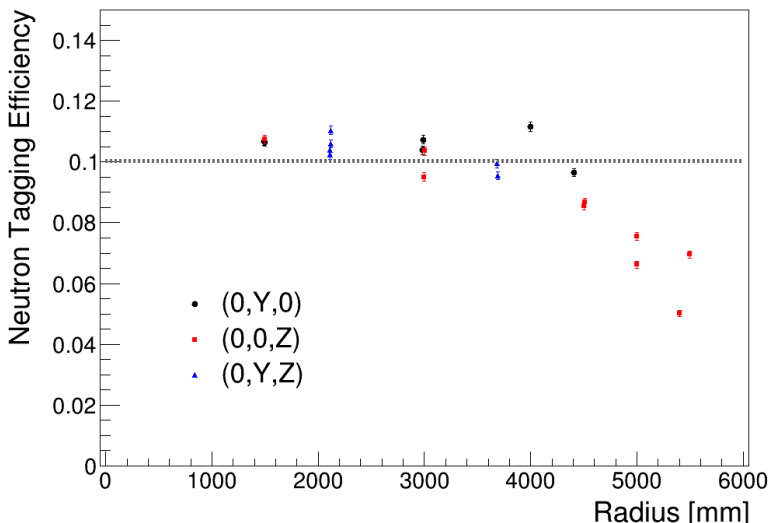


Figure 7.5: Neutron tagging efficiency for a series of runs performed with the AmBe source at various positions within the detector. The dashed line corresponds to the efficiency obtained with the AmBe source at the centre of the detector.

The neutron tagging efficiency is seen to remain relatively constant up to radii of 4500 mm. As the source approaches the edge of the detector, the efficiency is seen to drop. This decrease is likely due to a combination of

effects. Near the edge of the detector, the reconstruction algorithms typically have more difficulty determining the event position [143]. Additionally, with neutrons being close to the threshold of detection, optical effects from scattering and absorption will play a greater role near the acrylic.

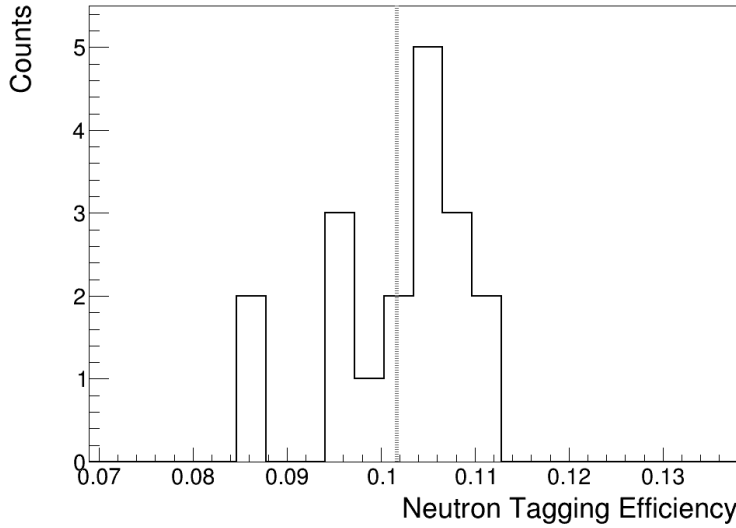


Figure 7.6: Neutron tagging efficiency for a series of runs performed with the AmBe source at various positions within the detector. The dashed line corresponds to the mean coincidence rate.

The neutron tagging efficiencies for a subset of these non-central runs are included as entries in Figure 7.6. This represents a projection of the data in Figure 7.5 onto the  $y$ -axis. The mean  $\mu$  of these data points is also included as the dashed line. The mean differs from the rate obtained from the three hour long central run with the AmBe source by 1.0%. Only runs where the source is located up to 4500 mm from the centre were used. This ensures that the efficiency is being determined using neutrons that are well within the 5000 mm fiducial volume used in the antineutrino analysis. When the source is placed at 5000 mm, nearly half of the neutrons will reconstruct outside of the fiducial volume. Therefore, the corresponding efficiencies are no longer representative of the antineutrino search.

The variance of the data points  $r_i$  in Figure 7.6 is then determined as:

$$\text{Var}(r) = \frac{1}{n-1} \sum_i^n (r_i - \mu)^2 \quad (7.4)$$

The systematic uncertainty assigned to this efficiency is determined as the square root of the variance. This assigns a 7.1% systematic uncertainty to the efficiency of detecting the neutron event  $\epsilon_{\text{neutron}}$ .

## Reconstruction Resolution

The position difference cut is a key component of the neutron tagging efficiency. Determining it from the AmBe source and using it to detect antineutrinos relies on the assumption that the position resolution of the 4.4  $\gamma$  ray is similar to that of the  $e^+$  from IBD.

The position difference distribution is predominately formed as a result of the position resolutions (rather than the travel distance of the neutron). It is possible that the position resolution of the  $e^+$  differs from that of the 4.4 MeV  $\gamma$  rays. This is further complicated by the fact the the  $e^+$  cover a wide range of energies. Higher energy interactions (producing more light) will tend to reconstruct more precisely, having a better resolution.

The antineutrino search only looks for the highest energy  $e^+$ , producing events with nHit values upwards of 30, corresponding roughly to 4 MeV charged particles [144]. To estimate this possible systematic effect, two sets of calibration data were compared. The first corresponded to the 4.4 MeV  $\gamma$  rays from the AmBe source calibrations. The later consisted of the data collected with a  $^{16}\text{N}$  source placed within the detector [145]. The associated systematic uncertainty was estimated by looking at the impact that the position resolutions (from the two different calibration sources) had on the position difference distribution.

The  $\beta^-$  decay of  $^{16}\text{N}$  primarily produces a 6.1 MeV  $\gamma$  ray (67%) and less frequently a 7.1 MeV  $\gamma$  ray (5%) [146]. Unlike the AmBe source, these  $\gamma$  rays

are produced in coincidence with energetic  $e^-$ . Within the  $^{16}\text{N}$  source, a PMT is optically coupled to plastic scintillator that surrounds the decay chamber. These  $e^-$  have sufficient energy to be detected by this PMT, but not enough to leave the source. By only looking at detector data in coincidence with signals from this internal PMT, the collected data is essentially free of background contamination [147].

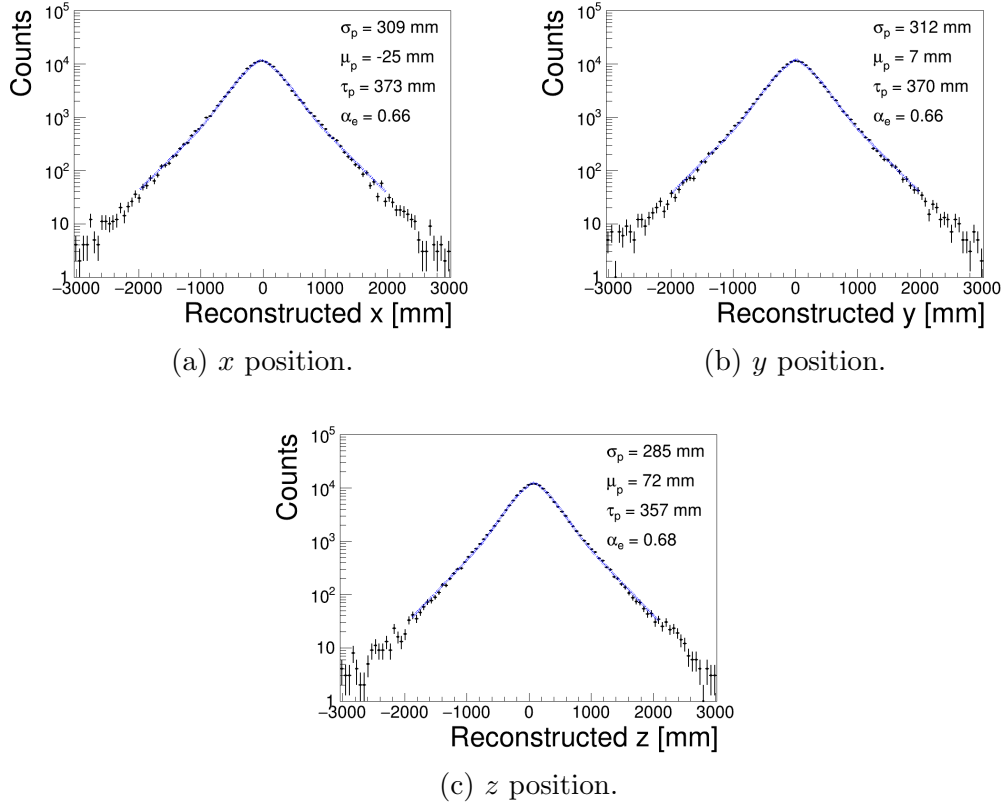


Figure 7.7: Reconstructed position of the  $\gamma$  rays from measurements taken with the  $^{16}\text{N}$  source at the centre of the SNO+ detector.

Figures 7.7 and 7.8 compare the reconstructed positions of the data collected with the  $^{16}\text{N}$  and AmBe sources respectively. A fit to the data was performed to extract the resolution of each coordinate. The functional form consisted of a Gaussian with exponential tails [148]:

$$N(x) = N_{\text{total}} \left( \frac{1 - \alpha_e}{\sqrt{2\pi}\sigma_x} e^{-\frac{1}{2}\left(\frac{x-\mu_x}{\sigma_x}\right)^2} + \frac{\alpha_e}{2\tau_x} e^{\frac{-|x-\mu_x|}{\tau_x}} \right) \quad (7.5)$$

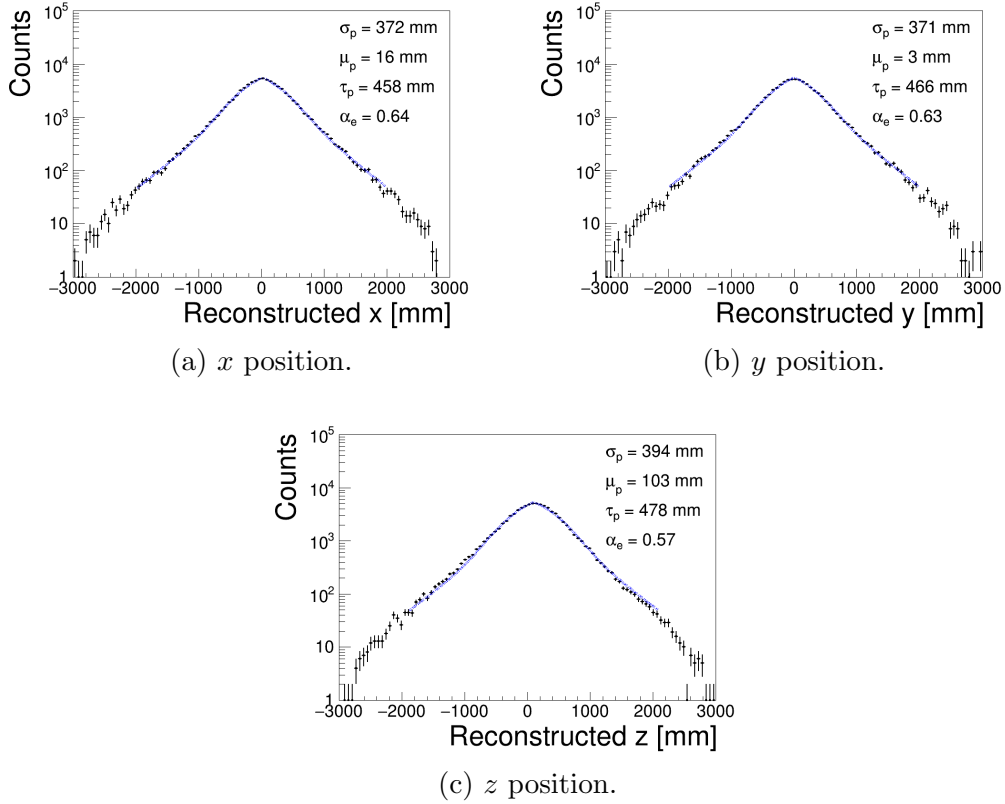


Figure 7.8: Reconstructed position of the 4.4 MeV  $\gamma$  ray from measurements taken with the AmBe neutron source at the centre of the SNO+ detector.

where:

- $N(x)$  is the number of counts in the corresponding bin at coordinate  $x$ .
- $N_{\text{total}}$  is the total number of counts in data set.
- $\sigma_x$  is the standard deviation of the Gaussian component, and is referred to as the resolution.
- $\mu_x$  is the shift of the centre of the Gaussian in the given coordinate.
- $\tau_x$  is the slope of the exponential component.
- $\alpha_e$  is the relative contribution of the exponential component.

As the total number of measured entries is known, the overall normalization  $N_{\text{total}}$  was fixed to that value. The resolutions obtained are compared in Table 7.3.

	<b>AmBe Source</b>	<b><math>^{16}\text{N}</math> Source</b>	<b>Difference</b>
x Resolution ( $\sigma_x$ ) [mm]	372	309	63 (17%)
y Resolution ( $\sigma_y$ ) [mm]	371	312	59 (16%)
z Resolution ( $\sigma_z$ ) [mm]	394	285	109 (28%)

Table 7.3: Position resolutions obtained from fits to the AmBe and  $^{16}\text{N}$  source data.

Given the higher energy of the  $\gamma$  rays produced by the  $^{16}\text{N}$  source, the subsequent  $e^-$  will produce signals that more closely resemble those of  $e^+$  from IBD. This is a result of the high energy  $e^-$  produced from Compton scattering of the initial  $\gamma$  ray. For 4.4 MeV  $\gamma$  rays, this produces  $e^-$  with continuous energies up to a maximum of 4.2 MeV, whereas for 6.1 MeV  $\gamma$  rays, the  $e^-$  energies extend up to 5.9 MeV. As the majority of the Cherenkov light is produced from the initial travel of charged particles, the  $e^-$  from the  $^{16}\text{N}$  source more closely match the 4 – 5 MeV  $e^+$  from IBD.

To evaluate the effects of position resolution, the reconstructed position of each  $\gamma$  ray–neutron pair in the AmBe source data was modified. This was done by randomly selecting a new reconstructed position for the first event in each coincidence pair. New  $x$ ,  $y$ , and  $z$  positions were chosen based on the resolution functions in Figures 7.7 and 7.8, sampled within radii of 3000 mm. To first evaluate the validity of this method, the positions of the first event were chosen based on the reconstructed 4.4 MeV  $\gamma$  rays. The resulting position difference distribution is compared to the original distribution in the data set in Figure 7.9.

The fraction of events that survive the position difference cut for the resampled data differs from the original data by 0.46%. The agreement here supports the assumption that the distance between events is mainly driven by the position resolution.

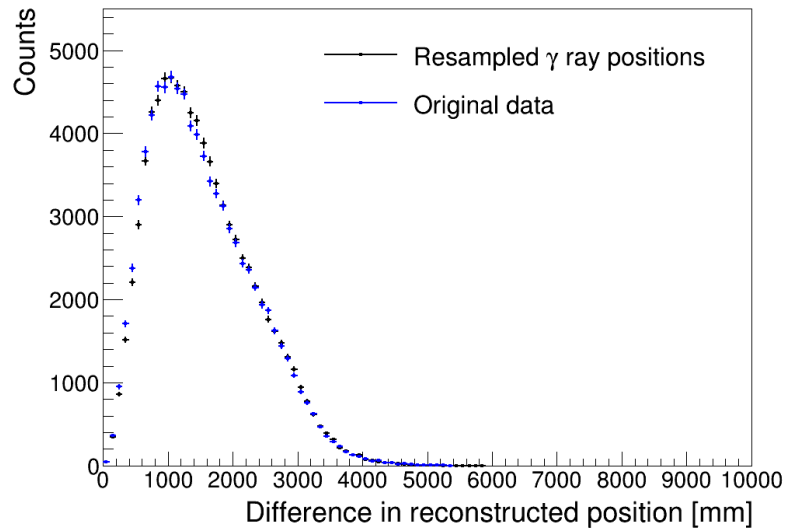


Figure 7.9: Position difference between event pairs for the original data and the data with resampled 4.4 MeV  $\gamma$  ray positions.

The same procedure was repeated using the resolutions obtained from the  $^{16}\text{N}$  source in Figure 7.7. The resulting distribution is compared to the original in Figure 7.10.

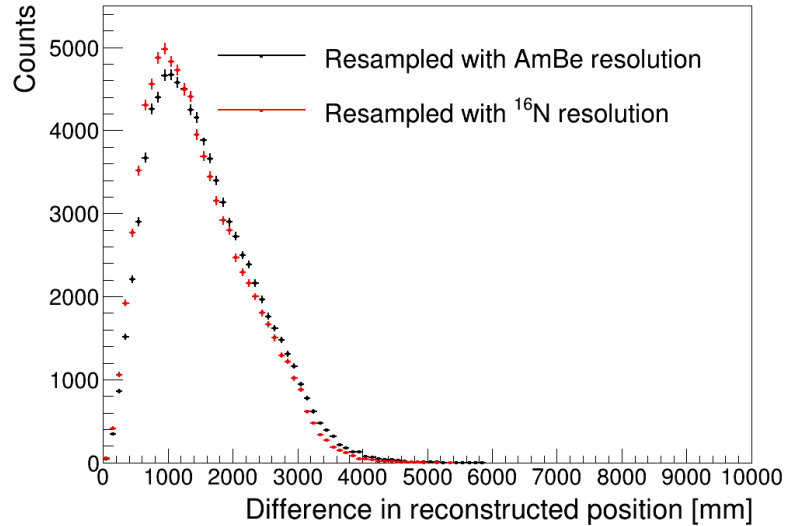


Figure 7.10: Position difference between event pairs for data with resampled first event positions based on 4.4 MeV  $\gamma$  ray and  $^{16}\text{N}$   $\gamma$  ray resolutions.

The improved position resolution of the  $^{16}\text{N}$  results in a slightly narrower distribution. For the optimal cut value of 1250 mm, the fraction of events that survive differs by 10.8%. This difference is assigned as a systematic uncertainty to the neutron tagging efficiency.

## Neutron Lifetime

The neutron lifetime determines the fraction of event pairs that lie in the chosen coincidence window. Both the  $e^+$  and the 4.4 MeV  $\gamma$  rays from the AmBe source produce light  $< O(\text{ns})$  after emission. As the second particle for both is the same, the measured neutron lifetime should be identical for the AmBe source coincidences and the IBD events. In this case, no further systematic effect would occur. However, there is some additional uncertainty on this measured value that needs to be evaluated.

To complete the evaluation of this parameter, the neutron lifetime was determined from the Monte Carlo simulation of the AmBe source, shown in Figure 7.11. Performing a single exponential fit, as in Section 5.2.1, the neutron lifetime was determined to be  $202.53 \pm 0.75 \mu\text{s}$ . A summary of all the determined values is shown in Table 7.4, along with literature values.

Source	Neutron Lifetime [ $\mu\text{s}$ ]
Measurement with AmBe source	$208.1 \pm 1.2$
Simulated AmBe source measurement	$202.53 \pm 0.75$
Simulated inverse beta decay	$202.02 \pm 0.87$
Cokinos and Melkonian [92]	$204.7 \pm 0.4$
Zhang et al. [93]	$202.6 \pm 3.7$

Table 7.4: Mean neutron lifetimes as determined from various sources.

The simulation performed for IBD and for the central AmBe source measurement are entirely compatible. This suggests that the source of neutrons does not affect the lifetime. This is to be expected as the majority of the travel time of the neutrons will take place after it has thermalized ( $< 1 \text{ eV}$  of energy). This indicates that even though the energies of the neutrons differ

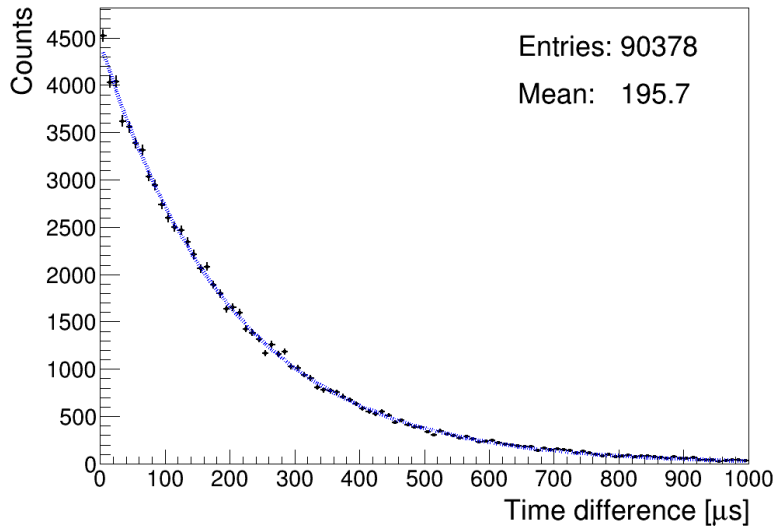


Figure 7.11: Time difference between 4.4 MeV  $\gamma$  ray–neutron pairs for the simulated AmBe source measurement.

initially ( $O(MeV)$  for the AmBe source and  $O(100\text{ keV})$  for IBD), the AmBe source can be used to mimic the IBD signal in regards to time coincidences.

While the lifetime values are similar, there are some disagreements. Namely the measured neutron lifetime differs from the Monte Carlo simulation and to a lesser extent with the literature values. While the measured lifetime is likely the most correct for the case of measuring an antineutrino signal in this detector, the potential impact of this discrepancy needs to be taken into account. This impact was evaluated by looking at the difference this causes in regards to the fraction of signal event kept  $\epsilon_{\Delta t}$  for the time cut of 275  $\mu\text{s}$ . Although the measured and simulated lifetimes differ by 2.7%, this causes  $\epsilon_{\Delta t}$  to change by 1.3%. This small difference is included as an added uncertainty on the neutron tagging efficiency.

### $\gamma$ ray Trigger Efficiency

The final systematic to evaluate comes from the conversion of  $\epsilon_{\gamma-n}$  into  $\epsilon_{\text{neutron}}$ . This relies on accurate knowledge of the trigger efficiency of the 4.4 MeV  $\gamma$  ray

$\epsilon_\gamma$ , a parameter that was determined from Monte Carlo simulations of the AmBe source. It is known that the Monte Carlo simulation has difficulty modeling this triggering close to the detection threshold.

The lowest detector trigger threshold is set at a nominal value of 7 nHit. The Monte Carlo simulation was set to trigger the detector 100% of the time when this criteria was met and 0% otherwise. This produces a step function-shaped trigger efficiency. However, from measurements, it is known that the SNO+ detector will always trigger only when 10 or more PMTs detect a photon simultaneously [149]. Between 5-9 nHit, the trigger efficiency changes continuously. This comparison is shown in Figure 7.12.

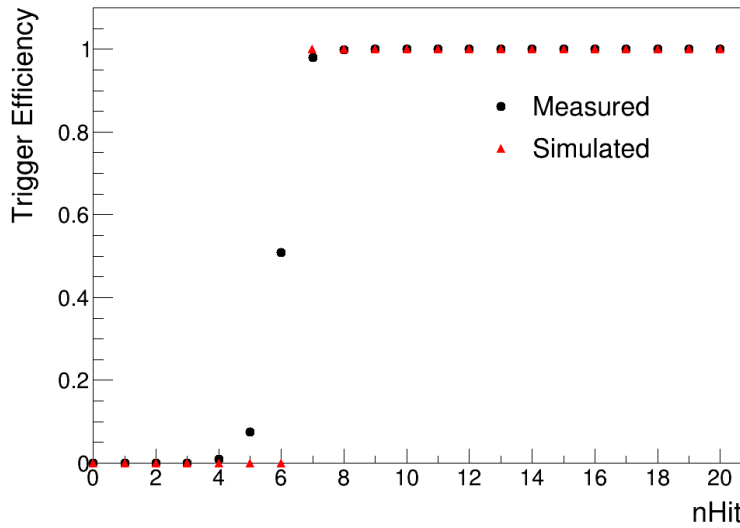


Figure 7.12: Measured trigger efficiency as a function of nHit compared to the modeled trigger efficiency.

The Monte Carlo generated nHit distribution of the 4.4 MeV  $\gamma$  ray, previously shown in Figure 7.4, illustrates that very few of the events have  $< 10$  nHit. Applying the measured trigger efficiency to the nHit distribution for events below 10 nHit resulted in a 0.03% difference in the total number of triggered  $\gamma$  rays. This difference is considered negligible compared to the other evaluated systematics.

## 7.2 $e^+$ Detection Efficiency

This efficiency was determined through the reactor Monte Carlo simulation by looking at the fraction of  $e^+$  that trigger the detector and also successfully reconstruct. However, as this pertains to the search for antineutrinos, this would also be affected by any nHit cuts used. As the cut in question is not yet set, this efficiency was determined as a function of the minimum nHit cut that may be placed on the  $e^+$ . Additionally, as the data collected by detector had a blinding scheme applied to it, the Monte Carlo simulation had the same scheme applied. The efficiency of detecting the positrons from IBD was determined based on this simulation.

Figure 7.13 shows the efficiency as a function of the minimum nHit cut. More accurately, this efficiency represents the fraction of the total IBD events where the  $e^+$  falls into a region defined by a minimum nHit up to maximum nHit of 39. The efficiency here corresponds to the value of  $\epsilon_{e^+}$ . Due to the blinding that was applied, it drops to zero at an nHit of 39. The amount of  $e^+$  signals that were removed because of this blinding for this analysis corresponds to just 5.2% of the total IBD events that took place in the detector.

### Systematic Uncertainty: nHit Distribution Modeling

The search for antineutrinos only looks for the highest energy  $e^+$ . Events at these energies will have sufficiently high nHit that the detector will always trigger. Therefore, this efficiency is primarily a measure of the fraction of events from these  $e^+$  that lie in the chosen nHit region. The main systematic occurs because of the uncertainty on how well the Monte Carlo simulation models the nHit associated to a given event.

To evaluate this, the data from the  $^{16}\text{N}$  source was used again as this source most closely resembles the  $e^+$  from IBD. Figure 7.14 shows the measured nHit distribution of the  $^{16}\text{N}$  source when placed at the centre of the detector com-

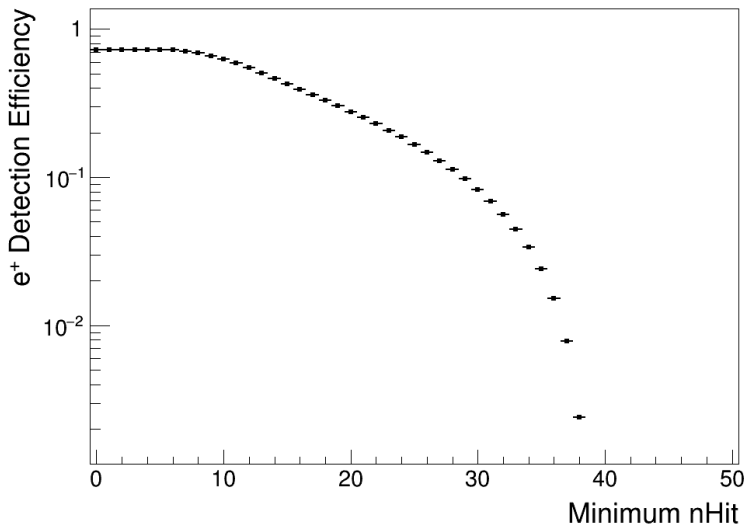


Figure 7.13: Fraction of the total IBD events where the  $e^+$  falls into a region defined by a minimum nHit up to a maximum nHit of 39.

pared to that obtained from the simulation. A slight difference can be seen, where the mean of the simulated distribution is slightly lower than that of the measurement. While this disagreement is present in the version of the SNO+ detector simulation that was used for this antineutrino analysis, the most recent versions of the simulation show good agreement in these distributions. Unfortunately, due to the computational time required to repeat the simulations, these improved versions could not be used instead for this work.

Previously in Figure 5.7c, it was found that the nHit of an event has a slight correlation to the radius at which it occurs. Therefore, this evaluation was performed for varying radial positions. A subset of ten runs were analyzed where the  $^{16}\text{N}$  source was placed at different positions within the detector. Figure 7.15 shows how the mean of these nHit distributions vary as a function of radius for both data and simulation. Similarly to Figure 5.7c, the mean nHit is seen to increase as events take place closer to the edge of the detector.

To estimate the effects on the  $e^+$  efficiency by comparing simulation and data, the same integral over a region of interest (ROI) was performed. The

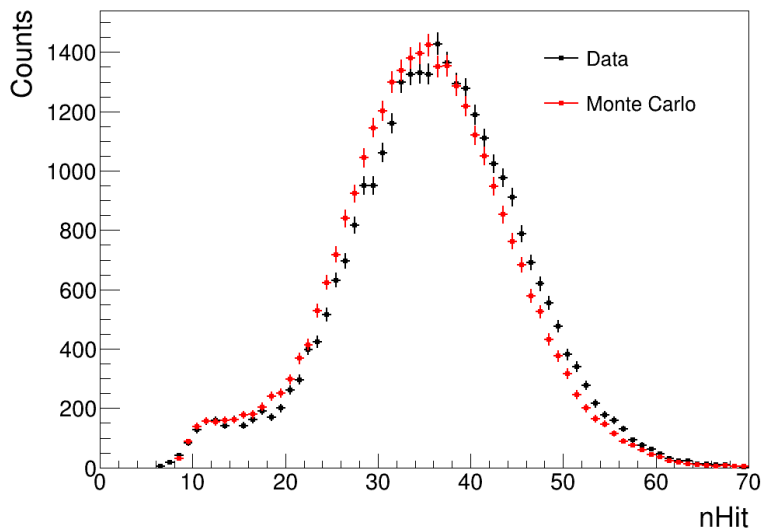


Figure 7.14: nHit distribution from measurements with the  $^{16}\text{N}$  source at the centre of the detector compared to the corresponding Monte Carlo simulation.

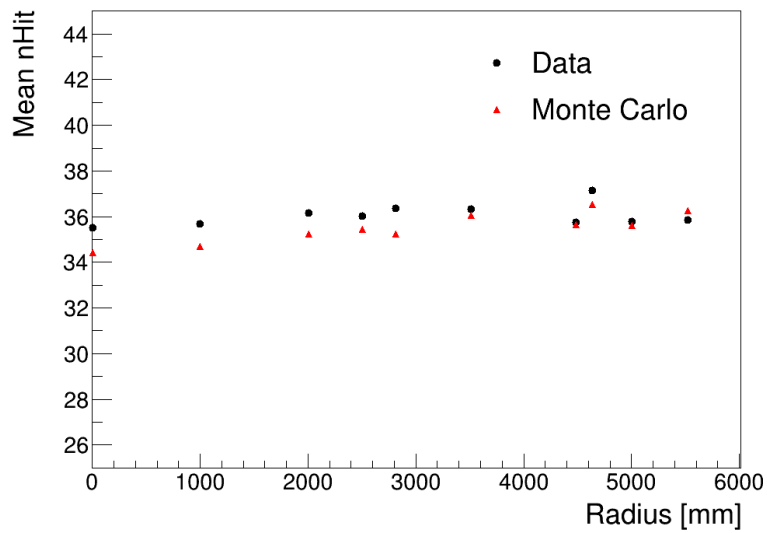


Figure 7.15: Mean of the  $^{16}\text{N}$  nHit distribution from detector-collected data and corresponding Monte Carlo simulations at different radii within the detector.

ROI was defined by a minimum nHit of 29, for reasons to be established later in Section 8.4.1, to a maximum of 39. This was compared to the total integral to determine the fraction that fall within this ROI. Figure 7.16 shows the fractional difference between this integral for detector data and the corresponding simulations.

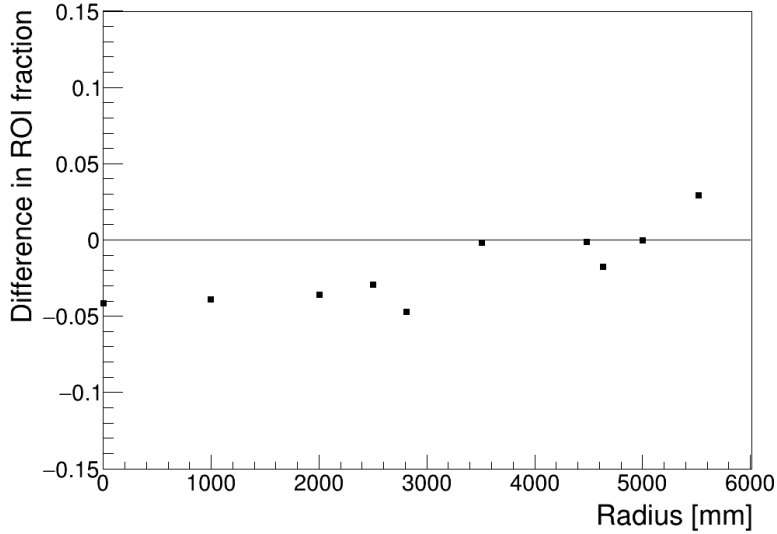


Figure 7.16: Difference between the fraction of events that fall within an nHit ROI of [29,39] for detector-collected data and simulations with the  $^{16}\text{N}$  source placed at different radii within the detector.

These differences between the data and simulation, while small, are not negligible. The absolute mean difference in Figure 7.16 was found to be 2.5%. This was assigned as the uncertainty on  $\epsilon_{e^+}$  and is associated with the accuracy of the Monte Carlo simulation in modeling a high energy event's nHit.

### 7.3 Fiducial Volume Efficiency

The final information needed to determine the expected number of measured IBD events is the fraction where both events are located within the fiducial volume. More specifically this is constructed as the fraction of the total IBD

interactions that occur within the central water volume. This allows for the determination of an expected rate based on the previous estimate in Section 3.4.2.

IBD interactions occur uniformly within the water. As the two events (from the  $e^+$  and neutron) are spatially correlated, the reactor Monte Carlo simulation must be used to make this determination. From the simulation, the fraction of IBD events where both reconstruct to positions within the specified 5000 mm diameter fiducial volume is  $0.3670 \pm 0.0027$ .

### Systematic Uncertainty: Reconstruction Resolution

This efficiency was solely determined by looking at the reconstructed positions of each event in a coincident pair. The previously discussed uncertainty on the position reconstruction of the  $e^+$  was evaluated to see any potential impact. This was done in a similar manner as in Section 7.1.3. This also required the position resolution of the neutrons, shown in Figure 7.17. The neutron reconstructions also include further broadening that comes from travel of the neutron through the water.

To estimate the effect of a difference in the  $e^+$  reconstructed position on this efficiency, the simulated interaction points were taken and reconstructed  $e^+$  positions in  $x$ ,  $y$ , and  $z$  were randomly sampled individually for each coordinate, based on the resolutions in Figure 7.8. Similarly, the reconstructed neutron positions were sampled from the resolutions in Figure 7.17.

The same procedure was then repeated using the resolutions obtained from the  $^{16}\text{N}$  source, Figure 7.7. Comparing the fraction of event pairs where both are located within a 5000 mm diameter fiducial volume, resulted in a 0.51% difference. The effect that position resolution has on this efficiency is expected to be small. At large radii, assuming the same set of neutron interaction positions, a poorer resolution will distribute nearly as many events outside of the fiducial volume as it would inside. This small difference is assigned as an uncertainty on this efficiency.

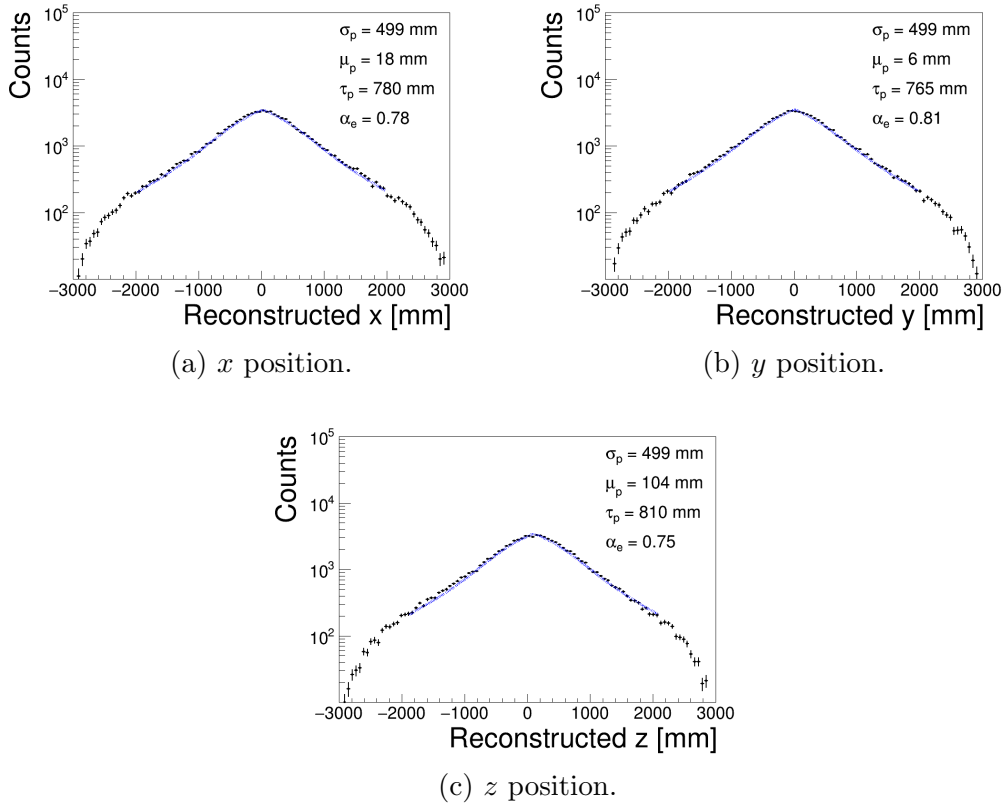


Figure 7.17: Reconstructed positions of neutrons from measurements taken with the AmBe source in the centre of the SNO+ detector.

## 7.4 Summary and Expectation

Each individual component that affects the number of antineutrinos that can be detected was evaluated. Table 7.5 summarizes these results working towards a total efficiency and expectation. The efficiencies compound and begin with those that are uncontrollable within this analysis. The final column lists the expected rate of events. In a data set with a known duration, the antineutrino signal expectation can now be determined.

Some of the values listed in the table are estimates, used only to better illustrate the rate. The principal estimate here is the detector trigger efficiency of the  $e^+$ . This value and subsequent ones based on it have uncertainties omitted. The total efficiency (last entry in Table 7.5), determined by Equation 7.1,

	<b>Fraction remaining</b>	<b>Expected rate [events/year]</b>
Total IBD events	–	$114.8 \pm 6.4$
With triggered $e^+$	0.722	82.9
With triggered neutrons	$0.303 \pm 0.042$	$34.8 \pm 5.2$
With triggered $e^+$ and neutrons	0.219	25.1
Have $e^+$ nHit $\geq 29$	$0.0295 \pm 0.0042$	$3.39 \pm 0.52$
In 5000 mm fiducial volume	$0.0108 \pm 0.0015$	$1.24 \pm 0.19$
Survive time and distance cuts	$0.00359 \pm 0.00052$	$0.413 \pm 0.064$

Table 7.5: Summary of the efficiencies in detecting signal events and the rate expectations for the SNO+ detector.

is fully characterized and includes all systematic uncertainties.

For an IBD interaction to be stored in a collected data set, the detector must trigger on both the  $e^+$  and neutron event. Table 7.5 first shows that 25 events per year will pass this minimal condition. With these statistics, only the highest energy  $e^+$  can be distinguished from backgrounds. Restricting the analysis to only the high energy  $e^+$  (those with nHit  $\geq 29$ , again for reasons to be discussed) reduces the number of signal events to just 3.4 per year. This occurs as most of the  $e^+$  from IBD have lower energies. Applying the remainder of the selection criteria reduces this to 0.4 events per year. In the absence of years of data taking, the signal expectation in the data set is near zero.

# Chapter 8

## Searching for Antineutrinos in SNO+ Data

### 8.1 Detector Data Overview

The search for antineutrinos was performed over the blinded data collected by the detector during the period from September 1, 2018 to March 31, 2018. Each individual run (typically one hour long) was evaluated by the SNO+ run selection committee. If the run passed the specified data quality conditions, it was labeled as ‘golden’ and is used for analysis [150]. A total of 1782 golden runs were analyzed (listed in Appendix C). This set of runs is referred to as the “full” data set in regards to this analysis.

#### 8.1.1 Data Processing Details

Prior to the search algorithm being applied, each run was further processed. Due to the immense computational requirements, this was performed using Compute Canada’s supercomputing clusters and in multiple steps:

- The data files for these runs were downloaded in ROOT format, corresponding to a file size of 7.4 terabytes.

- Initial selections were applied to these data files. Only events that triggered the detector on any of the enabled physics-based triggers (N100Lo, N100Med, N20, N20Low, ESUMHi) were kept in the data set.
- The “analysis\\_mask”, defining the data cleaning cuts, was then applied onto this data. This set of cuts (listed in Appendix B) removes any events from instrumental backgrounds, muons, or muon followers.
- All remaining events were reconstructed using the “alberta” position and direction reconstruction algorithms [78].

Events that pass these trigger and data cleaning conditions constitute the remaining data set. This data set now had a total file size of 4.0 terabytes. This necessary procedure of removing instrumental events from the detector data sets (through trigger selection and data cleaning) was also performed identically for the simulations (Chapters 5, 6, and 7) and calibration data (Chapters 6, and 7). This ensures the that no data was treated in a biased way as compared to other data.

### 8.1.2 Live Time

The total live time of the remaining data set was determined using the “Live Time Calculator” [140]. The majority of the dead time in any given run comes from 3 main sources:

- **Muons** — Muons and events following within 20 s of a muon in the detector are removed. This is used to remove the potential background introduced by muon follower events [151].
- **Calibrations** — Each run has a period of a few minutes over which electronic calibrations are performed. Events that overlap calibration pulses are removed from the data set.

- **Event bursts** — Instrumental events that cause burst of events (for example, “flashers”, see Appendix B) introduce extra dead time as the detector is locked out for a period of time following each event.

Afterwards, the live time of the remaining data set was determined to be 69.7 days.

## 8.2 Search Results

This data set was searched using the first pass of the algorithm (Section 5.3.1), producing a subset of coincident event pairs. These event pairs had a time difference of  $< 1000 \mu\text{s}$  and had both events reconstruct within the central water volume of the detector. This subset consisted of 96 million event pairs and reduced the total file size to 44 gigabytes.

Lastly, the second pass of the search algorithm was performed on this subset of data. This step removed any events that did not pass the further selection criteria of:

- Time difference of  $< 275 \mu\text{s}$  between events in the pair.
- Reconstructed radius of  $< 5000 \text{ mm}$  for both events in the pair.
- Position difference of  $< 1250 \text{ mm}$  between events in the pair.

Afterwards, the remaining data consisted of 0.13 million event pairs. The nHit distribution of these event pairs is shown in Figure 8.1.

### 8.2.1 Background Considerations

The distribution here resembles the ones shown previously in Figure 5.14, giving a first indication that these events are from accidental backgrounds. Another evaluation was done to further support this statement. In the case of accidental

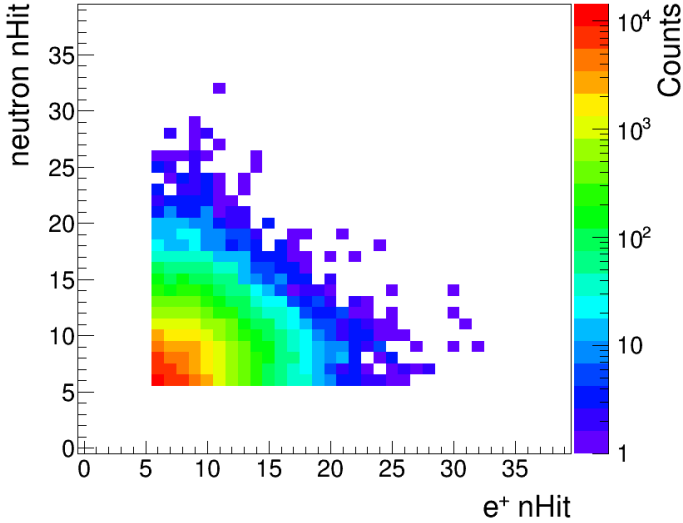


Figure 8.1: nHit distribution of all event pairs that passed the selection cuts in 69.7 live days of detector data.

backgrounds, where two uncorrelated events are coincident in time, it is equally likely to have a high energy first event followed by a low energy second event as the reverse. This is not always the case for IBD events, where sometimes there are some high energy events followed by low energy events, but not the reverse.

For a ROI defined by a minimum  $e^+$  nHit condition, an identical region can instead be constructed with a matching minimum neutron nHit. These regions (for the example of an nHit value of 25) are illustrated in Figure 8.2. In the case of a purely accidental background, the number of events in each of these two regions is expected to be the same.

The number of events in each region was determined for a series of different minimum nHit values. The ratio of these values is plotted in Figure 8.3. For purely accidental backgrounds this ratio is expected to be 1.0.

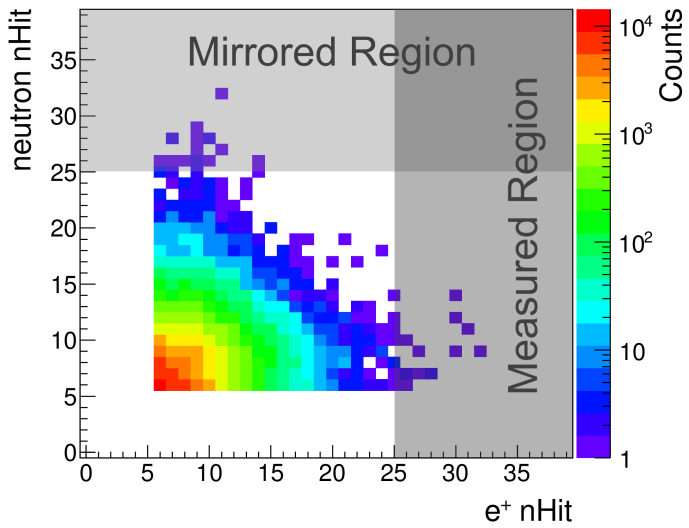


Figure 8.2: Illustration of the “measured” and “mirrored” regions of the nHit distribution of coincidence pairs.

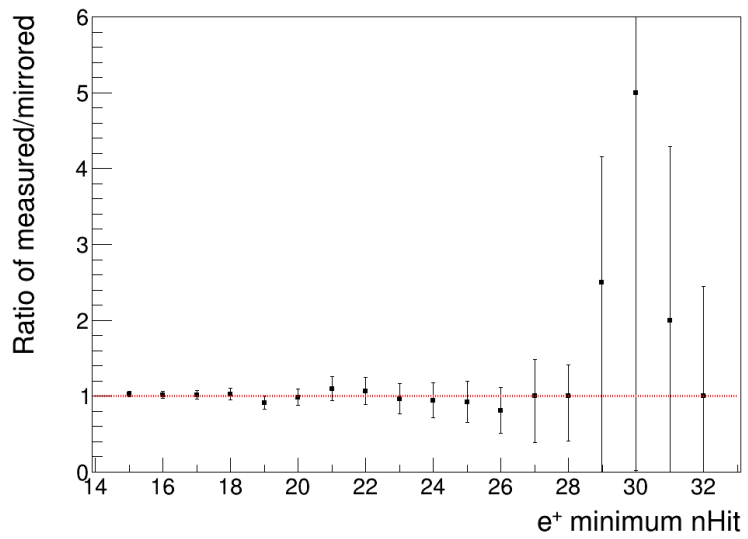


Figure 8.3: Ratio of the number of events in the “measured” and “mirrored” regions as a function of the minimum nHit cut that defines the corresponding region. The expectation for purely accidental backgrounds is shown in red.

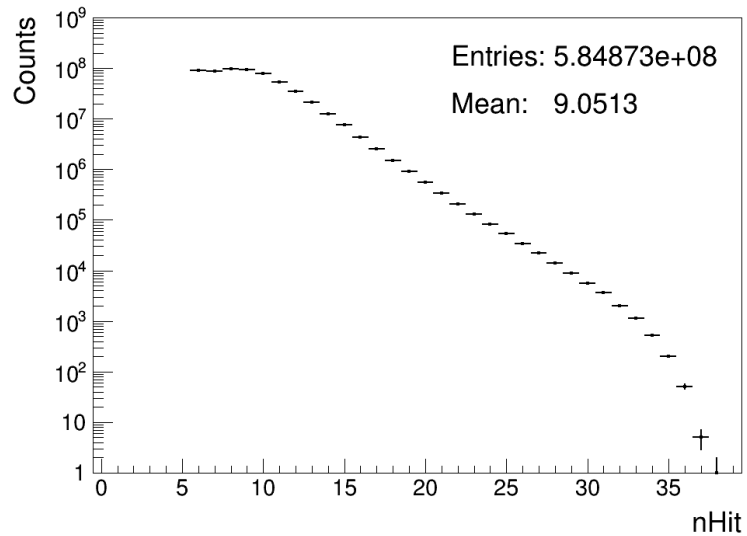
## 8.3 Background Expectation

Following the evidence that the collected data results from accidental backgrounds, the toy Monte Carlo simulation was used to estimate their rate. The accidental background rate (i.e. the rate at which events are coincident within some time interval) can be determined from the overall rate of events. However, studies from Lozza [152] have shown that this overall rate has been changing dramatically over time. These changes manifest themselves as spikes in the event rate when water was recirculated in and outside of the detector.

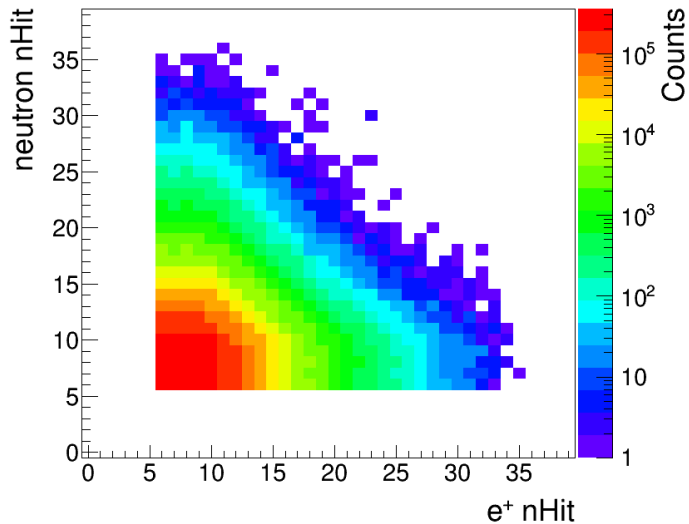
This challenge was avoided by looking at the total number of coincidence event pairs in the full data set (as this value is known). This number contains the time-averaged overall background rate over the multi-month data taking period. The background Monte Carlo model was then used to determine what fraction of event pairs pass all of the cuts to contribute to the two-dimensional nHit distribution.

At high nHit in Figure 8.1, the statistics are very low. To make a good estimate of the expected background rate in this region, a large Monte Carlo sample size is required. The background simulation was repeated, generating 10 billion coincident event pairs. This provided a statistical factor of 10<sup>4</sup> compared to detector data. Figure 8.4a shows the one-dimensional nHit distribution on which the Monte Carlo sampling was based along with the resulting two-dimensional distribution after all cuts were applied.

This time, the Monte Carlo sampling was based on the distributions from the full data set rather than the 2.6 day subset that was previously used in Chapter 5. This ensures that the results are more representative of the data collected by the detector over the multi-month time period. To illustrate the variation, the rate of events that contribute to Figure 8.1 was determined for both the 69.7 live day and 2.6 live day data sets. These rates were 21.2 and 19.2 mHz respectively. This is expected as the 2.6 day period in September had a sta-



(a) All events in full data set.



(b) Background Monte Carlo.

Figure 8.4: nHit distribution of all events in the 69.7 days of data (a) on which the background Monte Carlo simulation generated the corresponding two-dimensional distribution (b).

ble low background rate, whereas the multi-month time period included data collected during water recirculation (where the background rate was elevated).

From Figure 8.4b, the number of expected background events for the measurement period was determined. Focusing in on the high-nHit region, this was determined again as a function of the minimum  $e^+$  nHit cut. The number of expected background events are listed along with the number measured by the detector in Table 8.1.

Minimum $e^+$ nHit	Expected	Measured
25	24.93	22
26	15.75	13
27	9.91	9
28	6.20	7
29	3.86	5
30	2.44	5
31	1.44	2
32	0.72	1
33	0.30	0

Table 8.1: Number of expected background event pairs vs. number of measured event pairs for different values of a minimum  $e^+$  nHit cut.

## 8.4 Confidence Interval

The upper limit at 90 % confidence was determined following the method prescribed by Feldman and Cousins [153]. Prior to doing so, the minimum nHit cut on the  $e^+$  event needed to be set to fully define the ROI.

### 8.4.1 Final Region of Interest

The final ROI was set by performing an optimization of the minimum  $e^+$  nHit cut. First, the sensitivity of the experiment was determined as a function of this cut. The sensitivity is defined as the average upper limit  $\langle UL_{90} \rangle$  that would be obtained for an experiment that has  $b$  expected backgrounds. Using

the sensitivity here avoids the problem of choosing the best limit due to an under-fluctuation in the measured data.

For each nHit value, the expectation  $b$  was taken from Table 8.1. The determined  $\langle \text{UL}_{90} \rangle$ , seen in Figure 8.5a, decreases with higher nHit values, indicating a better limit. The changing signal efficiency was also evaluated as the desired quantity is a limit on the antineutrino flux, where it scales as  $\frac{\langle \text{UL}_{90} \rangle}{\epsilon_{\text{neutron}} \epsilon_{\text{FV}} \epsilon_{e^+}}$ . The only component of the signal efficiency that changes with this varying nHit cut is the  $e^+$  detection efficiency  $\epsilon_{e^+}$ , also shown in Figure 8.5a.  $\epsilon_{\text{neutron}}$  and  $\epsilon_{\text{FV}}$  do not change by varying this nHit. It is then sufficient to look at how  $\frac{\langle \text{UL}_{90} \rangle}{\epsilon_{e^+}}$  changes to determine the nHit region that produces the best limit on the antineutrino flux.

Figure 8.5b shows how  $\frac{\langle \text{UL}_{90} \rangle}{\epsilon_{e^+}}$  changes as function of the nHit region used. The clear minimum corresponds to an nHit region bounded with a minimum value of 29. This final condition was set to require a  $e^+$  nHit  $\geq 29$ .

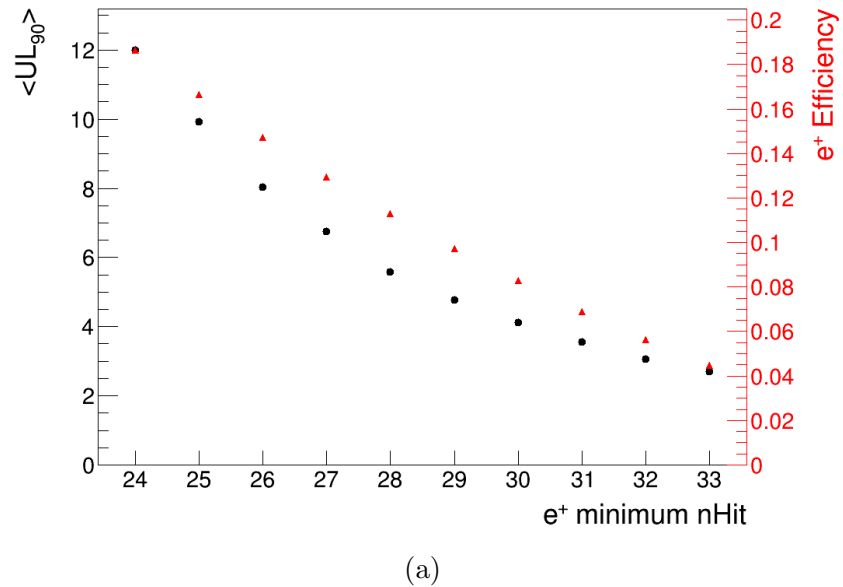
### 8.4.2 Limit on Number of Events

In this ROI, there were a total of 5 events in the detector data. The expectation determined from the Monte Carlo simulation was 3.86 background events. The expected signal in this data set is negligible at 0.079 events. This corresponds to a confidence interval of [0, 6.13], where the signal is less than 6.13 events at 90% confidence.

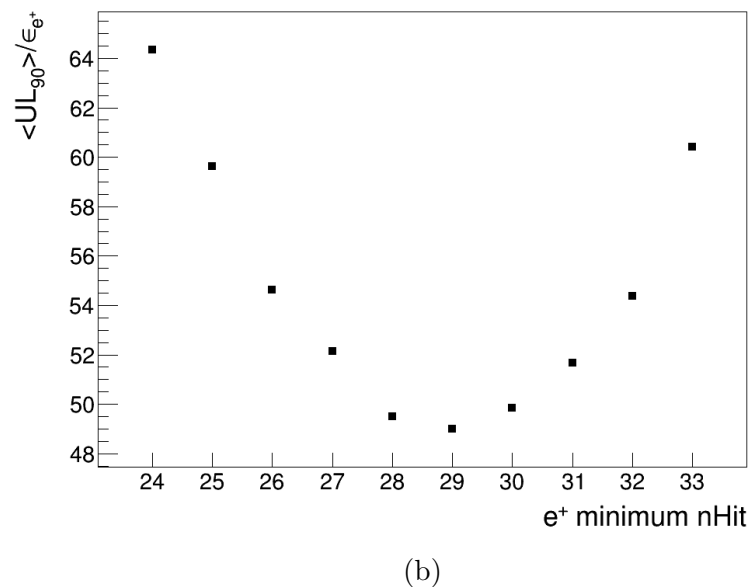
## 8.5 Antineutrino Limit

### 8.5.1 Antineutrino Flux

The upper limit on the number of signal events was converted into a better physical quantity: a limit on the flux of antineutrinos passing through the SNO+ detector. The corresponding limit on the rate of inverse beta decay



(a)



(b)

Figure 8.5: Sensitivity as a function of the minimum nHit cut value alongside the corresponding efficiency of detecting the  $e^+$  from IBD (a). Sensitivity over efficiency (b) corresponds to the obtainable limit on the antineutrino flux.

reactions  $R_{\text{up}}$  was determined by:

$$R_{\text{up}} = \frac{S_{\text{up}}}{\epsilon t} \quad (8.1)$$

with  $\epsilon$  being the total efficiency of detecting an IBD reaction and  $t$  the live time of the experiment. Performing this calculation yielded an upper limit on the rate of IBD interactions of  $0.283 \pm 0.041$  mHz. The interaction rate  $R$  can be related to the flux  $\Phi_{\bar{\nu}_e}$  by:

$$R = n_p \int \Phi_{\bar{\nu}_e}(E) \sigma(E) dE \quad (8.2)$$

where  $n_p$  represents the number of targets (i.e. protons) in the experiment. The energy dependent cross-section  $\sigma_p(E)$  is known and was previously used in the determination of the annual IBD expectations for the SNO+ detector, Section 3.4.2. To convert  $R_{\text{up}}$  into the corresponding total flux  $\Phi_{\bar{\nu}_{e-\text{up}}}$ , assumptions were made on the shape of the flux spectrum as a function of energy.

The shape of the flux spectrum is complicated as it takes into account the contributions from hundreds of reactors around the world. The type, power, and distance of each of these reactors is needed to construct  $\Phi_{\bar{\nu}_e}(E)$ . The simplest, and most physically relevant, assumption to make is that the shape of the spectrum is identical to the one that is expected (and previously calculated). In this circumstance, the limit on the antineutrino flux can be determined as:

$$\Phi_{\bar{\nu}_{e-\text{up}}} = \frac{R_{\text{up}}}{R_{\text{SNO+}}} \Phi_{\bar{\nu}_{e-\text{SNO+}}} \quad (8.3)$$

where  $R_{\text{SNO+}}$  is the rate of IBD events expected in the SNO+ detector and  $\Phi_{\bar{\nu}_{e-\text{SNO+}}}$  the total flux that corresponds to that rate. Performing these calculations, the limit of 6.13 signal events becomes an antineutrino flux of  $(1.45 \pm 0.23) \times 10^7 \bar{\nu}/(\text{cm}^2 \text{s})$ . More specifically, this is the upper limit on the number of antineutrinos from reactors that can be passing through the SNO+ detector per

unit time. From the reactor calculations, the expected flux that was passing through the SNO+ detector during this time period is  $(1.87 \pm 0.12) \times 10^5 \bar{\nu}/(\text{cm}^2 \text{s})$ .

### Flux to Distance Estimate

To better conceptualize the magnitude of this upper limit on the antineutrino flux, a further series of calculations were performed. These were aimed at determining how close a nuclear reactor would have to be to the SNO+ detector to obtain the given flux. This evaluation looked at the inclusion of a pressurized water reactor (PWR) with a thermal power of 6 GW (a typical total power for a reactor complex).

The calculations described in 3.4.2 were repeated for all currently-operating reactors along with the additional hypothetical reactor. The distance of the hypothetical reactor from the SNO+ detector was varied. From the total flux obtained, neutrino oscillations were then taken into account to ensure that this flux corresponds to that from Section 8.5.1.

The antineutrino flux of  $(1.45 \pm 0.23) \times 10^7 \bar{\nu}/(\text{cm}^2 \text{s})$  was found to correspond to the case where the additional 6 GW nuclear reactor was located 10 km away from the SNO+ detector. This distance is noticeably less than the actual distances to the closest nuclear reactors,  $O(100 \text{ km})$ . Comparing this to the dedicated reactor antineutrino experiments, it is, however, several times larger than the farthest reactors near the Daya Bay (2.0 km) [102], RENO (1.4 km) [103], and Double CHOOZ (1.0 km) [104] experiments.

### 8.5.2 Flux Uncertainty

Determining this flux in this way relies on the knowledge of the expected antineutrino flux passing through the SNO+ detector. Previously mentioned in Section 3.4.2, this is determined from the data provided by the IAEA's PRIS database. The data used to determine the flux expectations included operat-

ing thermal powers and annual-averaged load factors for the year 2017. The conversion from a limit on the event rate to an antineutrino flux makes the assumption that the time-averaged thermal power produced by these reactors was the same over the multi-month data-taking period as it was over the year.

This assumption may not be true. For example, a given reactor may have shut down for a period of time, influencing the annual load factor, but potentially not impacting the flux during the SNO+ data-taking period (if the shutdown occurred outside of this period). This effect can be evaluated for the three closest nuclear reactors. The Independent Electricity System Operator (IESO) publishes publicly available data for every power generating station in Ontario [154]. As the three closest reactors (Bruce, Darlington, and Pickering) are located within this province, the IESO provides hourly-averaged data on the actual produced electric power. The electric output of a reactor is directly related to its thermal output (the quantity on which neutrino flux calculations are made), where a typical reactor will produce roughly three times more thermal power than electric [155]. The electric and thermal load factors are usually assumed to be equivalent in neutrino flux calculations [34].

While the electric power output is not ideal, it will enable a determination on the uncertainty associated with using the IAEA's annual-averaged data. The hourly data from the IESO was first converted to a daily average power output and is shown in Figure 8.6. The three reactors are seen to fluctuate over the course of the year, where the larger changes are associated to a core being taken off-line/on-line. These data are then used to determine each reactor's annual-averaged electric power output. This is compared to the corresponding values as posted in the IAEA's PRIS database in Table 8.2. The IAEA electric powers  $P_e$  for each reactor are determined as the sum over  $n$  reactor cores:

$$P_e = \sum_{i=1}^n P_{\text{ref } i} * LF_i \quad (8.4)$$

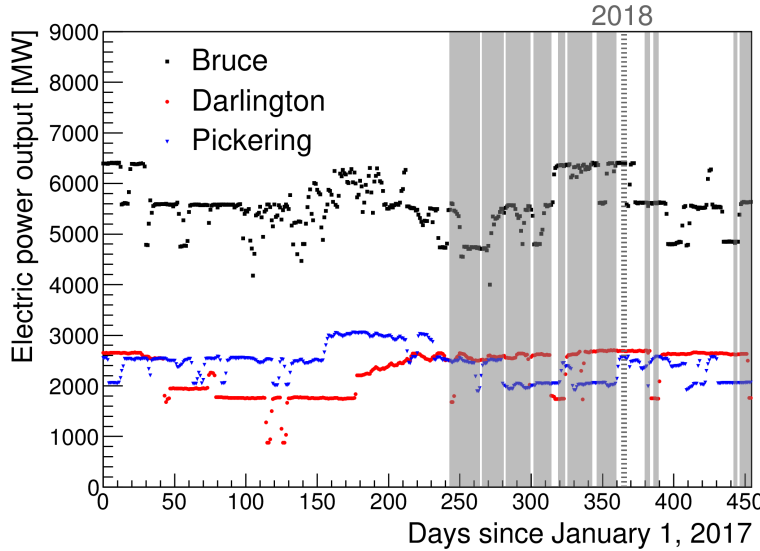


Figure 8.6: Daily-averaged IESO electric power outputs from [154] of the three closest nuclear reactors to the SNO+ detector. The shaded area corresponds to the SNO+ data-taking period of the 69.7 live day data set.

where  $P_{\text{ref } i}$  and  $LF_i$  are the reference electric power and load factor for the  $i^{\text{th}}$  reactor core, respectively.

Reactor	Bruce	Darlington	Pickering
IESO Electric Power [MW]	5599	2234	2455
IAEA Electric Power [MW]	5595	2220	2455
Difference	0.07 %	0.6 %	0 %

Table 8.2: Comparison of annual-averaged nuclear reactor electric power outputs as reported by the IAEA and the IESO in 2017 for the three closest reactors to the SNO+ detector.

The annual-averaged powers based on the hourly electric power data from the IESO show excellent agreement with those from the IAEA. This also serves as a verification of the accuracy of the annual data posted by the IAEA. The IESO data is used to determine the average electric power output for each reactor over the period of SNO+ data-taking (shaded region in Figure 8.6). These average powers are compared to those from the IAEA in Table 8.3.

While the data for the Bruce reactor does not differ much, the Darlington and Pickering reactors are seen to have a  $> 10\%$  difference. In the flux

Reactor	Bruce	Darlington	Pickering
IESO Electric Power [MW] (averaged over data-taking period)	5505	2497	2192
IAEA Electric Power [MW] (averaged annually)	5595	2220	2455
Difference	-1.6 %	12.4 %	-10.7 %

Table 8.3: Comparison of annual-averaged nuclear reactor electric power outputs to those averaged over the SNO+ data-taking period of the 69.7 live day data set.

limit calculation from Equation 8.3, the powers for these three reactors are corrected using the average over the data-taking period when determining their contribution to  $\Phi_{\bar{\nu}_{e-\text{SNO+}}}$ .

The uncertainty associated to using the annual-averaged data to determine the antineutrino flux over this shorter data-taking period is estimated to be the mean difference (8.2%) of the three evaluated reactors. This uncertainty is included and assigned to the remaining reactors (contributing roughly 40% of the antineutrino flux).

# Chapter 9

## Conclusions

Performing a series of laboratory measurements and simulations resulted in a constraint on the number of antineutrinos from nuclear reactors that are passing through the SNO+ detector. The upper limit on this flux was found to be  $(1.45 \pm 0.23) \times 10^7 \bar{\nu}/(\text{cm}^2 \text{s})$ . During this work, a number of other significant accomplishments were achieved.

At the University of Alberta, a germanium detector was used to make measurements of a weak AmBe neutron source. An associated Monte Carlo simulation was developed that showed good agreement with the experimental measurements. From this work, the simulation was deemed appropriate for modeling the neutron interactions from IBD and also resulted in a first activity calibration of the AmBe source used.

Monte Carlo simulations of IBD in the SNO+ detector were then performed, allowing for the development of an algorithm to search for these events. A different simulation was concurrently developed to model accidental background within the detector. Through comparisons to a small subset of data collected by the SNO+ detector, the background to the antineutrino signal was shown to predominantly come from these accidental coincidences.

All parameters that governed the search algorithm were optimized to maximize the significance of a possible antineutrino signal. This required the use

of data collected with another AmBe source placed within the SNO+ detector, which allowed for an independent measurement of the mean neutron lifetime in water. Similarly, the evaluation of the systematic effects on measuring IBD events included the characterization of the  $\gamma$  ray to neutron ratio of this specific source. These evaluations also answered what unknowns are most likely to affect future antineutrino searches and require more exploration.

Lastly, the 69.7 live days of data collected by the SNO+ detector were in good agreement with the expectations set from the Monte Carlo simulation of purely accidental backgrounds. The antineutrino signal was unfortunately too small to be measurable in the water-filled SNO+ detector over this time period. However, given the proper circumstances, it is possible that a water Cherenkov detector could perform a measurement of antineutrinos on this timescale.

Looking forward, with the addition of liquid scintillator being imminent, this work lays the foundation for the antineutrino search in the future phases of the SNO+ experiment. The algorithms presented can be directly and immediately applied to this scintillator-filled detector data. In those phases, with an improved discrimination for the IBD signal, the SNO+ detector will soon begin performing measurements of antineutrinos. It will then start providing the much needed independent measurement of  $\Delta m_{21}^2$  and help resolve the associated tension in regards to neutrino oscillation.

# Bibliography

- [1] Pauli, W. (1930). Open letter to the group of radioactive people at the Gauverein meeting in Tübingen <http://microboone-docdb.fnal.gov/cgi-bin/RetrieveFile?docid=953;filename=pauli%20letter1930.pdf> (Accessed June 2018).
- [2] Cowan, C. L., Reines, F., Harrison, F. B., Kruse, H. W., and McGuire, A. D. (1956). Detection of the Free Neutrino: a Confirmation. *Science* 124(3212).
- [3] Davis, R. (1964). Solar Neutrinos. II. Experimental. *Physical Review Letters* 12(11):303–305.
- [4] Davis, R., Harmer, D. S., and Hoffman, K. C. (1968). Search for Neutrinos from the Sun. *Physical Review Letters* 20(21):1205–1209.
- [5] Bahcall, J. N. (1964). Solar Neutrinos. I. Theoretical. *Physical Review Letters* 12(11):300–302.
- [6] Anselmann, P., et al. (1992). Solar neutrinos observed by GALLEX at Gran Sasso. *Physics Letters B* 285(4):376–389.
- [7] Abazov, A. I., et al. (1991). Search for neutrinos from the Sun using the reaction  ${}^{71}\text{Ga}(\nu_e, e^-){}^{71}\text{Ge}$ . *Physical Review Letters* 67(24):3332–3335.

- [8] Fukuda, Y., et al. (1998). Measurements of the Solar Neutrino Flux from Super-Kamiokande's First 300 Days. *Physical Review Letters* 81(6):1158–1162.
- [9] Boger, J., et al. (2000). The Sudbury Neutrino Observatory. *Nuclear Instruments and Methods in Physics Research Section A* 449(1):172–207.
- [10] Ahmad, Q. R., et al. (2002). Direct Evidence for Neutrino Flavor Transformation from Neutral-Current Interactions in the Sudbury Neutrino Observatory. *Physical Review Letters* 89(1):011301.
- [11] Ahmad, Q. R., et al. (2001). Measurement of the Rate of  $\nu_e + d \rightarrow p + p + e^-$  Interactions Produced by  $^8B$  Solar Neutrinos at the Sudbury Neutrino Observatory. *Physical Review Letters* 87(7):71301.
- [12] Fukuda, Y., et al. (1998). Measurement of a small atmospheric  $\nu_\mu/\nu_e$  ratio. *Physics Letters B* 433(1):9–18.
- [13] Fukuda, Y., et al. (1998). Evidence for Oscillation of Atmospheric Neutrinos. *Physical Review Letters* 81(8):1562–1567.
- [14] Bilenky, S. (2016). Neutrino oscillations: From a historical perspective to the present status. *Nuclear Physics B* 908:2–13.
- [15] Araki, T., et al. (2005). Measurement of Neutrino Oscillation with KamLAND: Evidence of Spectral Distortion. *Physical Review Letters* 94(8):81801.
- [16] Adamson, P., et al. (2017). Measurement of the Neutrino Mixing Angle  $\theta_{23}$  in NOvA. *Physical Review Letters* 118(15):151802.
- [17] An, F. P., et al. (2017). Measurement of electron antineutrino oscillation based on 1230 days of operation of the Daya Bay experiment. *Physical Review D* 95(7):72006.

- [18] Abe, K., et al. (2015). Measurements of neutrino oscillation in appearance and disappearance channels by the T2K experiment with  $6.6 \times 10^{20}$  protons on target. *Physical Review D* 91(7):72010.
- [19] Abe, K., et al. (2011). Solar neutrino results in Super-Kamiokande-III. *Physical Review D* 83(5):52010.
- [20] The ALEPH Collaboration, et al. (2006). Precision electroweak measurements on the Z resonance. *Physics Reports* 427(5):257–454.
- [21] Mangano, G., et al. (2005). Relic neutrino decoupling including flavour oscillations. *Nuclear Physics B* 729(1):221–234.
- [22] Blasi, P. (2013). The origin of galactic cosmic rays. *The Astronomy and Astrophysics Review* 21(1):70.
- [23] Kajita, T. (2014). The Measurement of Neutrino Properties with Atmospheric Neutrinos. *Annual Review of Nuclear and Particle Science* 64(1):343–362.
- [24] Gaisser, T. K. and Honda, M. (2002). Flux of Atmospheric Neutrinos. *Annual Review of Nuclear and Particle Science* 52(1):153–199.
- [25] Kajita, T. (2010). Atmospheric neutrinos and discovery of neutrino oscillations. *Proceedings of the Japan Academy, Series B* 86(4):303–321.
- [26] Kajita, T. (2012). Atmospheric Neutrinos. *Advances in High Energy Physics* 2012:504715.
- [27] Mirizzi, A., et al. (2016). Supernova neutrinos: Production, oscillations and detection. *Rivista del Nuovo Cimento* 39(1-2):1–112.
- [28] Thompson, T. A. and Burrows, A. (2001). Neutrino processes in supernovae and the physics of protoneutron star winds. *Nuclear Physics A* 688(1):377–381.

- [29] Janka, H. (2016). Neutrino Emission from Supernovae, pp. 1–30. Springer International Publishing, Cham.
- [30] Hirata, K., et al. (1987). Observation of a neutrino burst from the supernova SN1987A. *Physical Review Letters* 58(14):1490–1493.
- [31] Bionta, R. M., et al. (1987). Observation of a neutrino burst in coincidence with supernova 1987A in the Large Magellanic Cloud. *Physical Review Letters* 58(14):1494–1496.
- [32] Alexeyev, E. N., Alexeyeva, L. N., Krivosheina, I. V., and Volchenko, V. I. (1988). Detection of the neutrino signal from SN 1987A in the LMC using the INR Baksan underground scintillation telescope. *Physics Letters B* 205(2):209–214.
- [33] Huber, P. and Schwetz, T. (2004). Precision spectroscopy with reactor antineutrinos. *Physical Review D* 70(5):53011.
- [34] Baldoncini, M., et al. (2015). Reference worldwide model for antineutrinos from reactors. *Physical Review D* 91(6):65002.
- [35] Sanshiro, E. (2006). Geoneutrino Spectrum and Luminosity. <http://www.awa.tohoku.ac.jp/~sanshiro/research/geoneutrino/spectrum/> (Accessed June 2018).
- [36] Gando, A., et al. (2011). Partial radiogenic heat model for Earth revealed by geoneutrino measurements. *Nature Geoscience* 4:647.
- [37] Bellini, G., et al. (2013). Measurement of geo-neutrinos from 1353 days of Borexino. *Physics Letters B* 722(4):295–300.
- [38] Mantovani, F., Carmignani, L., Fiorentini, G., and Lissia, M. (2004). Antineutrinos from Earth: A reference model and its uncertainties. *Physical Review D* 69(1):13001.

- [39] Fiorentini, G., Fogli, G. L., Lisi, E., Mantovani, F., and Rotunno, A. M. (2012). Mantle geoneutrinos in KamLAND and Borexino. *Physical Review D* 86(3):33004.
- [40] Agostini, M., et al. (2015). Spectroscopy of geoneutrinos from 2056 days of Borexino data. *Physical Review D* 92(3):31101.
- [41] Patrignani, C., et al. (2016). Review of Particle Physics. *Chinese Physics C* 40(10):100001.
- [42] Hellfeld, D., Bernstein, A., Dazeley, S., and Marianno, C. (2017). Reconstructing the direction of reactor antineutrinos via electron scattering in Gd-doped water Cherenkov detectors. *Nuclear Instruments and Methods in Physics Research Section A* 841:130–138.
- [43] Vogel, P. and Beacom, J. F. (1999). Angular distribution of neutron inverse beta decay. *Physical Review D* 60(5):53003.
- [44] Giunti, C. and Laveder, M. (2011). 3 + 1 and 3 + 2 sterile neutrino fits. *Phys. Rev. D* 84(7):73008.
- [45] Maki, Z., Nakagawa, M., and Sakata, S. (1962). Remarks on the Unified Model of Elementary Particles. *Progress of Theoretical Physics* 28(5):870–880.
- [46] Tanabashi, M., et al. (2018). The Review of Particle Physics. *Physical Review D* 98:030001.
- [47] Djurcic, Z. (2013). Review of reactor antineutrino experiments. *Journal of Physics: Conference Series* 408(1):12008.
- [48] Vogel, P., Wen, L. J., and Zhang, C. (2015). Neutrino oscillation studies with reactors. *Nature Communications* 6:6935.

- [49] Pac, M. Y. (2016). Experimental conditions for determination of the neutrino mass hierarchy with reactor antineutrinos. *Nuclear Physics B* 902:326–338.
- [50] Wolfenstein, L. (1978). Neutrino oscillations in matter. *Physical Review D* 17(9):2369–2374.
- [51] Li, Y., Wang, Y., and Xing, Z. (2016). Terrestrial matter effects on reactor antineutrino oscillations at JUNO or RENO-50: how small is small? *Chinese Physics C* 40(9):91001.
- [52] Majorana, E. (1937). Teoria simmetrica dellelettrone e del positrone. *Il Nuovo Cimento* 14:171–184.
- [53] Zuber, K. (2012). Neutrinoless double beta decay. *Pramana* 79(4):781–791.
- [54] Stoica, S. and Mirea, M. (2013). New calculations for phase space factors involved in double-beta decay. *Physical Review C* 88(3):37303.
- [55] Engel, J. (2015). Uncertainties in nuclear matrix elements for neutrinoless double-beta decay. *Journal of Physics G: Nuclear and Particle Physics* 42(3):34017.
- [56] Aharmim, B., et al. (2009). Measurement of the cosmic ray and neutrino-induced muon flux at the Sudbury neutrino observatory. *Physical Review D* 80(1):12001.
- [57] Bellini, G., et al. (2013). Cosmogenic Backgrounds in Borexino at 3800 m water-equivalent depth. *Journal of Cosmology and Astroparticle Physics* 2013(08):49.
- [58] Boger, J., et al. (2000). The Sudbury Neutrino Observatory. *Nuclear Instruments and Methods in Physics Research A* 449(449):172–207.

- [59] Andringa, S., et al. (2016). Current Status and Future Prospects of the SNO+ Experiment. *Advances in High Energy Physics* 2016:6194250.
- [60] Jones, P. G. (2011). Background rejection for the neutrinoless double beta decay experiment SNO+. PhD Thesis, University of Oxford.
- [61] Ford, R. J. (2015). A scintillator purification plant and fluid handling system for SNO+. *AIP Conference Proceedings* 1672(1):80003.
- [62] Biller, S. and Manecki, S. (2017). A New Technique to Load  $^{130}\text{Te}$  in Liquid Scintillator for Neutrinoless Double Beta Decay Experiments. *Journal of Physics: Conference Series* 888(1):12084.
- [63] Knapik, R., Bonventre, R., and Shokair, T. (2012). SNO+ Electronic Upgrades. *Nuclear Physics B Supplements* 229-232:523.
- [64] Braid, D. (2017). SNO+ Internal Document 3729. Technical report.
- [65] Bialek, A., et al. (2016). A rope-net support system for the liquid scintillator detector for the SNO+ experiment. *Nuclear Instruments and Methods in Physics Research Section A* 827:152–160.
- [66] Alves, R., et al. (2015). The calibration system for the photomultiplier array of the SNO+ experiment. *Journal of Instrumentation* 10(03):P03002.
- [67] Maneira, J., Falk, E., Leming, E., Peeters, S., and Collaboration., S. (2017). Calibration of the SNO+ experiment. *Journal of Physics: Conference Series* 888(1):12247.
- [68] Petriw, Z. (2012). An Underwater Six-Camera Array for Monitoring and Position Measurements in SNO+. MSc Thesis, University of Alberta.
- [69] Singh, K. (2017). SNO+ Internal Document 4161. Technical report.

- [70] Redshaw, M., Mount, B. J., Myers, E. G., and Avignone, F. T. (2009). Masses of  $^{130}\text{Te}$  and  $^{130}\text{Xe}$  and Double-Beta-Decay  $Q$  Value of  $^{130}\text{Te}$ . *Physical Review Letters* 102(21):212502.
- [71] Gabriel, O. SNO+. *Talk at XXVIII International Conference on Neutrino Physics and Astrophysics*. 4-9 June 2018, Heidelberg, Germany.
- [72] Bahcall, J. N., Gonzalez-Garcia, M. C., and Peña-Garay, C. (2003). Does the Sun Shine by p p or CNO Fusion Reactions? *Physical Review Letters* 90(13):131301.
- [73] Antonioli, P., et al. (2004). SNEWS: the SuperNova Early Warning System. *New Journal of Physics* 6(1):114.
- [74] Jelley, J. V. (1958). Cerenkov radiation, and its applications. Pergamon Press.
- [75] Hale, G. M. and Querry, M. R. (1973). Optical Constants of Water in the 200-nm to 200-um Wavelength Region. *Applied Optics* 12(3):555–563.
- [76] Kaptanoglu, T. and Marzec, E. (2018). SNO+ Internal Document 4768. Technical report.
- [77] Bonventre, R., et al. (2013). SNO+ Internal Document 1962. Technical report.
- [78] Hu, J. (2017). SNO+ Internal Document 4393. Technical report.
- [79] Spiegelberg-Planer, R. and Mandula, J. (2005). The power reactor information system (PRIS) and its extension to non-electrical applications, decommissioning and delayed projects information. International Atomic Energy Agency.
- [80] Asahi, S. (2016). SNO+ Internal Document 3763. Technical report.

- [81] Declais, Y., et al. (1994). Study of reactor antineutrino interaction with proton at Bugey nuclear power plant. *Physics Letters B* 338(2):383–389.
- [82] Ma, X. B., Zhong, W. L., Wang, L. Z., Chen, Y. X., and Cao, J. (2013). Improved calculation of the energy release in neutron-induced fission. *Physical Review C* 88(1):14605.
- [83] Baldoncini, M., et al. (2016). Geoneutrinos and reactor antineutrinos at SNO+. *Journal of Physics: Conference Series* 718(6):62003.
- [84] Huber, P. (2011). Determination of antineutrino spectra from nuclear reactors. *Physical Review C* 84(2):24617.
- [85] Mueller, T. A., et al. (2011). Improved predictions of reactor antineutrino spectra. *Physical Review C* 83(5):54615.
- [86] Hahn, A. A., et al. (1989). Antineutrino spectra from  $^{241}\text{Pu}$  and  $^{239}\text{Pu}$  thermal neutron fission products. *Physics Letters B* 218(3):365–368.
- [87] Vogel, P., Schenter, G. K., Mann, F. M., and Schenter, R. E. (1981). Reactor antineutrino spectra and their application to antineutrino-induced reactions. II. *Physical Review C* 24(4):1543–1553.
- [88] Lewis, B. J., Onder, E. N., and Prudil, A. A. (2017). Fundamentals of Nuclear Engineering. Wiley.
- [89] Asahi, S. (2015). SNO+ Internal Document 2944. Technical report.
- [90] Gando, A., et al. (2011). Constraints on  $\theta_{13}$  from a three-flavor oscillation analysis of reactor antineutrinos at KamLAND. *Physical Review D* 83(5):052002.
- [91] Lan, C. (2007). SNO+ and Geoneutrino Physics. MSc Thesis, Queen’s University.

- [92] Cokinos, D. and Melkonian, E. (1977). Measurement of the 2200 m/sec neutron-proton capture cross section. *Physical Review C* 15(5):1636–1643.
- [93] Zhang, Y., et al. (2016). First measurement of radioactive isotope production through cosmic-ray muon spallation in Super-Kamiokande IV. *Physical Review D* 93(1):12004.
- [94] Beacom, J. F. and Vagins, M. R. (2004). Antineutrino Spectroscopy with Large Water Čerenkov Detectors. *Physical Review Letters* 93(17):171101.
- [95] Aharmim, B., et al. (2005). Electron energy spectra, fluxes, and day-night asymmetries of  ${}^8\text{B}$  solar neutrinos from measurements with NaCl dissolved in the heavy-water detector at the Sudbury Neutrino Observatory. *Physical Review C* 72(5):55502.
- [96] Coulter, I. and Lebanowski, L. (2017). SNO+ Internal Document 4415. Technical report.
- [97] Kaptanoglu, T., Segui, L., Mastbaum, A., Barros, N., and Coulter, I. (2017). SNO+ Internal Document 3461. Technical report.
- [98] Naumov, D. V., Naumov, V. A., and Shkirmanov, D. S. (2017). Inverse-square law violation and reactor antineutrino anomaly. *Physics of Particles and Nuclei* 48(1):12–20.
- [99] Alimonti, G., et al. (2009). The Borexino detector at the Laboratori Nazionali del Gran Sasso. *Nuclear Instruments and Methods in Physics Research Section A* 600(3):568–593.
- [100] Abe, S., et al. (2008). Precision Measurement of Neutrino Oscillation Parameters with KamLAND. *Physical Review Letters* 100(22):221803.
- [101] An, F. P., et al. (2017). Evolution of the Reactor Antineutrino Flux and Spectrum at Daya Bay. *Physical Review Letters* 118(25):251801.

- [102] An, F. P., et al. (2012). A side-by-side comparison of Daya Bay antineutrino detectors. *Nuclear Instruments and Methods in Physics Research Section A* 685:78–97.
- [103] Choi, J. H., et al. (2016). Observation of Energy and Baseline Dependent Reactor Antineutrino Disappearance in the RENO Experiment. *Physical Review Letters* 116(21):211801.
- [104] Abe, Y., et al. (2012). Reactor  $\bar{\nu}_e$  disappearance in the Double Chooz experiment. *Physical Review D* 86(5):52008.
- [105] Abe, K., et al. (2016). Solar neutrino measurements in Super-Kamiokande-IV. *Physical Review D* 94(5):52010.
- [106] Agostinelli, S., et al. (2003). Geant4a simulation toolkit. *Nuclear Instruments and Methods in Physics Research Section A* 506(3):250–303.
- [107] Liu, Z., Chen, J., Zhu, P., Li, Y., and Zhang, G. (2007). The 4.438 MeV gamma to neutron ratio for the AmBe neutron source. *Applied Radiation and Isotopes* 65(12):1318–1321.
- [108] Kluge, H. and Weise, K. (1982). The Neutron Energy Spectrum of a  $^{241}\text{Am}$ -Be(Alpha,n) Source and Resulting Mean Fluence to Dose Equivalent Conversion Factors. *Radiation Protection Dosimetry* 2(2):85–93.
- [109] Basunia, M. S. (2011). Nuclear Data Sheets for  $A = 27$ . *Nuclear Data Sheets* 112(8):1875–1948.
- [110] Chadwick, M., et al. (2011). ENDF/B-VII.1 Nuclear Data for Science and Technology: Cross Sections, Covariances, Fission Product Yields and Decay Data. *Nuclear Data Sheets* 112(12):2887–2996.
- [111] Wang, M., et al. (2012). The AME2012 atomic mass evaluation (II). Tables, graphs and references. *Chinese Physics C* 36:1603.

- [112] Duke, M., Hallin, A., Krauss, C., Mekarski, P., and Sibley, L. (2016). A precise method to determine the activity of a weak neutron source using a germanium detector. *Applied Radiation and Isotopes* 116:51–56.
- [113] Failey, M. P., Anderson, D. L., Zoller, W. H., Gordon, G. E., and Lindstrom, R. M. (1979). Neutron-capture prompt  $\gamma$ -ray activation analysis for multielement determination in complex samples. *Analytical Chemistry* 51(13):2209–2221.
- [114] Nakamura, T. (2008). Cosmic-ray Neutron Spectrometry and Dosimetry. *Journal of Nuclear Science and Technology* 45(sup5):1–7.
- [115] Browne, E. and Tuli, J. K. (2013). Nuclear Data Sheets for  $A = 60$ . *Nuclear Data Sheets* 114(12):1849–2022.
- [116] Manecki, S. (2018). SNO+ Internal Document 5097. Technical report.
- [117] Ziegler, J. F. (1998). Terrestrial cosmic ray intensities. *IBM Journal of Research and Development* 42(1):117–140.
- [118] Lozza, V. and Petzoldt, J. (2015). Cosmogenic activation of a natural tellurium target. *Astroparticle Physics* 61:62–71.
- [119] Brown, D. A., et al. (2018). ENDF/B-VIII.0: The 8th Major Release of the Nuclear Reaction Data Library with CIELO-project Cross Sections, New Standards and Thermal Scattering Data. *Nuclear Data Sheets* 148:1–142.
- [120] Hashizume, A. (2011). Nuclear Data Sheets for  $A = 127$ . *Nuclear Data Sheets* 112(7):1647–1831.
- [121] Timar, J., Elekes, Z., and Singh, B. (2014). Nuclear Data Sheets for  $A = 129$ . *Nuclear Data Sheets* 121:143–394.

- [122] Khazov, Y., Mitropolsky, I., and Rodionov, A. (2006). Nuclear Data Sheets for  $A = 131$ . *Nuclear Data Sheets* 107(11):2715–2930.
- [123] Brun, R. and Rademakers, F. (1997). ROOT An object oriented data analysis framework. *Nuclear Instruments and Methods in Physics Research Section A* 389(1):81–86.
- [124] Barros, N. (2017). SNO+ Internal Document 4276. Technical report.
- [125] Nae, S. (2017). SNO+ Internal Document 4195. Technical report.
- [126] Lozza, V. (2018). SNO+ Internal Document 1981. Technical report.
- [127] Wright, A. (2018). SNO+ Internal Document 4859. Technical report.
- [128] Svoboda, R., Wilson, J., and Wright, A. (2018). SNO+ Internal Document 3412. Technical report.
- [129] Tamm, I. E. and Frank, I. M. (1939). *Doklady Akademii Nauk SSSR* 214:107.
- [130] Biller, S. D., Jelley, N. A., Thorman, M. D., Fox, N. P., and Ward, T. H. (1999). Measurements of photomultiplier single photon counting efficiency for the Sudbury Neutrino Observatory. *Nuclear Instruments and Methods in Physics Research Section A* 432(2):364–373.
- [131] Radcliffe, T. J. . (1995). SNO Internal Report: SNO-STR-95-007. Technical report.
- [132] Dai, X., et al. (2008). Wavelength shifters for water Cherenkov detectors. *Nuclear Instruments and Methods in Physics Research Section A* 589(2):290–295.
- [133] Singh, K. (2016). SNO+ Internal Document 3527. Technical report.

- [134] Xiao-Bo, L., et al. (2011). Timing properties and pulse shape discrimination of LAB-based liquid scintillator. *Chinese Physics C* 35(11):1026.
- [135] Singh, K. (2016). SNO+ Internal Document 3658. Technical report.
- [136] Krar, B., Liu, Y., and Skensved, P. (2018). SNO+ Internal Document 4725. Technical report.
- [137] Loach, J. (2008). Measurement of the Flux of  $^8\text{B}$  Solar Neutrinos at the Sudbury Neutrino Observatory. PhD Thesis, University of Oxford.
- [138] Andringa, S. and Liu, Y. (2018). SNO+ Internal Document 4771. Technical report.
- [139] Bowden, N. S., Sweany, M., and Dazeley, S. (2012). A note on neutron capture correlation signals, backgrounds, and efficiencies. *Nuclear Instruments and Methods in Physics Research Section A* 693:209–214.
- [140] Li, A. (2018). SNO+ Internal Document 4821. Technical report.
- [141] Mowlavi, A. A. and Koohi-Fayegh, R. (2004). Determination of 4.438 MeV gamma-ray to neutron emission ratio from a  $^{241}\text{Am}$ - $^9\text{Be}$  neutron source. *Applied Radiation and Isotopes* 60(6):959–962.
- [142] Kamboj, B. K. and Shahani, M. G. (1986). Precise measurement of the gamma to neutron ratio of an Am- $\alpha$ -Be neutron source using an improved manganese bath technique. *Nuclear Instruments and Methods in Physics Research Section A* 244(3):513–515.
- [143] Hu, J. (2018). SNO+ Internal Document 4936. Technical report.
- [144] Lebanowski, L. (2017). SNO+ Internal Document 4398. Technical report.
- [145] Dragowsky, M. R., et al. (2002). The  $^{16}\text{N}$  calibration source for the Sudbury Neutrino Observatory. *Nuclear Instruments and Methods in Physics Research Section A* 481(1):284–296.

- [146] Tilley, D. R., Weller, H. R., and Cheves, C. M. (1993). Energy levels of light nuclei  $A = 16$ . *Nuclear Physics A* 564(1):1–183.
- [147] Hamer, A. (1999). Energy Calibration of SNO for Measurement of the Charged-Current Neutrino Reaction. PhD Thesis, Queen's University.
- [148] Boulay, M. (2001). Direct Evidence for Weak Flavour Mixing with the Sudbury Neutrino Observatory. PhD Thesis, Queen's University.
- [149] LaTorre, A. (2017). SNO+ Internal Document 4728. Technical report.
- [150] Caden, E. (2018). SNO+ Internal Document 5080. Technical report.
- [151] Ahmad, Q. R. (2002). Muon Correlated Background at The Sudbury Neutrino Observatory. PhD Thesis, Brown University.
- [152] Lozza, V. (2018). SNO+ Internal Document 4996. Technical report.
- [153] Feldman, G. J. and Cousins, R. D. (1998). Unified approach to the classical statistical analysis of small signals. *Physical Review D* 57(7):3873–3889.
- [154] Independent Electricity System Operator, Power Data Directory <http://www.ieso.ca/en/power-data/data-directory> (Accessed June 2018).
- [155] Usman, S. M., Jocher, G. R., Dye, S. T., McDonough, W. F., and Learned, J. G. (2015). AGM2015: Antineutrino Global Map 2015. *Scientific Reports* 5:13945.

# Appendix A

## Inelastic Scattering Model

Over the course of the measurements with the HPGe detector in Chapter 4, it was discovered that the inelastic scattering of neutrons was not being modeled properly in some circumstances. Within Geant4, the inelastic scattering process produces  $\gamma$  rays as the secondary particle in the interaction. These  $\gamma$  rays are designed to correspond to those from the decay of excited nuclear states (of the nucleus off of which the neutron scattered).

During the course of laboratory measurements of this reaction on aluminum, nickel, and copper targets, a problem in the simulation was discovered. The simulation produced much less (if any)  $\gamma$  rays at the specific energies corresponding to decay of these excited nuclear states. In addition, it was found to be producing  $\gamma$  rays with a continuous spectrum of energies from this reaction. This is a known occurrence in Geant4, where to conserve the total energy of the interaction, Geant4 will emit  $\gamma$  rays with the “lost” energy. In the case of laboratory measurements, where the target and detector are different volumes, this results in unphysical peaks in the measured  $\gamma$  ray energy spectra.

To model neutron interactions at the MeV scale, the “Neutron HP” packages should be used for each interaction. These packages are based on measured neutron cross sections (rather than calculated cross sections). This results in more accurate simulations, especially as many nuclei have large resonances in

this energy range. With these packages, the inelastic scattering process was found to occur within the simulated target materials with the correct total cross section  $\sigma_{total}$  (when comparing to the data published in the Evaluated Nuclear Data File (ENDF) by the National Nuclear Data Center of Brookhaven National Laboratory). This total cross section  $\sigma_{total}$  is the sum of the cross sections for excitation to each of the possible nuclear energy levels of a given nucleus:

$$\sigma_{total} = \sigma_{L1} + \sigma_{L2} + \sigma_{L3} + \dots \quad (\text{A.1})$$

where each cross section  $\sigma_{Ln}$  corresponds to excitation to the  $n^{\text{th}}$  energy level.

The simulation was performed in two steps. First, the simulation was performed with neutrons as the primary particles. If a neutron inelastically scattered, the  $(x, y, z)$  position of this interaction within the simulation would be stored. A second separate simulation would then be performed. For each  $(x, y, z)$  position this simulation would generate excited nuclei by sampling in the following way.

Each energy level was first constructed as a range of values:

$$\begin{aligned} L1 &= \left[ 0, \frac{\sigma_{L1}}{\sigma_{total}} \right] \\ L2 &= \left[ \frac{\sigma_{L1}}{\sigma_{total}}, \frac{\sigma_{L1} + \sigma_{L2}}{\sigma_{total}} \right] \\ L3 &= \left[ \frac{\sigma_{L1} + \sigma_{L2}}{\sigma_{total}}, \frac{\sigma_{L1} + \sigma_{L2} + \sigma_{L3}}{\sigma_{total}} \right] \\ &\dots \end{aligned} \quad (\text{A.2})$$

where these ranges start at 0 (for  $L1$ ) and finish at 1 (for  $Ln$ ). A random number would then be sampled from  $[0, 1]$ . This number would correspond to one of the previous ranges  $Ln$ . The simulation was set to produce an excited nucleus with energy equal to the excited nuclear state  $Ln$  at the position  $(x, y, z)$ . The standard “Decay” packages within Geant4 would then simulate the decay of this excited nucleus. This resulted in simulations that were consistent with

measurements.

It should be noted that while this was found to be a problem for the lighter metals that were measured (aluminum, nickel, and copper), it was not a problem for tellurium (Section 4.5.4). In that case, this approach produced similar results to the default simulation. The reason for this variation across target materials is not known.

# Appendix B

## Data Cleaning Cuts

The following list details each of the data cleaning cuts used. These cuts were applied identically to all data sets and Monte Carlo simulations. A brief description is included for each entry.

- **zerozerocut** — Removes events with GTID’s that end in 00, needed due to a rollover issue.
- **ringoffire** — Removes events where the majority of the hits are in a ‘ring’ in one crate.
- **crateisotropy** — Removes events where noise from one channel causes adjacent channels to trigger, resulting in an anisotropic distribution of hits in electronics space.
- **flashergeocut** — Removes “flashers”. These are events where excess charge in one card produced light in the detector, causing an excess of hits opposite the card.
- **muontag** — Identifies events as muons by looking for a large number of total hits and outward-looking PMT (OWL) hits.
- **owlcut** — Removes events that have a high number of OWL hits.

- **neckcut** — Removes events that have a high number of neck PMT hits.
- **junkcut** — Removes events where a channel is registered as having more than one hit.
- **qcluster** — Remove instrumental events where high charge in one channel results in the hits of adjacent channels.
- **qvt** — Removes “flasher” events that have low charge in the flashing tube. This is done by looking for events earlier in time with a high-charge channel.
- **qvnhit** — Removes noise events by comparing the charge for each hit. Noise events typically have lower charge than expected.
- **itctimespreadcut** — Removes instrumental events by comparing the hit times of each PMT in an event. Instrumental events will have more broadly distributed hit times than Cherenkov light-produced events.
- **ftscut** — Removes “flashers” where the data from the flashing card is not saved. This is done by looking at the median time difference of closely-spaced hits in an event. Cherenkov light-produced events have a short median time.
- **tpmuonfollowercut-short** — Removes the possibility of muon-follower events by removing events within 20 s of a previously tagged muon.
- **caencut** — Removes instrumental events by looking at the voltage traces recorded by the Costruzioni Apparecchiature Elettroniche Nucleari (CAEN) digitizer.
- **pollingcut** — Removes events that occur while routine data acquisition system calibrations are being performed, when there is increased hardware noise.

# Appendix C

## SNO+ Water Data Runs

The following table consists of the “golden” runs from the period of September 1, 2017 – March 31, 2018. It should be noted that this golden run list was not finalized by the SNO+ run selection committee at the time of this analysis and could differ in future analyses.

Run Numbers used in the Antineutrino Search									
104617	104886	105513	105761	106158	106566	106894	107363	108195	<b>109026</b>
104620	104887	105514	105762	106159	106567	106895	107365	108199	<b>109027</b>
104621	104888	105515	105763	106160	106568	106896	107366	108200	<b>109028</b>
104622	104889	105516	105764	106161	106571	106897	107367	108201	<b>109029</b>
104623	104890	105517	105765	106162	106572	106898	107368	108202	<b>109030</b>
104624	104891	105518	105766	106163	106573	106899	107370	108203	<b>109031</b>
104625	104892	105519	105767	106164	106574	106900	107371	108210	<b>109032</b>
104626	104893	105521	105768	106165	106575	106901	107372	108211	<b>109033</b>
104627	104894	105522	105769	106166	106576	106902	107373	108212	<b>109034</b>
104628	104895	105523	105770	106167	106577	106903	107374	108213	<b>109035</b>
104629	104896	105524	105772	106168	106578	106904	107375	108214	<b>109036</b>
104630	104897	105525	105773	106169	106579	106905	107376	108215	<b>109037</b>
104631	104911	105526	105774	106172	106580	106906	107377	108216	<b>109038</b>
104633	104914	105527	105775	106173	106581	107129	107380	108217	<b>109040</b>
104636	104915	105528	105776	106175	106582	107130	107381	108218	<b>109041</b>
104637	104916	105529	105777	106176	106583	107131	107383	108219	<b>109042</b>
104639	104917	105530	105778	106177	106584	107132	107387	108220	<b>109043</b>
104641	104918	105539	105779	106178	106585	107141	107388	108221	<b>109045</b>
104643	104919	105540	105780	106179	106586	107142	107389	108222	<b>109046</b>

**1047XX** - runs used for the toy Monte Carlo background simulation

**109XXX** - runs used as comparison to AmBe source data

Run Numbers used in the Antineutrino Search

104644	104920	105541	105781	106186	106587	107143	107390	108225	<b>109047</b>
104645	104922	105542	105782	106187	106589	107144	107391	108226	<b>109048</b>
104647	104923	105543	105783	106188	106590	107145	107396	108227	<b>109049</b>
104648	104924	105544	105784	106189	106591	107146	107397	108228	<b>109053</b>
104649	104925	105545	105785	106190	106592	107147	107398	108229	<b>109054</b>
104650	104926	105546	105813	106191	106593	107148	107399	108231	<b>109056</b>
104651	104929	105547	105814	106192	106594	107149	107400	108232	<b>109057</b>
104652	104930	105548	105815	106193	106595	107150	107401	108233	<b>109059</b>
104653	104931	105549	105816	106194	106596	107151	107402	108234	<b>109060</b>
104654	104932	105550	105817	106195	106597	107152	107403	108235	<b>109061</b>
104655	104933	105551	105818	106196	106598	107153	107404	108236	<b>109062</b>
104657	104934	105552	105819	106206	106599	107154	107405	108237	<b>109066</b>
104658	104995	105553	105820	106213	106600	107155	107406	108238	<b>109067</b>
104659	104998	105554	105841	106214	106601	107156	107407	108239	<b>109068</b>
104660	104999	105555	105842	106215	106602	107157	107408	108240	<b>109069</b>
104661	105000	105556	105843	106216	106603	107158	107409	108248	<b>109071</b>
104663	105001	105557	105845	106217	106604	107159	107410	108249	<b>109072</b>
104664	105002	105558	105853	106218	106605	107160	107411	108250	<b>109313</b>
104665	105003	105559	105855	106219	106606	107161	107412	108251	<b>109314</b>
104667	105004	105560	105867	106220	106607	107162	107413	108252	<b>109317</b>
104668	105005	105561	105868	106221	106608	107163	107415	108253	<b>109318</b>
104669	105006	105562	105869	106222	106609	107164	107416	108256	<b>109319</b>
104670	105007	105563	105873	106223	106610	107165	107417	108257	<b>109320</b>
104671	105008	105564	105874	106224	106611	107166	107418	108258	<b>109321</b>
104672	105009	105565	105875	106225	106612	107167	107419	108259	<b>109322</b>
104673	105011	105566	105876	106226	106613	107168	107420	108260	<b>109323</b>
104674	105012	105567	105877	106227	106614	107169	107421	108261	<b>109325</b>
104675	105013	105568	105878	106228	106615	107170	107422	108262	<b>109326</b>
104676	105014	105569	105879	106229	106617	107171	107423	108263	<b>109327</b>
104688	105015	105570	105880	106230	106618	107172	107424	108264	<b>109329</b>
104693	105048	105571	105881	106239	106619	107173	107425	108265	<b>109330</b>
104694	105049	105572	105917	106240	106620	107174	107426	108266	<b>109331</b>
104697	105050	105573	105918	106241	106621	107175	107428	108267	<b>109349</b>
104698	105051	105574	105919	106248	106622	107176	107429	108268	<b>109352</b>
104699	105052	105575	105920	106249	106623	107177	107430	108269	<b>109353</b>
<b>104700</b>	105055	105577	105921	106250	106624	107178	107431	108270	<b>109354</b>
<b>104703</b>	105056	105578	105922	106251	106625	107179	107432	108271	<b>109355</b>
<b>104704</b>	105057	105579	105923	106252	106626	107180	107433	108272	<b>109357</b>
<b>104706</b>	105058	105580	105924	106253	106627	107181	107434	108275	<b>109358</b>
<b>104707</b>	105059	105581	105925	106254	106628	107182	107435	108277	<b>109359</b>

**1047XX** - runs used for the toy Monte Carlo background simulation**109XXX** - runs used as comparison to AmBe source data

## Run Numbers used in the Antineutrino Search

<b>104708</b>	105064	105582	105926	106255	106629	107183	107436	108278	<b>109360</b>
<b>104709</b>	105065	105583	105927	106256	106630	107184	107442	108279	<b>109362</b>
<b>104710</b>	105066	105584	105928	106257	106631	107185	107443	108280	<b>109363</b>
<b>104713</b>	105067	105585	105929	106259	106632	107186	107444	108281	<b>109364</b>
<b>104714</b>	105068	105586	105930	106271	106643	107187	107445	108282	<b>109365</b>
<b>104715</b>	105069	105587	105931	106272	106644	107188	107446	108283	109984
<b>104716</b>	105071	105588	105932	106273	106645	107189	107447	108284	109986
<b>104717</b>	105072	105589	105933	106274	106646	107190	107448	108285	109987
<b>104719</b>	105075	105590	105939	106279	106652	107191	107449	108286	109988
<b>104720</b>	105077	105591	105940	106280	106653	107192	107450	108287	109989
<b>104721</b>	105082	105592	105941	106281	106654	107193	107451	108288	109990
<b>104722</b>	105084	105593	105942	106282	106655	107194	107452	108289	109991
<b>104723</b>	105085	105594	105948	106283	106656	107195	107453	108309	109992
<b>104724</b>	105087	105595	105949	106284	106657	107196	107454	108310	109993
<b>104725</b>	105088	105596	105950	106285	106659	107197	107455	108311	109994
<b>104726</b>	105089	105598	105951	106286	106660	107198	107458	108312	109995
<b>104734</b>	105090	105599	105952	106287	106661	107199	107459	108313	110134
<b>104735</b>	105091	105600	105953	106288	106662	107200	107460	108314	110917
<b>104736</b>	105092	105601	105956	106289	106663	107201	107461	108315	110918
<b>104737</b>	105112	105604	105957	106290	106664	107202	107462	108316	110919
<b>104738</b>	105113	105605	105958	106302	106665	107203	107509	108317	110920
<b>104739</b>	105114	105606	105960	106303	106666	107204	107510	108318	110921
<b>104740</b>	105116	105607	105961	106304	106669	107205	107513	108319	110922
<b>104741</b>	105118	105608	105962	106306	106675	107206	107516	108320	110923
<b>104742</b>	105120	105609	105963	106307	106676	107207	107517	108321	110924
<b>104743</b>	105121	105610	105964	106308	106677	107208	107518	108322	110925
<b>104745</b>	105122	105611	105965	106309	106678	107209	107519	108323	110926
<b>104746</b>	105125	105612	105966	106310	106679	107210	107520	108324	110927
<b>104747</b>	105126	105613	105967	106311	106680	107211	107521	108325	111065
<b>104748</b>	105127	105614	105968	106312	106681	107212	107522	108326	111066
<b>104749</b>	105128	105615	105969	106446	106683	107213	107523	108327	111067
<b>104750</b>	105129	105616	105970	106447	106684	107214	107524	108328	111068
<b>104751</b>	105131	105618	105971	106449	106685	107215	107525	108329	111071
<b>104752</b>	105132	105619	105972	106450	106686	107216	107526	108330	111073
<b>104753</b>	105134	105645	105973	106451	106687	107217	107542	108331	111074
<b>104754</b>	105136	105646	105974	106452	106688	107218	107543	108332	111075
<b>104755</b>	105145	105647	105975	106459	106689	107219	107545	108333	111076
<b>104757</b>	105146	105648	105976	106460	106690	107220	107557	108334	111077
<b>104758</b>	105150	105649	105977	106461	106691	107221	107566	108335	111078
<b>104759</b>	105151	105650	105978	106462	106692	107222	107567	108336	111081

**1047XX** - runs used for the toy Monte Carlo background simulation

**109XXX** - runs used as comparison to AmBe source data

## Run Numbers used in the Antineutrino Search

<b>104760</b>	105152	105651	105979	106463	106693	107223	107572	108337	111082
<b>104761</b>	105157	105652	105980	106465	106694	107224	107576	108338	111083
<b>104762</b>	105158	105653	105981	106466	106707	107225	107582	108339	111084
<b>104764</b>	105159	105654	105982	106467	106708	107226	107583	108340	111085
<b>104765</b>	105161	105655	105983	106468	106709	107227	107584	108341	111139
<b>104766</b>	105162	105656	105984	106469	106710	107228	107585	108342	111140
<b>104767</b>	105163	105657	105985	106470	106711	107229	107593	108343	111141
<b>104768</b>	105166	105658	105986	106471	106712	107230	107594	108347	111142
<b>104771</b>	105167	105659	105987	106472	106713	107233	107595	108348	111143
<b>104772</b>	105168	105660	105988	106473	106714	107235	107596	108349	111144
<b>104773</b>	105169	105661	105989	106474	106715	107236	107597	108350	111145
<b>104774</b>	105189	105680	105990	106475	106716	107237	107598	108351	111146
<b>104776</b>	105190	105681	105991	106476	106717	107241	107599	108352	111147
<b>104777</b>	105191	105682	105992	106477	106718	107242	107600	108353	111148
<b>104778</b>	105192	105683	105993	106478	106719	107244	107601	108354	111149
104804	105193	105684	105994	106479	106720	107245	107602	108355	111161
104806	105194	105685	105995	106484	106721	107246	107603	108356	111162
104815	105195	105688	105996	106485	106722	107247	107608	108357	111172
104816	105198	105689	105997	106486	106736	107248	107609	108358	111173
104817	105199	105690	105998	106487	106737	107249	107612	108359	111174
104818	105200	105691	105999	106488	106738	107253	107615	108360	111175
104820	105201	105692	106000	106489	106739	107254	107616	108361	111176
104821	105202	105693	106001	106490	106740	107255	107617	108362	111177
104823	105203	105694	106002	106491	106741	107256	107619	108363	111178
104825	105204	105702	106003	106492	106810	107257	107620	108364	111192
104826	105205	105703	106004	106493	106811	107258	107621	108365	111193
104827	105235	105704	106070	106494	106812	107259	107622	108366	111194
104828	105248	105708	106071	106495	106813	107263	107623	108367	111201
104829	105251	105709	106072	106496	106814	107264	107628	108368	111202
104830	105252	105710	106073	106497	106815	107267	107629	108369	111203
104831	105275	105711	106074	106498	106816	107270	107630	108370	111204
104832	105276	105712	106075	106499	106817	107272	107631	108371	111205
104833	105278	105713	106076	106515	106818	107273	107632	108375	111206
104834	105407	105714	106077	106516	106820	107275	107633	108376	111207
104835	105408	105715	106078	106517	106821	107278	107634	108377	111292
104836	105413	105716	106079	106520	106822	107279	107635	108378	111293
104837	105414	105717	106080	106521	106823	107281	107637	108379	111294
104838	105415	105718	106081	106522	106824	107282	107638	108380	111296
104839	105416	105719	106082	106523	106825	107285	107639	108381	111297
104840	105417	105720	106083	106524	106830	107286	107640	108382	111298

**1047XX** - runs used for the toy Monte Carlo background simulation

**109XXX** - runs used as comparison to AmBe source data

Run Numbers used in the Antineutrino Search									
104841	105418	105721	106084	106525	106831	107287	108143	108383	111299
104842	105427	105722	106096	106526	106832	107289	108144	108384	111300
104843	105430	105723	106097	106527	106837	107290	108145	108385	111301
104844	105431	105724	106098	106528	106838	107291	108146	108386	111302
104845	105433	105726	106099	106529	106839	107292	108147	108387	111303
104846	105434	105727	106104	106530	106843	107293	108148	108388	111304
104847	105435	105728	106105	106531	106844	107294	108149	108389	111305
104848	105436	105729	106109	106532	106856	107295	108150	108390	111306
104849	105437	105730	106110	106533	106857	107297	108151	108391	111307
104850	105438	105731	106111	106534	106858	107303	108152	108392	111308
104851	105439	105732	106112	106535	106859	107306	108153	108393	111310
104852	105440	105733	106129	106536	106860	107307	108156	108394	111311
104853	105441	105734	106130	106537	106861	107311	108157	108395	111312
104854	105442	105735	106131	106539	106862	107312	108158	108396	111313
104855	105443	105736	106132	106540	106863	107313	108159	108397	111314
104856	105444	105737	106133	106541	106864	107314	108160	108400	111315
104857	105445	105738	106134	106542	106865	107315	108161	108401	111316
104858	105446	105739	106135	106543	106866	107316	108162	108402	111317
104859	105447	105740	106136	106544	106867	107317	108163	108403	111318
104860	105448	105741	106137	106545	106868	107320	108164	108404	111319
104861	105449	105742	106138	106546	106869	107321	108165	108405	111320
104862	105452	105743	106139	106547	106870	107322	108169	108406	111321
104863	105453	105744	106140	106548	106871	107325	108170	108407	111322
104864	105455	105745	106141	106549	106872	107326	108171	108408	111323
104866	105456	105746	106142	106550	106873	107327	108172	108409	111325
104867	105457	105747	106143	106551	106874	107328	108173	108410	111326
104868	105458	105748	106144	106552	106875	107329	108174	108411	111327
104869	105488	105749	106145	106553	106876	107350	108176	108412	111328
104870	105489	105750	106146	106554	106877	107351	108177	108413	111329
104871	105490	105751	106147	106555	106878	107352	108178	108414	111330
104872	105491	105752	106148	106556	106879	107353	108180	108415	111331
104873	105492	105753	106149	106558	106880	107355	108181	108416	111332
104876	105493	105754	106150	106559	106881	107356	108182	<b>109019</b>	111333
104877	105494	105755	106152	106560	106882	107357	108187	<b>109020</b>	111334
104880	105495	105756	106153	106561	106883	107358	108190	<b>109021</b>	111335
104881	105496	105757	106154	106562	106885	107359	108191	<b>109022</b>	111336
104882	105497	105758	106155	106563	106886	107360	108192	<b>109023</b>	111337
104883	105498	105759	106156	106564	106891	107361	108193	<b>109024</b>	111338
104884	105499	105760	106157	106565	106893	107362	108194	<b>109025</b>	111339
104885	105511								

**1047XX** - runs used for the toy Monte Carlo background simulation

**109XXX** - runs used as comparison to AmBe source data

## Appendix D

# Signal to Background Optimization

The method chosen to optimize the selection criteria relied on maximizing the measured signal  $N_{\text{sig meas}}$  to background  $N_{\text{bkgd meas}}$  through:

$$\frac{N_{\text{sig meas}}}{\sqrt{N_{\text{bkgd meas}}}} \quad (\text{D.1})$$

This value corresponds to the significance of the measured signal. More correctly, this value would be:

$$\frac{N_{\text{sig meas}}}{\sqrt{N_{\text{sig meas}} + N_{\text{bkgd meas}}}} \quad (\text{D.2})$$

as the quantity measured in an experiment is the sum of the signal and background. However, in the case of this analysis the expected signal (Section 7.4) is much less than the expected background (Section 8.3). Therefore making  $\sqrt{N_{\text{sig meas}} + N_{\text{bkgd meas}}} \approx \sqrt{N_{\text{bkgd meas}}}$ .

From the previously defined signal acceptance  $SA$  and background accep-

tance  $BA$ , this quantity can be rewritten as:

$$\frac{N_{\text{sig meas}}}{\sqrt{N_{\text{bkgd meas}}}} = \frac{N_{\text{sig total}}}{\sqrt{N_{\text{bkgd total}}}} \frac{SA}{\sqrt{BA}} \quad (\text{D.3})$$

where  $N_{\text{sig total}}$  and  $N_{\text{bkgd total}}$  are the total expected signal and background in a given data set. As this total does not change as a function of any given cut parameter, the term  $\frac{N_{\text{sig total}}}{\sqrt{N_{\text{bkgd total}}}}$  is a constant. Changing the expected values for  $N_{\text{sig total}}$  and/or  $N_{\text{bkgd total}}$  would change the shape of the  $\frac{SA}{\sqrt{BA}}$  curve and the maximum significance, but it would not change the parameter value at which the curve is maximal. This effect will be illustrated.

The following example is based on the optimization of the time difference cut parameter  $\Delta t$ . The values of  $N_{\text{sig total}}$  and  $N_{\text{bkgd total}}$  were varied and  $\frac{SA}{\sqrt{BA}}$  was plotted as a function of the cut parameter, Figure D.1.

The effect of extending the range of considered coincidences were also explored. The  $SA$  and  $BA$  parameters were previously constructed as the fraction of events that pass of the total in a  $1000 \mu\text{s}$  time window. Instead they were constructed as the same such fraction that pass within a  $3000 \mu\text{s}$  window. Figure D.2.

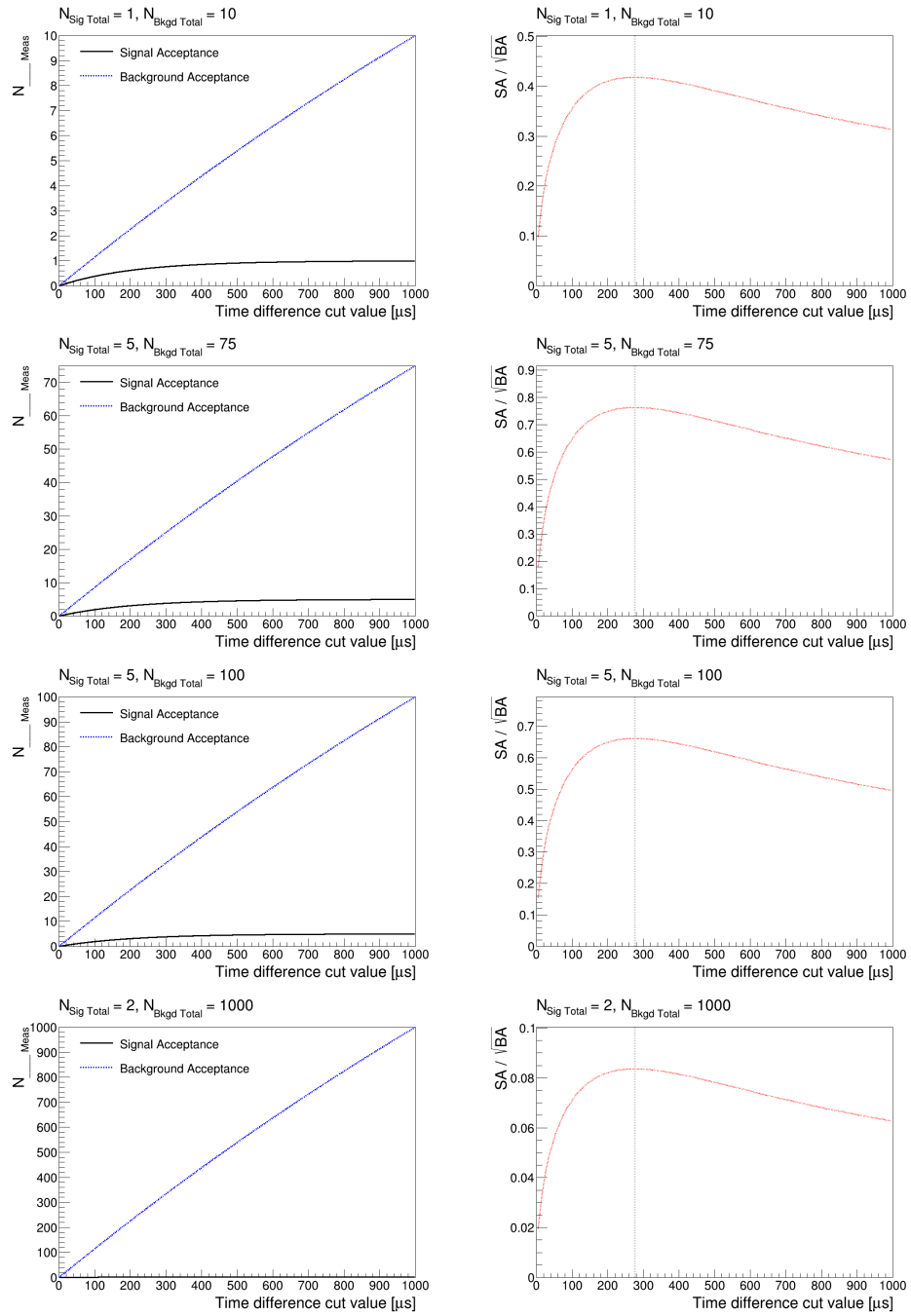


Figure D.1: Number of measured signal and background events as a function of the time difference cut parameter. The maximum is found at a cut value of  $275 \mu\text{s}$ .

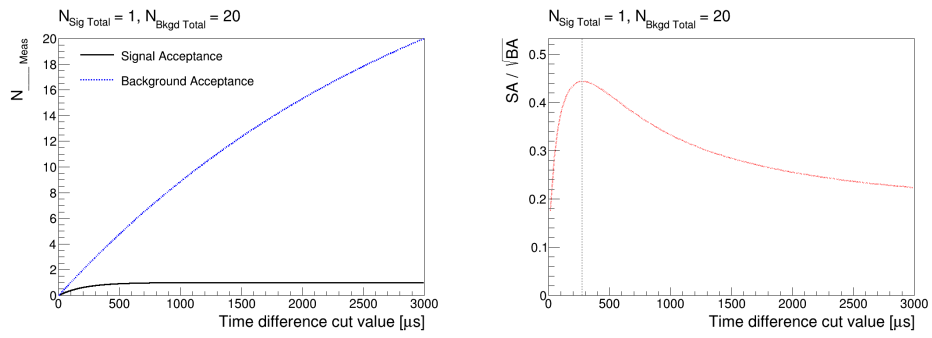


Figure D.2: Number of measured signal and background events as a function of the time difference cut parameter. The maximum is found at a cut value of 275  $\mu\text{s}$ .